UNIVERSIDAD NACIONAL AUTÓNOMA DE MÉXICO
POSGRADO EN ASTROFÍSICA

CHARACTERIZATION OF TWO COMPACT IACT TELESCOPES *HAWC's Eye* IN SYNCHRONY WITH THE HAWC GAMMA-RAY OBSERVATORY

T E S I S

QUE PARA OPTAR POR EL GRADO DE:
MAESTRO EN CIENCIAS (ASTROFÍSICA)

PRESENTA:
JOSÉ ERANDI SERNA FRANCO

TUTOR
DR. JOSÉ RUBÉN ALFARO MOLINA
INSTITUTO DE FÍSICA - UNAM

COMITÉ TUTOR
DRA. MARIANA CANO DÍAZ
INSTITUTO DE ASTRONOMÍA - UNAM
DRA. MARIANA VARGAS MAGAÑA
INSTITUTO DE FÍSICA - UNAM

CIUDAD UNIVERSITARIA, CDMX - DICIEMBRE 2021

Para Angelina, Alma y José.
Mi más grande y mejor ejemplo.

Supervisor
Dr. José Rubén
Alfaro Molina
Instituto de Física
UNAM

Referee 1
Dr. Juan Carlos
Arteaga Velázquez
Instituto de Física y Matemáticas
UMSNH

Referee 2
Dr. Ernesto José María de la Salete
Belmont Moreno
Instituto de Física
UNAM

Referee 3
Dr. Alejandro
Farah Simón
Instituto de Astronomía
UNAM

Referee 4
Dr. Eduardo
Moreno Barbosa
Facultad de Ciencias Físico Matemáticas
BUAP

Referee 5
Dr. Ibrahim Daniel
Torres Aguilar
Coordinación de Astrofísica
INAOE

INDEX

List of Figures

List of Tables

GLOSSARY

AC/DC	-	Altern Current/Direct Current
AERIE	-	Analysis and Event Reconstruction Integrated Environment
CDT	-	Central Daylight Time
COG	-	Center Of Gravity
CST	-	Central Standard Time
DAC	-	Digital-to-Analog Counts
DAQ	-	Data Acquisition system
DIM	-	Distributed Information Management system
DRS4	-	Domino Ring Sampling chip
EAS	-	Extensive Air Shower
FACT	-	First g-Adp Cherenkov Telescope
FAD	-	Fast Analog-to-Digital converter
FITS	-	Flexible Image Transport System
FoV	-	Field of View
FPA	-	FACT Pre-Amplifier
FTU	-	FACT Trigger Unit
G-APD	-	Geiger-mode Avalanche Photodiode
HAWC Observatory	-	High Altitude Water Cherenkov observatory
HE01	-	HAWC's Eye 01
HE02	-	HAWC's Eye 02
IACT	-	Imaging-Air Cherenkov Telescope
MAGIC	-	Major Atmospheric Gamma-ray Imaginc Cherenkov telescope
MC	-	Monte Carlo
MILAGRO	-	Multiple Institution Los Alamos Gamma Ray Observatory
miniFTM	-	FACT Trigger Master
PCB	-	Printed Control Board card
PE	-	Photo-Electron
PINCness	-	Parameter for Identifying Nuclear Cosmic rays
PMT	-	Photomultiplier Tube
PMMA	-	Polymethyl Methacrylate
PSU	-	Power Supply Unit
RF	-	Random Forest
SiPM	-	Silicon Photomultiplier
TDC	-	Time-to-Digital Converter
TUI	-	Text User Interface
UTC	-	Coordinated Universal Time
VAMOS	-	Verification and Assessment Measuring of Observatory Subsystem
XCDF	-	eXplicit bitwise-Compacted Data Format

1

PRELIMINARIES

Since the discovery of cosmic rays more than one hundred years ago, they have been measured and studied to understand the processes that produce them and consequently, to know more about the universe where we are living in. Even though the cosmic rays have been the center of several studies, some characteristics, as their origin and propagation methods are still unknown.

Cosmic rays consist of electrons and totally ionized nuclei of atoms, and they arrive in equal amounts from all directions. Since cosmic rays are electrically charged, they are deflected by the magnetic fields they pass through, so the incoming direction does not reveal their original location. It seems that the same regions that accelerate the cosmic rays are related to the production of gamma rays, and considering that the photons are unaffected by the magnetic fields, their incoming directions do indicate their production source. The energy of the cosmic rays lies between 10^8 and 10^{20} eV. The most energetic ones produce secondary radiation when they interact with the molecules of the atmosphere called *Extensive Air Showers (EAS)*, and this secondary radiation can be observed from the ground, but the primary particle can only be observed outside the atmosphere. Because of this, several kinds of detectors measure cosmic and gamma rays inside and outside the atmosphere, like satellites and ground-based experiments respectivelly. [Karttunen et al., 2016]

Ground-based experiments detect and characterize the cosmic rays that reach the Earth and interact in the atmosphere, producing an EAS. The first kind of detector is the *Imaging Air Cherenkov Telescope (IACT)* which detects the Cherenkov radiation produced by the secondary particles of the EAS by interacting with the atmosphere; meanwhile, the other kind of detector is a ground-based extensive array, which analyzes the Cherenkov radiation produced by the interaction of the EAS particles with a medium (like water) relying upon ground level.

This thesis shows the characterization process of the IACT called *HAWC's Eye* and the analysis of the hybrid stereoscopic data obtained by the simultaneous performance of HAWC's Eye and the ground-based extensive array *High Altitude Water Cherenkov (HAWC)* observatory during November 2020.

2

INTRODUCTION

In the following chapter the concepts needed to understand the astrophysical context of gamma-ray astronomy are discussed, and the detectors used for gamma-ray studies as well.

2.1. Cosmic-rays

Stable charged particles and nuclei are originated in space, those particles have lifetimes of 10^6 years or longer forming what we call *cosmic radiation*.
Cosmic radiation incident on the Earth's atmosphere is classified as "primary" cosmic rays, and is composed by charged particles and nuclei accelerated at astrophysical sources. Primary cosmic-ray particles include protons, helium nuclei, electrons, and nuclei of most elements of the periodic table of stellar origin, like carbon, iron, oxygen, etc.
Atomic nuclei of practically all elements of the periodic table will be found in cosmic radiation. Free protons account for about 80 % of the primary nucleons and approximately 15 % are nucleons bound in helium nuclei. Electrons constitute about 2 % of the primaries. Nuclei of the periodic table elements other than the previously mentioned (H and He) make up the remaining components of cosmic radiation. Nuclei of the light elements (Li, Be, and B), which constitute secondary cosmic-ray particles, account for a small fraction ($\sim 0.3\,\%$) of cosmic-ray nuclei [L' Annunziata, 2016, Schneider, 2014].
Most galactic cosmic-ray particles possess energies from about 100 MeV to 10 GeV, and primary cosmic-ray nucleon intensity drops rapidly according to the energy beyond several GeV. The primary nucleon intensity from a few GeV to 100 TeV is described by the power law:

$$I_N(E) \approx 1.8\, E^{-\alpha} \text{ nucleons/cm}^2 \text{ sec sr GeV}, \tag{2.1}$$

where E is the energy per nucleon (including rest mass energy) and α is approximately 2.7.
As said before, primary nucleon energies above 1 TeV (i.e., 10^{12} eV) are relatively few in number; and primary cosmic-ray particles with energies above 10^{20} eV are very rare, but has been also reported. The rarity of such extremely high-energy primary cosmic-ray particles can be visualized by the cosmic-ray flux as a function of the nucleon energy shown in Figure 2.1.

Along the energy spectrum three different turning points can be identified. The first one is the "knee", located around particle energies of $10^{15.5}$ eV which shows a decline in the particle flux, then a "second knee" is located at $\sim 10^{17.8}$ eV associated to a change of the spectral index of the particle flux, and the "ankle" region of the spectrum occurring around 10^{19} eV, shows another change of the spectral index of the flux. Measurements with the Pierre Auger Observatory have shown that in the region above the ankle the spectral index γ of the particle flux ($\propto E^{-\gamma}$) changes from $2.51 \pm 0.03(\text{stat.}) \pm 0.05(\text{sys.})$ to $3.05 \pm 0.05(\text{stat.}) \pm 0.10(\text{sys.})$ before changing to $5.1 \pm 0.03(\text{stat.}) \pm 0.10(\text{sys.})$ above the knee (5×10^{19} eV) [Aab, 2020].

The origin of the knee is not well known yet and it is still under discussion. Some theories still favour a particle physical origin due to a change of the interactions in the atmosphere, other theories describes the knee as result of a rigidity dependent cut-off for individual elements and other one calculate the all-particle spectrum as sum spectrum for groups of elements from hydrogen to iron. Meanwhile the second knee is caused by the end of the galactic component of cosmic-rays, i.e. by the cut-off of the heaviest elements. Also, there is much attention on the mechanisms by which the cosmic-ray nucleons are accelerated in space to energies up to 10^{20} eV. Finally, one theory to describe the shape of the tail of the energy spectrum is to associate it to the GZK cut-off[1]. [L' Annunziata, 2016, Knoll, 2010, Hörandel, 2003, Nagano, 2000].

[1] In the highest-energy region, not only deflection by the intergalactic magnetic field, but also the energy losses of cosmic rays in the intergalactic radiation fields, such as microwave, infrared, and radio backgrounds, become important. Soon after the discovery of the cosmic background radiation by Penzias and Wilson (1965), Greisen (1966) and Zatsepin and Kuz'min (1966) predicted that there would be a cutoff in the spectrum of protons around 6×10^{19} eV due to photopion production on the microwave background. This has become known as the GZK cutoff [Nagano, 2000].

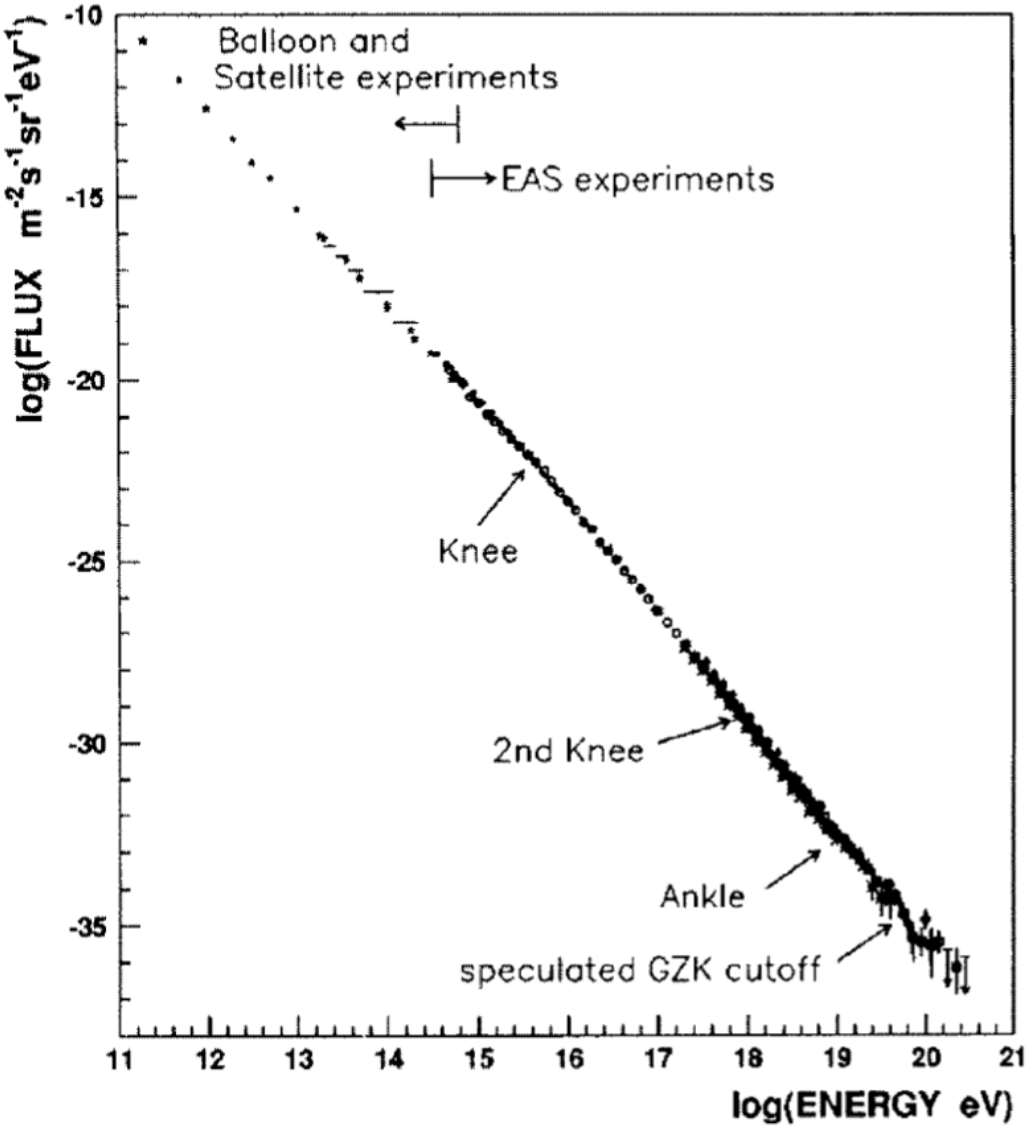

Figure 2.1: Observed energy spectrum of primary cosmic-rays. The spectrum is expressed by a power law from 10^{11} to 10^{20} eV with a slight change of slope around $10^{15.5}$ eV (knee), $10^{17.8}$ eV (second knee), and 10^{19} eV (ankle). The integral fluxes around the "knee" and the "ankle" are approximately 1 per m^2/year and 1 per km^2/year [Nagano, 2000, Hörandel, 2003].

2.2. Gamma-rays

One production method of gamma radiation is electromagnetic radiation emitted by the unstable nucleus of an atom during radioactive decay. When a nucleus is in an unstable state, it may fall to a more stable state by the emission of energy as gamma radiation. Another origin of it is via the phenomenon referred to as electron-positron annihilation whereby a positron encounters an electron, its antiparticle, and the two particles are annihilated. Their annihilation results in the conversion of their mass into energy as gamma radiation. The amount of energy produced by this process is equivalent to the mass of the two electrons annihilated according to Einstein's equation of equivalence of mass and energy [L' Annunziata, 2016].
Another production method is the bremsstrahlung. When fast electrons interact in matter, part of their energy is converted into electromagnetic radiation in the form of bremsstrahlung. The fraction of the electron energy converted into bremsstrahlung increases with increasing electron energy and is largest for absorbing materials of high atomic number. Also, most commonly-available gamma-ray sources decay by beta-minus emission, and the source encapsulation is usually also thick enough to stop these beta particles. In other cases, an external absorber may be used to prevent the beta particles from reaching the detector where their energy deposition would needlessly complicate the gamma-ray spectrum. In the absorption process, however, some secondary radiation in the form of bremsstrahlung will be generated and may reach the detector and contribute to the measured spectrum. In principle, the bremsstrahlung spectrum may extend to an energy equal to the maximum beta particle energy, but significant yields are confined to energies that are much lower than this value. Because these spectra are continua, they do not lead to peaks in the recorded spectra but rather can add a significant continuum on which all other features of the gamma-ray spectra are superimposed. Because the bremsstrahlung contribution cannot simply be subtracted as a background, its inclusion can lead to errors in quantitative measurements of areas under peaks in the gamma-ray spectrum. To minimize the generation of bremsstrahlung, the use of beta absorbers made from low atomic number materials, such as beryllium, is often preferred [Knoll, 2010].
The advantage of using gamma-rays to study objects in the Universe is that their detected arrival direction is in the same direction where the source that produced it is located, because they are not charged particles, so they are not deflected by magnetic fields in the Universe, unlike hadrons. Also, must of the gamma-ray sources are ultra-high cosmic-ray sources as well.

There are some production mechanisms of very-high-energy (VHE) gamma-rays[2], the first example of this acceleration process is the *hadronic model*, which consists in the production of secondary mesons due to high-energy protons interacting with low-energy photons in the surroundings of sources (also called *photoproduction*) [Spurio, 2014]:

$$p + \gamma \rightarrow \Delta^+ \rightarrow \pi^0 + p, \tag{2.2}$$

where Δ^+ is the resonance associated with the photoproduction and it is ~ 0.250 mb. Then, neutral pions decay into gamma-rays via the process:

$$\pi^0 \rightarrow \gamma\gamma, \tag{2.3}$$

where each photon has an energy of $E^*_\gamma = m_\pi c^2/2 = 67.5$ MeV and a momentum opposite to each other in the rest of frame of the neutral pion. When a E^{-2} energy spectrum of accelerated protons at the source is considered, the π^0-decay spectrum for an observer in the laboratory frame in the $E^2_\gamma \frac{\mathrm{d}N}{\mathrm{d}E_\gamma}$ representation raises steeply below ~ 200 MeV and approximately traces the energy distribution of parent protons at energies grater than few GeV. If the resonance mass $m_\Delta = 1.232$ GeV and the proton mass $m_p = 0.938$ GeV are considered, the collision with the CMB with a photon of average energy of $E_\gamma = 1.2 \times 10^{-3}$ eV and with a collision angle of $\theta = \pi$, have a threshold energy of:

$$E_p = \frac{m^2_\Delta - m^2_p}{4E_\gamma} = 1.2 \times 10^{20} \text{ eV} = 1.2 \times 10^8 \text{ TeV}. \tag{2.4}$$

The threshold decreases when the interaction happens with the CMB photons in the high-energy tail of the spectrum. The effect becomes significant for protons with $E \simeq 5 \times 10^7$ TeV. This characteristic spectral feature is shown in Figure 2.2 (green solid line). This process is often referred to as the pion-decay bump and it uniquely identifies the presence of gamma-rays produced by π^0-decays. In this figure it is assumed that primary protons are accelerated up to ~ 1 PeV, and that secondary gamma-rays carry a few percent of the primary energy.
On the other hand, we have the *leptonic model* in which the production of high-energy photons is the so-called *Self-Synchrotron Compton (SSC)* mechanism. Synchrotron emission from electrons moving in the magnetic fields generates photons, which constitute a target for their parent electron population. So, the process in which low-energy photons gain energy by colliding with high-energy electrons is the *inverse Compton (IC)* scattering. This mechanism increases the

[2]The high-energy (HE) gamma-rays are those with energies between 100 MeV and 100 GeV, and the very-high-energy (VHE) gamma-rays are the ones with energies of 100 GeV to 100 TeV [Spurio, 2014].

photon's energy and is important in regions where accelerated electrons coexist with a high-energy density of soft photons [Spurio, 2014].

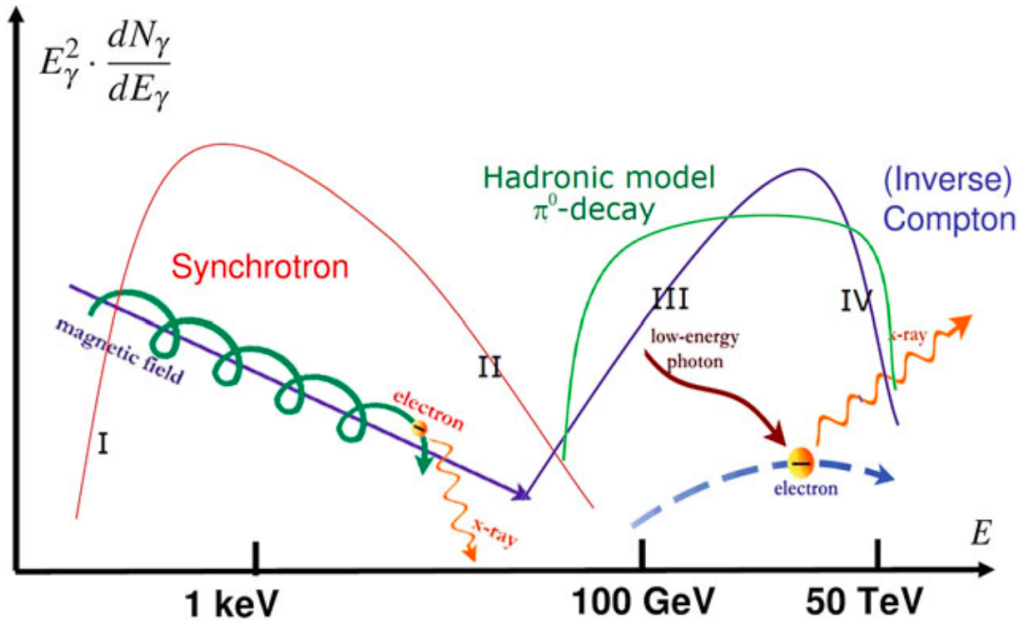

Figure 2.2: Spectral energy distribution of photons produced in leptonic/hadronic models. Superposition of gamma-rays from both leptonic and hadronic mechanisms is assumed in the case of mixed models. [Spurio, 2014]

2.3. Extensive air showers

Extensive Air Showers (EAS) are initialized by a primary particle through the interaction with a nucleus in the atmosphere. Most of the particles on the EAS travel at velocities close to the speed of light in the atmosphere along the direction of the primary particle.
VHE primary gamma-rays induce an almost pure electromagnetic cascade, containing only e^-, e^+ and gamma-rays. Electromagnetic showers are governed mainly by bremsstrahlung of electrons (dominant for energies $E > E_c \simeq 86$ MeV[3] and a radiation length of $X_0 \simeq 37\ \mathrm{g \cdot cm}^2$[4]) and positrons and pair production of photons

[3] E_c is the critical energy at which radiation energy losses dose deriving from excitation/ionization. This value depends on the material; for air the critical energy is $E_c \simeq 86$ MeV [Spurio, 2014].

[4] For this case, the radiation length X_0 is for the air.

(for energies $E > 1.02$ MeV). In addition to bremsstrahlung, electrons and positrons also loos energy by excitation/ionization of the medium. The main difference between an EAS initiated by a photon and a EAS induced by a primary proton or nucleus is the presence of a hadronic component in the second case, which develops a significant muon cascade [Spurio, 2014, De Angelis and Pimenta, 2015]. Figure 2.3 shows a simplified developing process of hadronic and electromagnetic showers [L' Annunziata, 2016, De Angelis and Pimenta, 2015].

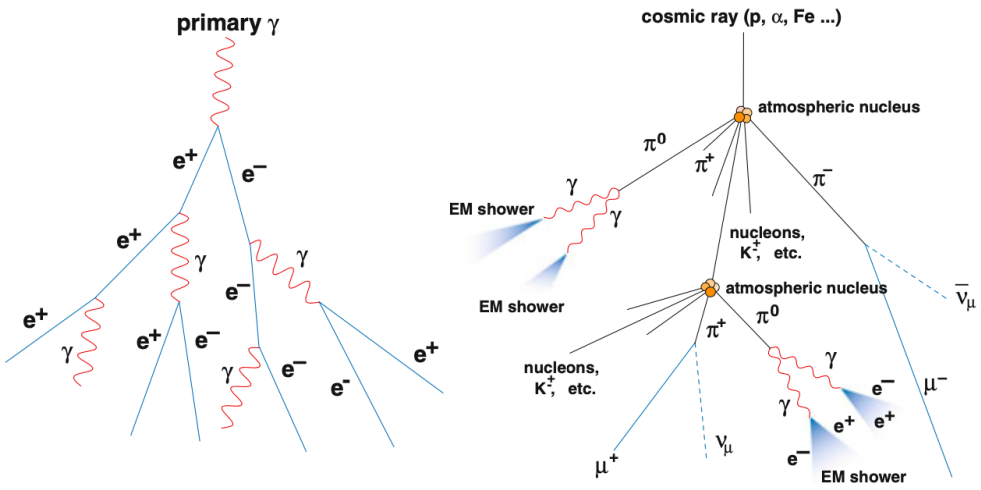

Figure 2.3: Schematic representation of two atmospheric showers initiated by a photon (left) and by a proton (right). [De Angelis and Pimenta, 2015]

2.4. Cherenkov radiation

Many secondary particles in the EAS are superluminal, and they thus emit Cherenkov light that can be used for the detection.
The Vavilov-Cherenkov radiation (commonly called just Cherenkov radiation) occurs when a charged particle moves through a medium faster than the speed of light in the medium. The total energy loss due to this process is negligible. The light is emitted in a coherent cone (shown in Figure 2.4) at an angle such that:

$$\cos\theta_c = \frac{1}{n\beta}, \tag{2.5}$$

from the direction of the emitting particle. The threshold velocity is obtained from $\beta = 1/n$, where n is the refractive index of the medium.
The number of photons produced per unit path length and per unit energy interval of photons by a particle with charge $z_p e$ at the maximum angle is:

$$\frac{\mathrm{d}^2N}{\mathrm{d}\lambda\,\mathrm{d}x} \simeq \frac{2\pi\alpha z_p^2}{\lambda^2}\sin^2\theta_c, \tag{2.6}$$

where the index of refraction n is, in general, a function of photon energy E; Cherenkov radiation is relevant when $n > 1$ and the medium is transparent, and this happens close to the range of visible light.
The total energy radiated is small, some 10^{-4} times the energy lost by ionization. In the visible range (300-700 nm), the total number of emitted photons is about 40/m in air, and about 500/cm in water. Due to the dependence on λ, Cherenkov detectors must be sensitive close to the ultraviolet region [L' Annunziata, 2016, De Angelis and Pimenta, 2015].

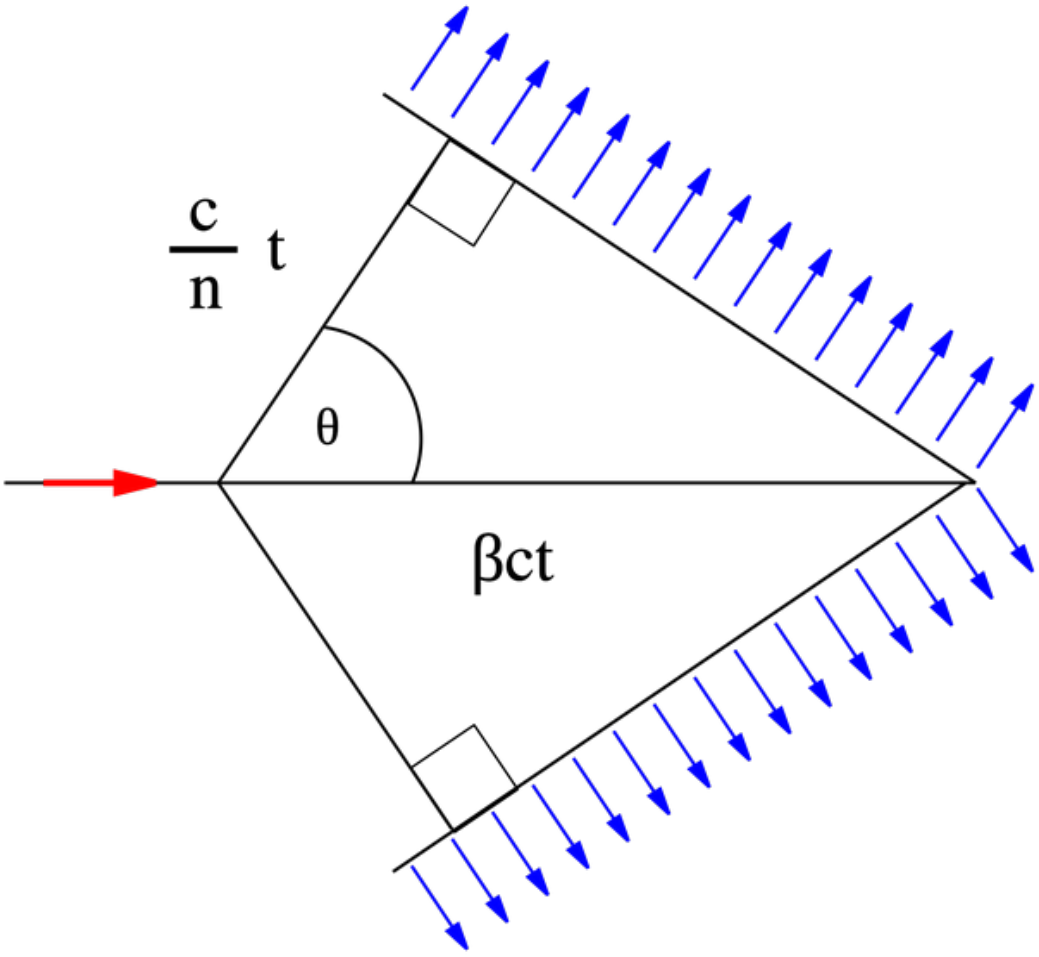

Figure 2.4: Schematic representation of Cherenkov radiation by a charged particle. [De Angelis and Pimenta, 2015]

2.5. Particle detectors

A particle detector aims to measure the momenta and to identify the particles that pass through it after being produced in a collision or a decay; this is called an *event*. The position in the space where the event occurs is known as the interaction point.
To identify every particle produced by the collision and plot the paths they have taken (i.e., to "completely reconstruct the event"), it is necessary to know the masses and momenta of the particles themselves. The mass can be computed by measuring the momentum and either the velocity or the energy. [De Angelis and Pimenta, 2015]
Different instruments allow these measurements, like fluorescence detectors, scintillators, cloud and wire chambers, Cherenkov detectors, and much more. This work will be focused on the Cherenkov detectors.
Due to the conversion probability in the atmosphere, only satellite-based detectors can detect primary X/γ-rays. However, satellites are small, with maximum dimensions of about 1 m^2 because of the cost of space technology. If the energy of the primary particle is large enough, some of the products of the shower generated by the interaction with the atmosphere can reach ground-based detectors. It is appropriate to build such detectors at high altitudes, where atmospheric dimming is lower. The area sampled by ground-based detectors can be much larger than the typical areas of satellites. Since the fluxes of high-energy photons are low and decrease rapidly with increasing energy, VHE, and Ultra-High Energy (UHE) gammas[5] can be detected only from the atmospheric showers they produce, i.e., employing ground-based detectors. This fact clarifies another meaning of the division between HE and VHE photons: HE photons are detected using satellites, while for VHE photons the detection using ground-based detectors becomes possible.
The characteristic of the ground-based experiments are presented in what follows [De Angelis and Pimenta, 2015].

2.5.1. Imaging Air Cherenkov Telescopes

Imaging Air Cherenkov Telescopes (IACTs) are essentially wide-field optical telescopes consisting of a large reflector that reflects the light (the *image*) into a high-speed multi-photosensor camera in the focal plane. Short exposures are required to detect the faint flashes of Cherenkov light against the Poisson fluctua-

[5] The high-energy (HE) gamma-rays are those with energies between 100 MeV and 100 GeV, the very-high-energy (VHE) gamma-rays are the ones with energies of 100 GeV to 100 TeV, and the ultra-high-energy (UHE) gamma-rays are those with energies $>$ 100 TeV [Spurio, 2014].

tion[6] in the night-sky background. An IACT must be operated in almost total darkness (as other telescopes), thus it must be installed far from human environments. These telescopes operate usually on moonless nights, limiting the duty cycle to $10-15\,\%$. High-speed detectors and electronics are required to minimize the integration time, the amount of time the chip spends "counting photons". Ideally, the integration time should be reduced down to the shortest intrinsic timescale of the Cherenkov light wavefront, which corresponds to a few nanoseconds. Longer integration time reduces the signal-to-noise.
The field-of-view (FoV) of IACTs is $\sim 4^\circ$ which is substantially larger than most optical telescopes. This FoV allows to obtain images of showers whose impact parameters on the ground extend several meters away. These regions of the sky containing one or more source candidates are usually targeted for observations. Surveys can only be accomplished slowly, by tiling regions of the sky with overlapping FoVs. The energy interval from which the current generation of IACTs is sensitive ranges from 100 GeV to 100 TeV. Their angular resolution is of the order of 0.1°. Their sensitivity is sufficient to detect the Crab nebula in some minutes, and a source with $1\,\%$ of the Crab flux in a few hours[7]. Like most very large optical telescopes, IACTs typically make use of an altitude-azimuth drive for tracking sources during large exposures. The angular resolution reached with the IACT technique allows resolving important substructures of some sources.
Current telescopes are based on either simple parabolic reflectors or many individual mirror segments having a radius of curvature equal to the focal length, placed on an optical support structure (as HESS, VERITAS or MAGIC, which is shown in Figure 2.5) [Spurio, 2014].

2.5.2. Wide-Field Detectors

The WFD, designed for the detection of CRs at PeV and TeV energies, can be adopted also for gamma-ray astronomy. The mandatory requirement is that the energy threshold is reduced by two or three orders of magnitude, using dense particle arrays located at very high altitudes. The feasibility of the measurement at the ground level of showers initiated by a gamma-ray has been successfully demonstrated by different experiments. [Spurio, 2014]
The Wide-Field Detectors (WFD) are large arrays of detectors sensitive to charged secondary particles generated in the atmospheric showers. They have a high duty cycle and a large FoV, but relatively low sensitivity. The energy threshold of such detectors is rather large.

[6] The Poisson fluctuation is described in Appendix A.

[7] Note that a source with a flux equal to $1\,\%$ of the Crab is not detected in 100 minutes. The statistical significance of a signal excess depends on the background level, and this increases linearly with the observation time.

Figure 2.5: MAGIC (Major Atmospheric Gamma Imaging Cherenkov) is a system of two 17 m diameter IACTs. The MAGIC telescopes are located at a height of 2200 m a.s.l. on the Roque de Los Muchachos European Northern Observatory on the Canary Island of La Palma. [MAGIC, 2021]

The principle of operation is the same as the one for the UHE cosmic rays detectors like Auger, i.e., direct sampling of the charged particles in the shower. This can be achieved:

- either using a sparse array of scintillator-based detectors;
- or by an effective covering of the ground, to ensure efficient collection and hence lower the energy threshold.

The energy threshold of a WFD is at best in the $0.5 - 1$ TeV range, so they are built to detect UHE photons as well as the most energetic VHE gammas. At such energies, fluxes are small and large surfaces of the order of $\sim 10^4$ m are required. Concerning the discrimination from the charged cosmic ray background, muon detectors devoted to hadron rejection may be present. Otherwise, it is based on the reconstructed shower shape. The direction of the detected primary particle is computed from the arrival times with an angular precision of about $\sim 1^\circ$. The calibration can be performed by studying the show in the reconstructed directions caused by the Moon. The energy resolution is poor [De Angelis and Pimenta, 2015].

2.5.3. Hybrid detection

As previously explained, IACT and WFD are the principal ground-based detectors used for gamma-ray astronomy. Each one has its own advantages and disadvantages depending on the technique, therefore combining both techniques for observation is a promising solution to improve measurements. Also, the experiments can make a cross-callibration between each other with observational data.

Figure 2.6: The MILAGRO (Multiple Institution Los Alamos Gamma Ray Observatory) consists of a man-made pond lined on the bottom, covered on top, and filled with water. The MILAGRO detector is located in the Jemez Mountains near Los Alamos, New Mexico at an elevation of 2,650 m [MILAGRO, 2021].

So, considering that for this particular case the experiments used are the IACT and a WFD, the implementation of a hybrid technique between this both experiment is discussed. In one hand, the IACT can not estimate correctly the impact position of the EAS's core by themselves. Also, even that IACTs have an excellent angular resolution, EAS produced by different primary particles of different energies can produce similar images in the IACT because the distance of the EAS axis depends directly on the energy reconstruction of the telescopes, i.e. the light-pool produced by a high-energy shower far away from the telescope can be similar to the one produced by a low-energy shower near the telescope. This is shown in Figure 2.7. Meanwhile, the IACTs can make a good estimation of the shower age because they observe the whole shower development through the atmosphere.
In the other hand, a WFD records the information obtained from shower slices that reaches the array, so then the particle density of these slices depends on the energy of the primary particle, the amount of atmosphere that the shower pass through (shower age) which also depends on the altitude where is located the WFD. Hence, to have a good estimation of the primary energy, the shower age must be correctly estimated, but a WFD can not make a good estimation of the shower age because a high-energy shower with a larger age (more ammount of atmosphere crossed) can produce a similar image than a low-energy shower with a shortest age (less ammount of atmosphere crossed). Meanwhile, considering that a WFD

is an array of small particle detectors, the impact position of the shower's core can be correctly estimated, as shown in Figure 2.7.

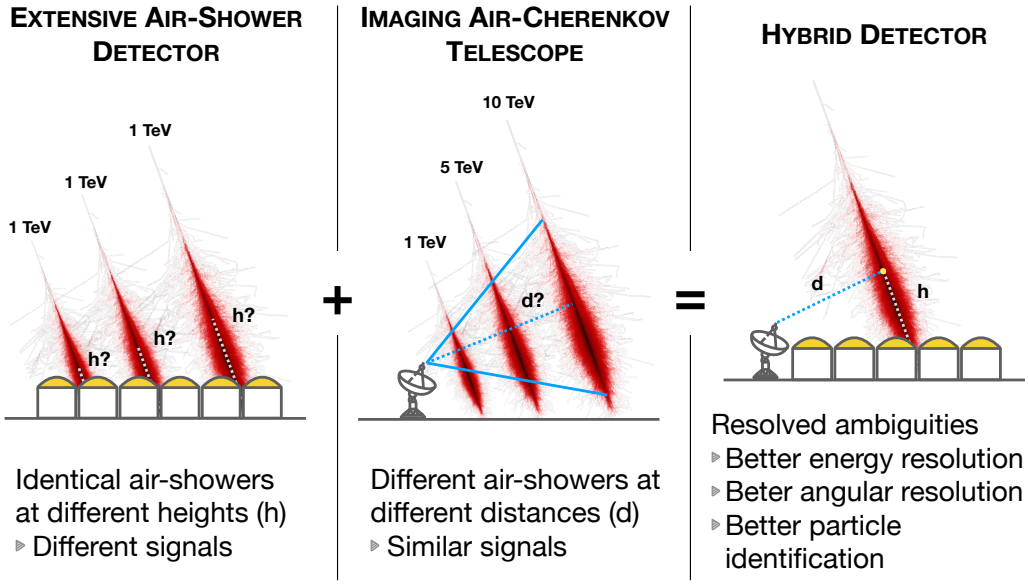

Figure 2.7: A WFD can not estimate correctly the shower age because showers with different energy and age can produce a similar detection, but these experiments can estimate correctly the impact position of the shower's core. Then, the IACTs can estimate correctly the shower age of a EAS, but they can not make a good estimation of the EAS that is observed to the telescope. Because of this, combining different observation techniques can solve ambiguities and improve measurements.

In this work, hybrid detection was performed and analyzed using two compact IACTs called *HAWC's Eye* and they worked in hybrid performance with the *High Altitude Water Cherenkov (HAWC)* Observatory which is a WFD. In the next chapter, both experiments are discussed.

3

DETECTORS OF THE HYBRID SETUP

The following chapter is dedicated to explaining the experiments used to make hybrid detection. First, the *High Altitude Water Cherenkov (HAWC) Observatory* is described, which is an EAS array. Then, the next section is focused on the IACT *HAWC's Eye*.

3.1. The High Altitude Water Cherenkov Observatory

The High Altitude Water Cherenkov (HAWC) Observatory is an instrument sensitive to multi-TeV hadron and gamma-ray EAS, operating at the coordinates of 18°59'41"N, 97°18'27"W at an altitude of 4,100 m a.s.l. at the volcano Sierra Negra, in the state of Puebla, Mexico. HAWC consists of a large 22,000 m^2 area densely covered with 300 Water Cherenkov Detectors (WCDs). Each WCD consists of a 7.3 m diameter, 5 m tall steel tank lined with a plastic bladder, and 200,000 L of purified water. The array has an external layout conformed of 345 outriggers, which are smaller WCDs of 1.65 m diameter and 1.55 m tall, also filled with water. Ifncluding the outriggers area, the HAWC's footprint grows up to 100,000 m^2. At the bottom of each WCD, three 8-inch Hamamatsu R5912 Photomultiplier Tubes (PMTs) are anchored in an equilateral triangle of side length 3.2 m, with one 10-inch high-quantum-efficiency Hamamatsu R7081 PMT anchored at the center. For the outriggers, they have one 10-inch PMT anchored at the center of its base. Figure 3.2 shows a representation of the HAWC array, indicating the dimensions of the WCD and the outriggers, and also the location of the PMTs respectively.

Figure 3.1: The HAWC Observatory. At the center of the array are located the 300 WCD, and in the surroundings are distributed 345 outriggers. In the background, the volcano "Pico de Orizaba" is another active volcano. [HAWC, 2021b]

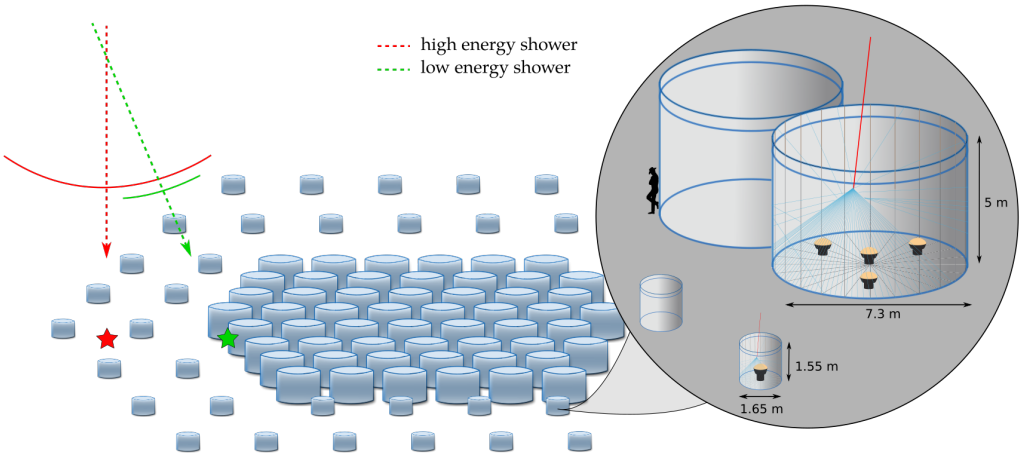

Figure 3.2: Representation of the layout of HAWC, indicating the sizes of the WCD and the outriggers, and also the location of the PMTs inside each one of these detectors. [HAWC, 2021a]

The high altitude of HAWC sets the scale for the photon energy that can be detected. The detector is fully efficient to gamma-rays with primary energy above ~ 1 TeV. Lower-energy photons can be detected when they fluctuate to interact deeper

in the atmosphere than typical ones.
PMT pulses are amplified, shaped, and passed through two discriminators, and digitized. The amount of time that PMT pulses spend above their thresholds is used to estimate the total amount of charge collected in the PMT.
The data from the front-end electronics are digitized with commercial Time-to-Digital Converters (TDCs) and passed to a cluster of computers for real-time triggering and processing. Events are preserved in the computer cluster if they pass the trigger condition: a simple multiplicity trigger, requiring some number, $N_{\text{threshold}}$, of PMTs, hit within 150 ns.
The reconstruction of EAS involves determining the direction, the likelihood for the event to be a photon, and the event's size.
The strength of HAWC over the IACT technique is that photon showers may be detected across its entire ~ 2 sr of FoV of the instrument, day or night, regardless of weather conditions, and also it is uniquely suited to study the long-duration light curve of objects and to search for flaring sources in real-time. Additionally, since sources are observed on every transit, HAWC obtains thousands of hours of exposure on each source, greatly improving the sensitivity to the highest-energy photons [Abeysekara, 2017].
Events from the detector are reconstructed to determine the arrival direction of the primary particle and the size of the resulting EAS on the ground, a proxy for the primary particle's energy. The Direction reconstruction happens in two steps: first the core reconstruction and then the direction determination; both are discussed too in what follows. The EAS core, the dense concentration of particles along the direction of the original primary is needed to make the best reconstruction of EAS's direction.

3.1.1. Hit selection and event size bins

The HAWC Data Acquisition System (DAQ) records 1.5 μs of data from all PMTs that have a hit during an EAS event. A subset of these hits is selected for the EAS fit. To be used for the fit, hits must be between -150 and +400 ns around the trigger time. Different cuts are applied to remove hits that can not be correctly calibrated or are associated with afterpulses or contaminating signals. Channels are considered available for reconstruction if they have a live PMT taking data that have not been removed by one of these cuts.
The angular error and the ability to distinguish photon events from hadron events are strongly dependent on the energy and size of events on the ground. The data are divided into nine size bins, $\mathscr{B}$. The size of the event is defined as the ratio of the number of PMT hits used by the event reconstruction to the total number of PMTs available for reconstruction, f_{hit}. This definition allows for the relative stability of the binning when PMTs are occasionally taken out of service.

Figure 3.3 shows the distribution of true energies as a function of the $\mathscr{B}$ of the events. The distribution of the energies naturally depends heavily on the source itself, both its spectrum and the angle at which it culminates during its transit. [Abeysekara, 2017]

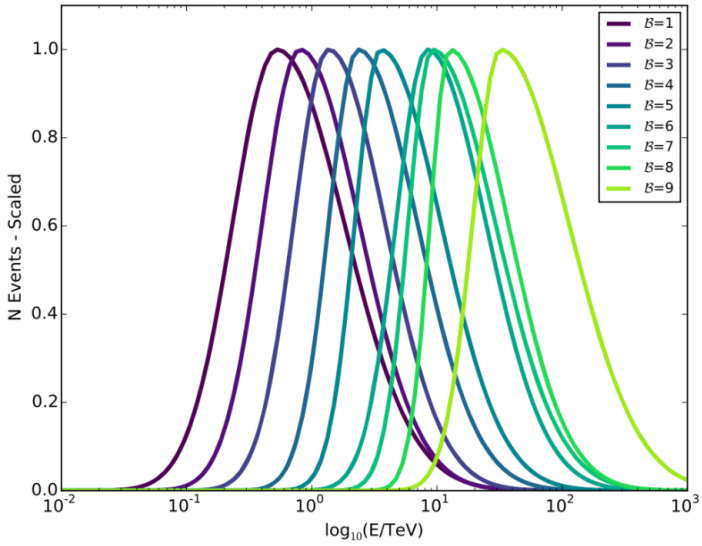

$\mathcal{B}$	f_{hit}
1	6.7 %-10.5 %
2	10.5 %-16.2 %
3	16.2 %-24.7 %
4	24.7 %-35.6 %
5	35.6 %-48.5 %
6	48.5 %-61.8 %
7	61.8 %-74.0 %
8	74.0 %-84.0 %
9	84.0 %-100.0 %

Figure 3.3: *Left*: fits to the true energy distribution of photons from a source with a spectrum of the form $E^{-2.63}$ at a declination of +20°N for $\mathscr{B}$ between 1 and 9, summed across a transit of the source. The curves have been scaled to the same vertical high for display. *Right*: ranges in which the data are divided into nine size bins $\mathscr{B}$ in function of the f_{hit}. [Abeysekara, 2017]

3.1.2. Core reconstruction

Considering an EAS, the concentration of secondary particles is highest along the trajectory of the original primary particle, termed the EAS core. Determining the position of the core in the ground is key to reconstructing the direction of the primary particle.
The Photo-Electron (PE) distribution on the ground is fit with a function that decreases monotonically with the distance from the shower core. The signal in the $i-$th PMT, S_i, is presumed to be:

$$\begin{aligned} S_i &= S(A,\vec{x},\vec{x_i}) \\ &= A\left[\frac{1}{2\pi\sigma^2}e^{-\frac{|\vec{x_i}-\vec{x}|^2}{2\sigma^2}}+\frac{N}{(0.5+|\vec{x_i}-\vec{x}|/R_m)^3}\right], \end{aligned} \tag{3.1}$$

where,

S_i	-	Signal of the $i-$th PMT
A	-	Overall amplitute
$\vec{x}$	-	Core location
$\vec{x_i}$	-	$i-$th core position
σ	-	Gaussian width (fixed to 10 m)
N	-	Normalization of the tail (fixed to 5×10^{-5})
R_m	-	Molière radius ($\approx$ 120 m for HAWC)

3.1.3. Direction reconstruction

In first order approximation, particles from the EAS arrive on a plane defined by the speed of light and direction of the primary particle. But, in fact, the shower front is curved, since the shower particles originate from a common interaction point. In practice, this means that particles detected near the shower core are observed to arrive earlier than particles far from the core. Generally, the shower front is several nanoseconds thick near the core and wider far from the core. The curved shape of the EAS front is shown in Figure 3.4.

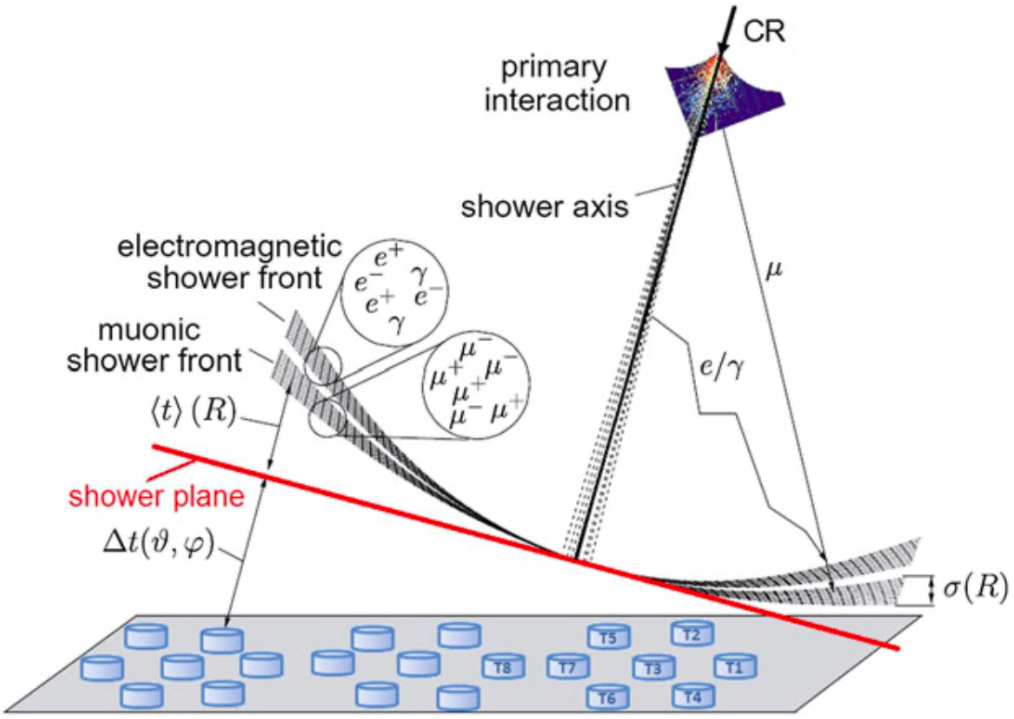

Figure 3.4: Sketch of the development of EM and muonic showers in the atmosphere, produced by the interaction of a primary proton or nucleus (see text for details). [Spurio, 2014]

Since particle density is higher near the core than in the shower periphery, there

is a resulting position-dependent shower timing offset, which will be called *sampling*.
A combined curvature/sampling correction (a function of the distance of hits from the shower core and the total charged recorded in the PMT) is used to account for the deviation of the front shape compared to a plane.
After correcting for the sampling and curvature, the angular fit is a simple χ^2 planar fit. [Abeysekara, 2017]

3.1.4. Photon/hadron separation

For HAWC, hadronic cosmic rays constitute the main background to high-energy photon observation. As previously mentioned, the morphology of an EAS produced by a hadron or a photon is very different, and for HAWC this is very important, particularly for showers above several TeV.
Two parameters are used to identify cosmic ray events. The first parameter, *compactness* $\mathscr{C}$, is defined as:

$$\mathscr{C} = \frac{N_{\text{hit}}}{CxPE_{40}}, \tag{3.2}$$

where,

N_{hit} - Number of PMT hits during the EAS
$CxPE_{40}$ - Effective charge measured in the PMT with the largest effective charge outside a radius of 40 m from the shower core

On the other hand, hadronic showers have sporadic high-charge hits far from the EAS'center. This clumpiness is characteristic of hadronic showers and arises from a combination of penetrating particles (primarily muons) and hadronic subshowers that are largely absent in photon-induced showers. So, the clumpiness of an EAS is quantified by a parameter $\mathscr{P}$, termed the *PINCness* (short of *Parameter for Identifying Nuclear Cosmic rays*) of an event. $\mathscr{P}$ is defined as: [Abeysekara, 2017]

$$\mathscr{P} = \frac{1}{N}\sum_{i=1}^{N}\frac{(\zeta_i - \langle\zeta_i\rangle)^2}{\sigma_{\zeta_i}^2}, \tag{3.3}$$

where,

ζ_i - $\left[= \log_{10}\left(Q_{\text{eff},i}\right)\right]$ Is the logarithm of the charge $Q_{\text{eff},i}$
$Q_{\text{eff},i}$ - Effective charge for each of the PMT hits, i
$\langle\zeta_i\rangle$ - Average of the charge ζ_i
σ_{ζ_i} - Errors of the charge ζ_i
N - Number of PMT hits

3.2. The IACT HAWC's Eye

The HAWC's Eye telescopes are a pair of compact light-weight IACTs developed as a possible extension of the HAWC Observatory, allowing hybrid measurements of the EAS. This design was adapted from the FAMOUS fluorescence telescope developed for the Pierre Auger Observatory [Niggemann et al., 2015]. For the HAWC's Eye telescope, the design was adapted to observe photon-induced EAS. A very similar telescope, called IceAct, was constructed for the IceCube-Gen2 extension of the IceCube detector at the south pole [Schaufel et al., 2019, Aartsen, 2020].
In the following section, the telescope prototype is described, naming the principal improvements done from the previous version of the telescopes. Also, the EAS detection and reconstruction techniques are explained below.

Figure 3.5: One of the two HAWC's Eye IACTs inside the grey shield, located beside a WCD of the HAWC array.

3.2.1. HAWC's Eye hardware design

Figure 3.6 shows an outline of the HAWC's Eye design. At the top is located a Fresnel lens of 549.7 mm. The lens is located over a carbon-fiber barrel that is light-tight, and it is 503.4 mm tall. Then, at the bottom of the barrel, a base of Winston cones are centered and joined to the Silicon Photomultipliers (SiPMs) sensors which will be used to collect the Cherenkov light. Finally, under the SiPMs mount, there is an enclosure that contains the electronics needed for the data acquisition.

3.2.2. Optical design and camera

In the upper part of the telescope, light reaches the aperture of the telescope and it gets focused on a focal plane with the Fresnel lens. The lens model SC934[1], has a diameter of 549.7 mm and a thickness of 2.5 mm. This is made of Polymethyl Methacrylate (PMMA). Simulations using GEANT 4 have shown that the focal distance must be 503.35 mm, so it will get the minimum Point Spread Function

[1] Manufactured by ORAFOL Fresnel Optics GmbH

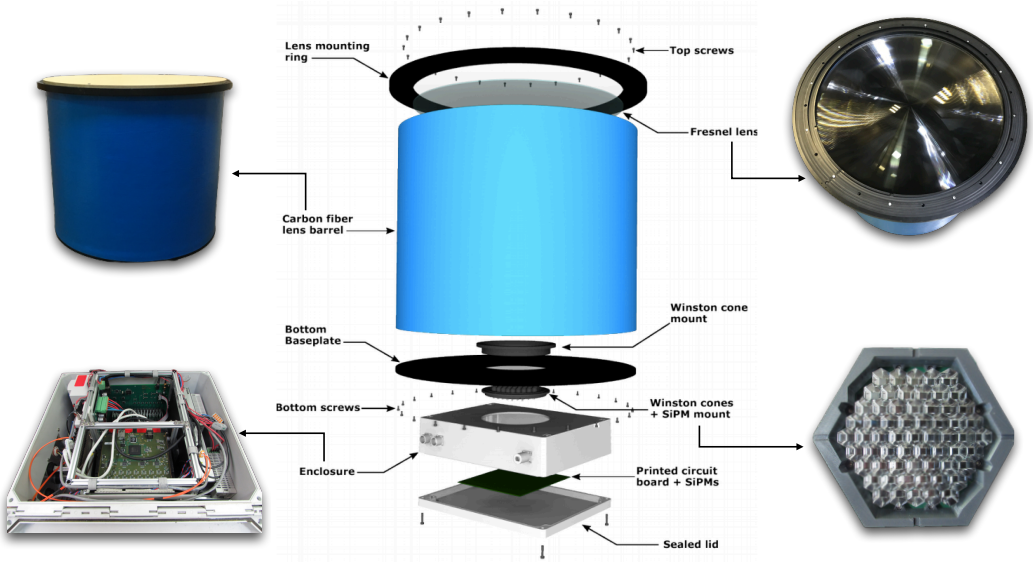

Figure 3.6: Exploded assembly drawing of the telescope construction. Based from [Schaufel, 2017].

(PSF) at the most efficient wavelength of the system approximately 441 nm[2]. Additionally, the lens can be covered with a wooden lid, so that it is protected from external stress and damage to the lens are prevented.
In the focal plane is located a 61 hex-to-square light collectors mount made from PMMA too. These have a length of 23.5 mm and collect the focused light. Each light collector has a hexagonal window (area $\approx$ 190 mm^2), and the light is guided to a squared window (area = 6 mm^2) using Winston-shaped surfaces. Figure 3.7 shows the Winston cones light collectors of a camera and a model of one single light collector.
The window exit of the light collectors is glued to a camera whose pixels are SiPMs of the type MicroFJ-60035-TSV (SenseL) by ON Semiconductor [ON-Semiconductor, 2021]. Implementing the light collectors on the camera has the advantage that the effective area of each SiPM is enlarged, so the total effective area is enlarged too. Also, if the light collectors are implemented, the stray light is not detected by the SiPM due to the special shape of its surface. [Audehm, 2020] Each SiPM has about 1.6° FoV of the sky, so if a maximal inner circle is considered into the hexagonal light collector array, the total FoV of the telescope is $\sim$ 12°. On Table 3.1 the characteristics of the SiPMs SenseL used are specified.
Each camera has 61 SiPM pixels with a Wiston cone light collector each, but there are three additional SiPM "blind" pixels. Those pixels are considered blind becau-

[2]The manufacturer states a different focal length for the lens. It states a distance of 502.1 mm for a wavelength of (546 $\pm$ 27) nm and considering perpendicular light.

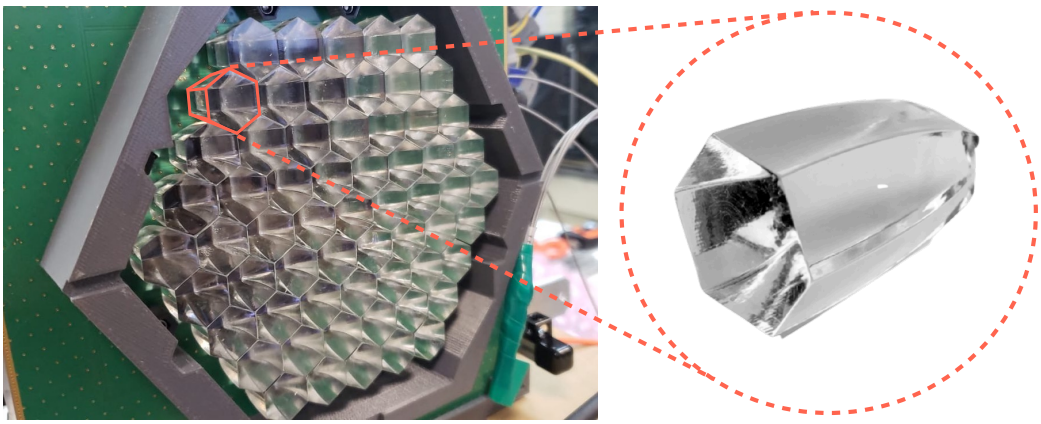

Figure 3.7: *Left*: the complete array of light collectors that conform to the camera of one telescope. *Right*: a Winstone cone light collector made of PMMA which collects and focuses the light on the SiPMs.

Parameter	**MicroFJ-60035-TSV (SensL)***
Active area [mm^2]	6.07×6.07
Cell size [μm]	35
Number of microcells	22292
Fill factor [%]	75
Breakdown voltage [V]	24.5 ± 0.25
Overvoltage [V]	1 to 6
Temperature coefficient [mV °C^{-1}]	21.5
Gain	5.3×10^6
Spectral range [nm]	200 to 900
Most efficient wavelength λ_p [nm]	420
PDE at λ_p [%]	48.5
Dark count rate [MHz]	2.95
Crosstalk [%]	22
Operation temperature range [°C]	-40 to +85

* Values are measured for 5V overvoltage and 21 °C

Table 3.1: SenseL SiPM characteristics used for the camera of the telescopes HAWC's Eye. The values are taken from the corresponding datasheets [SenseL, 2021]

se they do not have a light collector and they are located at the periphery of the camera. These blind pixels are used for monitoring noise and are not included in the trigger of the telescope. Figure 3.8 shows the three blind pixels of the camera. The first camera of this type was commissioned in the First G-APD Cherenkov

Telescope (FACT) in 2011 [Anderhub et al., 2013].

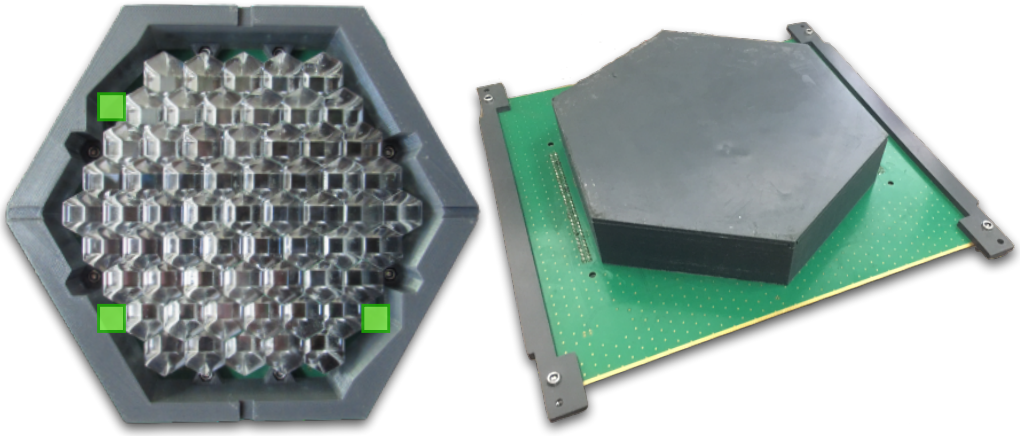

Figure 3.8: *Left*: The blind pixels of the camera are located at the periphery of the SiPM array and are pointed with green squares. None of these three SiPMs has light collectors. The top-left and bottom-right pixels are open to the stray light to measure the night sky background; meanwhile, the bottom-left pixel is isolated from the light and is used to measure the dark count rate of the SiPM. *Right*: Hexagonal 3D-printed light-tight shield that protects the camera from impacts.

The SiPM and light collectors mount is covered with a hexagonal 3D-printed shield that also is light-tight, so the instrument is protected against environmental stress or collisions. This shield has a lid that can be taken out to perform the observations or be put back on to protect the system.
Finally, the lens and the camera are joined by a carbon fiber barrel which has a black cover inside and is black painted too, from being light-tight and prevent stray light to be reflected inside the system and producing noise. This barrel is 622 mm in diameter and 510 mm tall.
Because of the previously described design, the camera, the Fresnel lens, and the electronics are protected against external factors, so it makes the telescopes to be easy to transport, also considering the telescope is light-weight and compact.

3.2.3. Silicon photomultiplier

Unlike PMTs, SiPMs are solid-state photodetectors. SiPMs use the photoelectric effect similar to PMTs and amplifying this current between several dynodes. SiPMs work with low voltage, are unaffected by magnetic fields, and are compact and robust, because of this, they are appropriate for the telescope camera. Some SiPMs of the HAWC's Eye camera are shown in Figure 3.9.

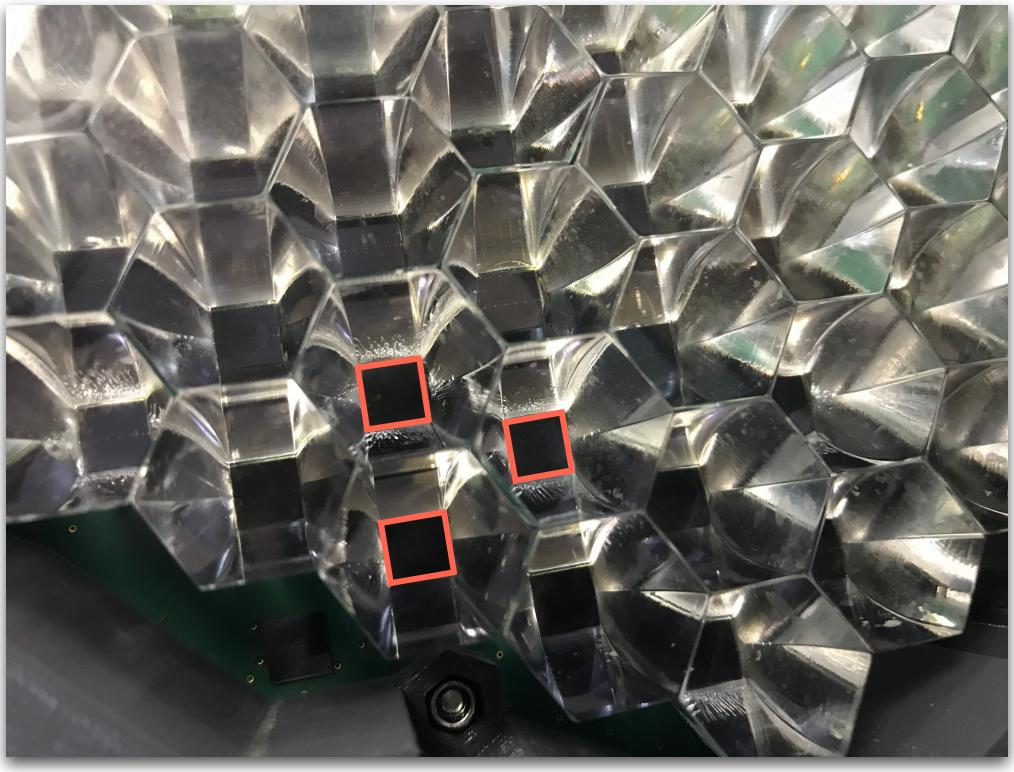

Figure 3.9: Three of the 64 SenseL SiPMs used in the HAWC's Eye camera, pointed with red squares. The effective area of each one is 6.07×6.07 mm^2.

A SiPM is formed of a large number (thousands) of microcells. Each microcell is a Geiger-mode Avalanche Photodiodes (G-APDs) with its own quench resistor and a capacitively coupled fast output. These microcells are arranged in a close-packaged array with all the like terminals (e.g. all of the anodes) summed together. The array of microcells can thus be considered as a single photodiode sensor with three terminals: anode, cathode, and fast output, as shown in Figure 3.10 [ON-Semiconductor, 2021].

Since the photodiode is operated in Geiger mode, all generated pulses have the same size, not depending on the energy of the triggering photon or the number of simultaneously impinging photons; the pulse height can be varied by the distance of the applied voltage from the breakdown voltage. The gain of the SiPM is proportional to this overvoltage.
In the total SiPM, more than one G-APD can get triggered simultaneously due to a high photon flux. So, the signal of each triggered G-APD contributes to the total output signal, giving a characteristic distribution of signal sizes. Then, the pulses are grouped by the number of triggered microcells, or more precisely PE.

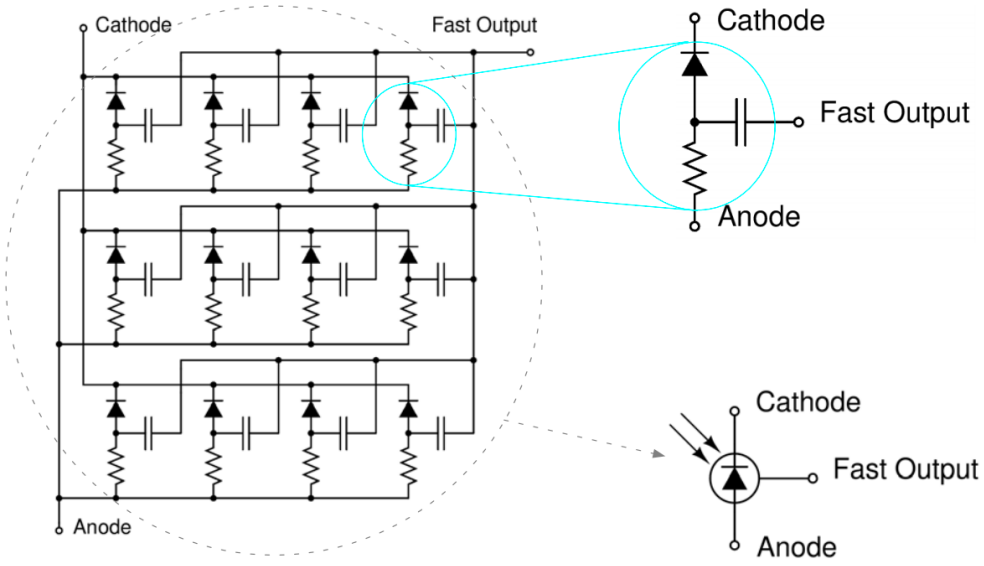

Figure 3.10: *Left*: Simplified circuit schematic of the ON Semiconductor SiPM showing only a 12 microcell example. Typically, SiPM sensors have thousands of microcells. *Top-right*: Circuit schematic of the ON Semiconductor SiPM microcell, showing details of the fast output. *Bottom-right*: ON Semiconductor SiPM component symbol. [ON-Semiconductor, 2021]

The arrival time of the light reaching the SiPM can be read off at the pulse as well. It is associated with the rising edge of the pulse. [Audehm, 2020]

3.2.4. Data acquisition system

The Data Acquisition system (DAQ) of the HAWC's Eye telescope is formed by a couple of Pre-Amplifier board (FPA), Trigger Unit board (FTU), and Analog-to-Digital converter board (FAD), which are lent by the FACT Collaboration [Anderhub et al., 2013], so this system is tested and functional. The DAQ needs a couple of these boards because each system is capable of processing the data of 36 SiPMs pixels, so it was easily modified to process the HAWC's Eye's 64 SiPM pixel camera. These 6 boars are plugged into a backplane which distributes the voltage and is responsible for the signal exchange between the boards as well. Figure 3.11 shows the previously described DAQ system. [Audehm, 2020]
Figure 3.12 shows the DAQ trace. First, to get a signal from the SiPMs, they must be powered by the Power Supply Unit (PSU). The PSU keeps the SIPM's gain constant by modifying the bias voltage of each one depending on its temperature. The PSU that is installed in the HAWC's Eye telescopes is the second version of the PSU [Schumacher et al., 2016, Schumacher, 2019]. Figure 3.11 (left) shows an example of a PSU with eight channels connected. An external voltage below 100

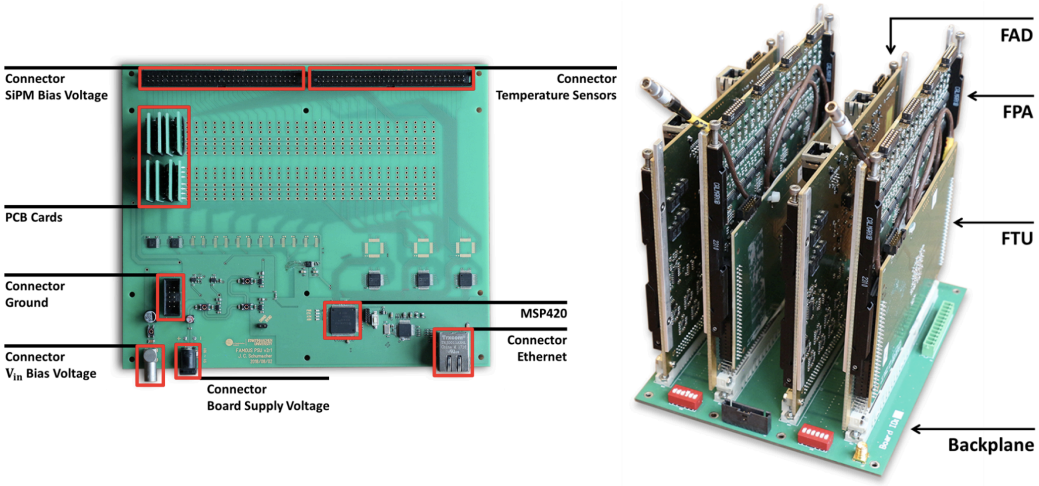

Figure 3.11: *Left*: Power supply unit of the DAQ. The image shows an example of eight channels plugged. *Right*: HAWC's Eye DAQ is composed of two sets of FACT DAQ boards, all these plugged in a backplane. [Audehm, 2020]

V, V_{in}, is connected to the PSU and it is adjusted for each one of the 64 SiPMs in the camera. Because of this, each SiPM is controlled by a Printed Circuit Board (PCB) card which has a linear regulator circuit, that is plugged in the PSU. The voltage that is fed into each PCB must be in the range of 0 V and V_{in}, and the current value used is 35 V. Also the current and voltage of each SiPM must be continuously measured, and the PCB cards make this possible too. Another important function of the PSU is that it can make an automatic modification on the bias voltage depending on the SiPM temperature, using an integrated MSP430 microcontroller [TexasInstruments, 2021]. The adjustment depends on the feedback of 64 temperature sensors which are placed in the locations of the pixels, and they are connected to the PSU, so the temperature dependence of the breakdown voltage, and hence of the gain, can be effectively compensated. All the measurements (voltage, current, and temperature) are digitized by the MSP430's 12 bit ADC and transferred to the operation PC via Ethernet. The Ethernet connection is used for communication as well. [Schumacher et al., 2016, Audehm, 2020, Schumacher, 2019]

The total 64 pixels are divided into two sets, which will be analyzed by each set of FACT DAQ (1 FPA + 1 FTU + 1 FAD). When a pulse signal is generated by the pixels (channels), this is fed into the FPA board; each FPA board is fed with 32 channels, which are divided into 4 subsets of 9 channels each which are connected to a Domino Ring Sampling chip (DRS4) what here will be called as *patch*. The 4 patches are connected to the FPA board and fed with the pulses and, arriving at the board, single-channel signals are amplified. Then, with the signals amplified, they

are divided into two sets to be analyzed by two different processing chains. The first half of the pulses are processed by the FPA, which stores the signals in the ring buffers composed of 1024 capacitors. Each ring is overwritten continuously with a sampling rate of 2 GHz until the trigger decision is made. After the trigger decision, the signals are fed into the FAD which digitizes them.

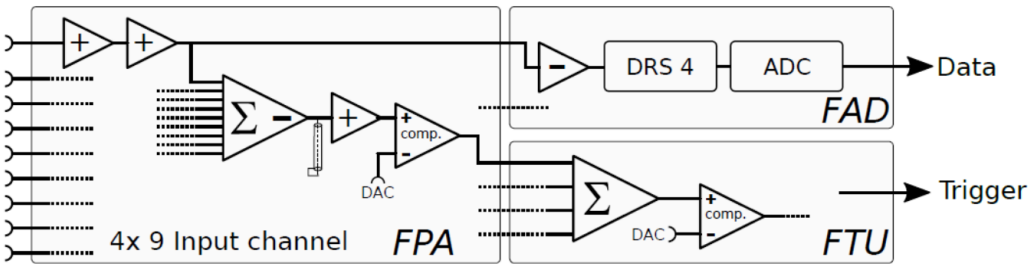

Figure 3.12: Schematics of the trace of the output signal from the SiPM to digitalization and trigger decision for one pixel at one patch of one board. All the other signals are equivalently treated. [Schaufel, 2017]

Meanwhile, the other half of the signals are used to make the trigger decision. From this half of pulses, all the signals in one patch are summed and the sum is inverted. Then, the sum is compared with an adjustable threshold on the FPA to create a "patch trigger", this process is for each patch individually. All four patch thresholds of one FPA then are fed into the FTU board to make the final trigger decision. The trigger can be adjusted to indicate if one, two, three, or the four patch triggers have to appear in coincidence to create a "board trigger". This decision process is an N-out-of-4 logic. Finally, a board trigger can initialize the readout procedure on the FADs.
For a proper trigger, the image of an EAS detected by the camera must be contained in one patch of pixels, or at least in most of them. Because of these, the pixel patches are arranged in a symmetric way[3]. Figure 3.13 shows the coaxial cables (semtec MH081-MH1RP [SAMTEC, 2021]) used to feed each channel pulse into the FAD, the patches, the DAQ boards, and the aluminum skeleton as well, all in a disassembled version of the telescope's DAQ.

Only one board trigger is needed to trigger the whole telescope. When the readout is in process, a busy signal must be sent to the FAD to prevent the acceptance of additional information triggers until the current readout process is finished [Bretz et al., 2018]. This busy signal is generated by the Trigger Master board (miniFTM). Also, the miniFTM is the board responsible for synchronizing the

[3]The pixel patches layout used in this work is shown in A

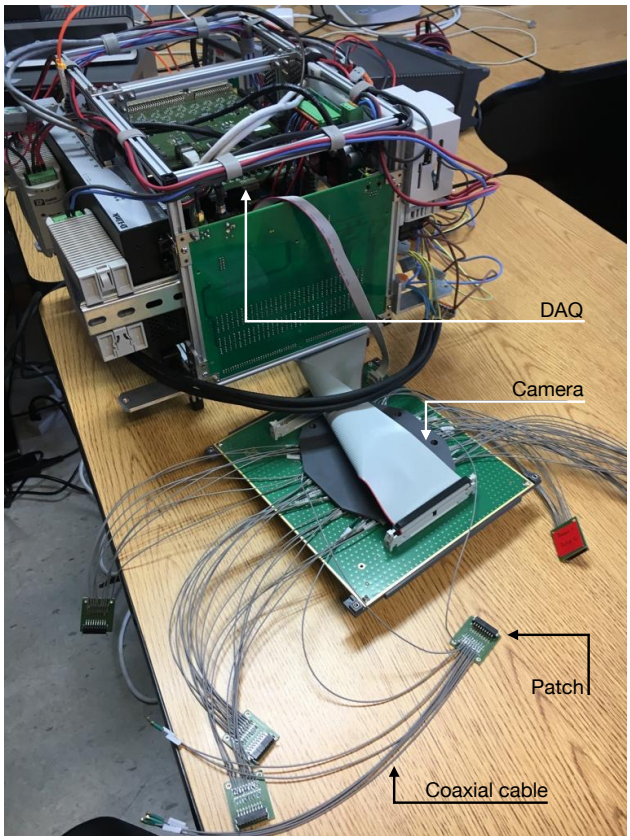

Figure 3.13: Channel coaxial cables, nine-channel patches, DAQ boards, and aluminum skeleton in which all the telescope DAQ is mounted.

complete system of 6 boards of the DAQ and perform the trigger distribution between the FTUs and the FADs.
The complete DAQ system is mounted in an aluminum skeleton box. Then, to protect the system, it is saved inside a water-tight fiberglass reinforced polyester box, which is screwed to the bottom part of the telescope's barrel. Figure 3.14 shows the DAQ inside the protective box. The camera is attached to the same structure so that DAQ and camera can be easily separated from the telescope body for transportation or maintenance.

Figure 3.15 is a simplified schematic of the instrumentation inside the DAQ box. The box contains the DAQ and some more electronics needed for proper control of the telescope. This includes AC/DC converters that provide 5 V DC operating voltage for the electronics, and the 35 V to bias the SiPMs as well. AC input voltages of 110 V/60 Hz and 230 V/50 Hz are accepted. Additionally, a BeagleBone single-board controller equipped with a BeagleBone Load Cape [BeagleBone, 2021b, BeagleBone, 2021a] is used together with several relays to power

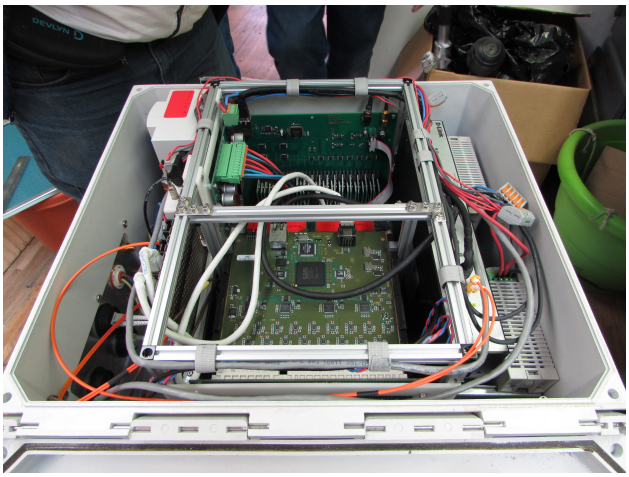

Figure 3.14: DAQ mounted in the aluminum skeleton, all inside a water-tight fiberglass reinforced polyester box.

cycle the FACT boards and control the power input of the SiPM PSU. To enable a non-conductive trigger output from the telescope, a fiber optics trigger transceiver system is used to convert the telescope trigger [Schaufel, 2017]. Finally, a gigabit switch is available for internal and external communication. The power input, communication signal, and trigger output are routed through the closed box with the help of an aluminum plate with multiple connectors[4].

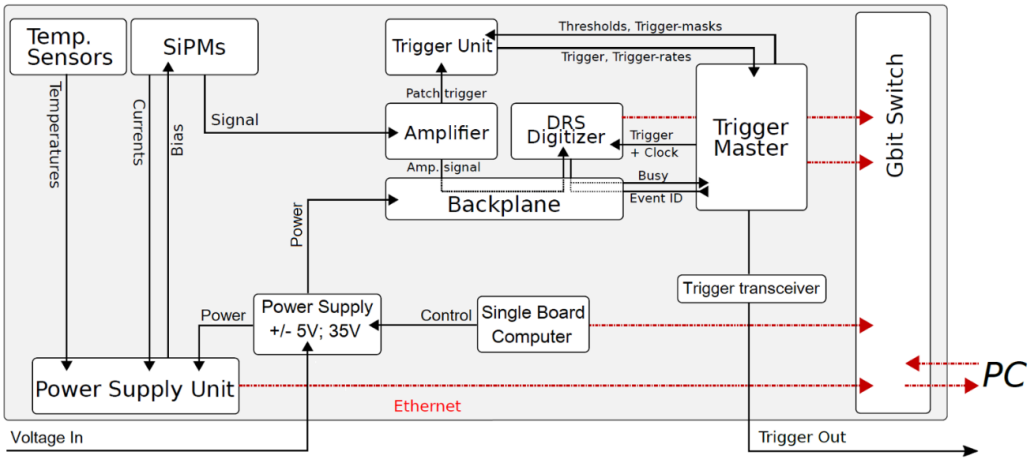

Figure 3.15: Schematics of the entire electronics system enclosed in the DAQ box. Based on [Bretz et al., 2018].

[4]The plate used on the telescopes, and the assignment of the used connectors can be found in A

3.2.5. Telescope monitoring and operation

Because the HAWC's Eye DAQ is composed of the FACT boards and some more, this is operated using the software developed for the FACT telescope, called *FACT++* [Anderhub et al., 2013]. Some boards from the HAWC's Eye DAQ were not used in the FACT telescope, as the PSU, the miniFTM, and the single-board computer, so the framework was extended for this. Each component has its own console-based program that runs in the operating computer of the telescope. Each program shows the status of the subsystems every single moment, and they answer to manual command-line inputs or commands distributed by a JavaScript interpreter. Then, for the communication between individual framework subprograms, the Distributed Information Management (DIM) system is used [CERN, 2021]. An overview of the FACT++ framework used for the HAWC's Eye telescope is shown in Figure 3.16. Text User Interface (TUI) is also shown in the same Figure, which is used for remote monitoring of important system parameters, as pixel voltages, current, temperature, or system trigger. [Audehm, 2020]
To simplify the telescope operation during data taking, scripts are available for different tasks using JavaScript, such as recording the calibration data for the DRS4 chips, or the start of the data taking process. Runs created during data taking contains 5 min of information. Also, there is an option for the software to take over the trigger threshold adjustment considering the monitored pixel currents [Bretz et al., 2018], which ensures a data acquisition with a constant noise trigger rate under changing background conditions [Audehm, 2020].

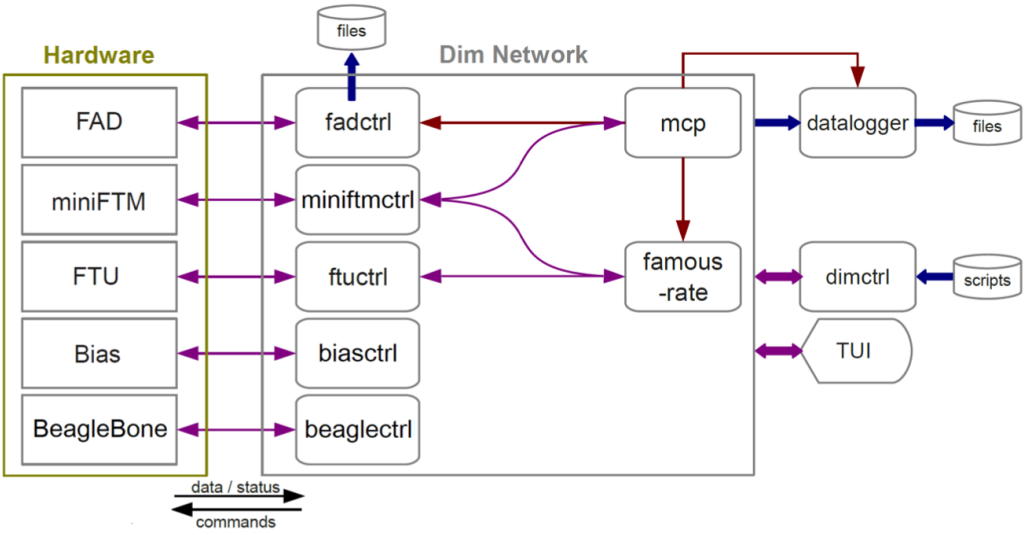

Figure 3.16: Flux diagram with the telescope system with its hardware and software components [Audehm, 2020].

4

HYBRID OBSERVATION CAMPAIGNS

Four hybrid observation campaigns, with HAWC's Eye and the HAWC observatory, have been made. The first one was in 2017, in which just one HAWC's Eye telescope prototype was used. Then, the second and third observation campaigns were made in 2019, where two improved HAWC's Eye telescopes were placed in the HAWC's site and the hybrid observation was done. Finally, in 2020 a third campaign was made.
The following chapter describes the observation campaigns performed with the HAWC's Eye telescopes, specially the last one which is the one analyzed in this work.

4.1. 1st Observation campaign: Jul/Aug 2017

The first observation campaign was performed by Merlin Schaufel, in collaboration with Rubén Alfaro and Arturo Iriarte[1], for three nights between July and August of 2017.
During this campaign, one prototype of the HAWC's Eye telescope was used. It was located almost in the middle of the HAWC array, as shown in Figure 4.1(a), because of its centrality, and the given accessibility of infrastructure needed to operate the telescope properly, as shown in Figure 4.1(b). The exact position of the telescope, due to the HAWC coordinate system, was $x = (59.4 \pm 0.5)$ m and $y = (219.0 \pm 0.5)$ m.

Before starting the data-taking procedure, the orientation and tilt of the telescope had to be set. The protective box of the camera was used to establish the reference

[1] A picture of the crew from the 1st observation campaign can be found in the Appendix A.

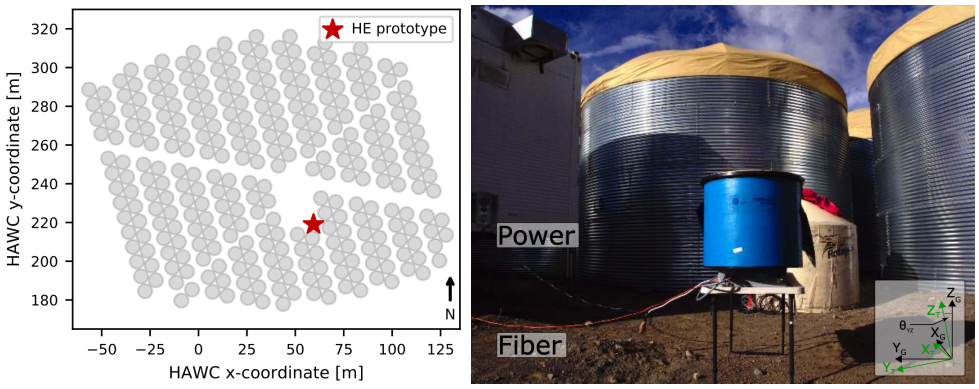

(a) (b)

Figure 4.1: *(a)* HAWC's layout where the WCD are represented with gray circles, and the position of the HAWC's Eye telescope during the observation campaign of 2017, pointed with a red star [Audehm, 2020]. *(b)* First setup of the IACT HAWC's Eye at the HAWC's site [Schaufel, 2017].

for all the needed measurements. So then, the x-axis of the telescope coordinate system was pointing to $(46 \pm 1)°$NE, whereas the z-axis was tilted away from the ground array's zenith.

The telescope was operated and monitored via Ethernet from its own computer, using the FACT++ software described before (see section 3.2.5) and it was connected to a 110 V power supply. Also, considering the synchronization of the data from both experiments, the trigger output from the HAWC's Eye electronics was connected to the HAWC DAQ, in particular storing the trigger signal in a PMT channel of the HAWC data stream; all this by the fiber optics transceiver developed in [Schaufel, 2017] and an SC-type optical fiber. The chosen channel was the 31, which was blacklisted for HAWC so it cannot affect the trigger decision or the reconstruction of events.

This observation campaign lasted three nights, but only data taken during the 27th to 28th of July night was considered for analysis. The reason for this was the quality of the weather during the observation nights; in particular, the chosen night had excellent weather conditions including a clear sky and a little bit of moonlight due to the moon that was in the first quarter phase, which is a noise signal for the telescope.

For a more detailed and complete description of the analysis made during this campaign, see [Schaufel, 2017].

4.2. 2nd Observation campaign: Sept/Oct 2019

Almost two years later since the first observation campaign, it was possible to do a new one with some improvements in the telescope design. The improvements are the implementation of the SenseL SiPMs pixels on the camera, and the Winston cone hex-to-sqare light collectors on each pixel, but the principal improvement from the first campaign is the implementation of two HAWC's Eye telescopes at the HAWC's site. This campaign was done in the night between the 2nd and 3rd of October of 2019, and it was performed at the site by Jan Audehm, in collaboration with Rubén Alfaro, Jesús Martínez and Yunior Pérez[2], and remotely by Thomas Bretz.

First of all, it is important to mention that the two cameras from the telescopes are not identical, due to a problem during its transportation from Germany to Mexico. Four light collectors were ripped off from one camera, and one of those took the SiPM out from the camera too[3]. In other words, there is one totally dead pixel and three more that have less amplitude in their signal compared to the others, so those four pixels are not used during the data analysis. They cannot be glued back to the camera because the light-collector array is so tight that others can be affected or damaged in the process. This camera is the one placed in HAWC's Eye 02.

In the first campaign, the telescope was not physically covered against any external condition, so for this new campaign two shields were constructed, one for each telescope. The shields are made of an aluminum skeleton and covered all around with a thick tarpaulin.

Two new locations were chosen to place the telescopes into the HAWC array. So, to have the exact new positions of the telescopes, the distance between these locations and the four nearest HAWC's WCD was measured with a laser distance-measurement tool, and knowing the radius and exact position of the center of each WCD in the HAWC layout, it is possible to compute the position of the telescopes in the HAWC's coordinate system. Table 4.1 indicates the distances of the four nearest WCD to each telescope, and its x-y coordinates in the HAWC's coordinate system[4]. Figure 4.2(a) and 4.2(b) shows the exact position of each telescope using the values shown in Table 4.1, and their computed coordinates are shown in Table 4.2.

To be congruent with the HAWC coordinate system, both telescopes had to be aligned, so the x-axis of the telescopes pointed to the East of HAWC, and the y-axis pointed to the North. Then, using a water level, both telescopes were tilted

[2] A picture of the crew from the 2nd observation campaign at the site can be found in the Appendix A.

[3] An image of the HAWC's Eye 02 camera with the missing pixels can be found in Appendix A

[4] A full labeled layout of HAWC can be found in the Appendix A

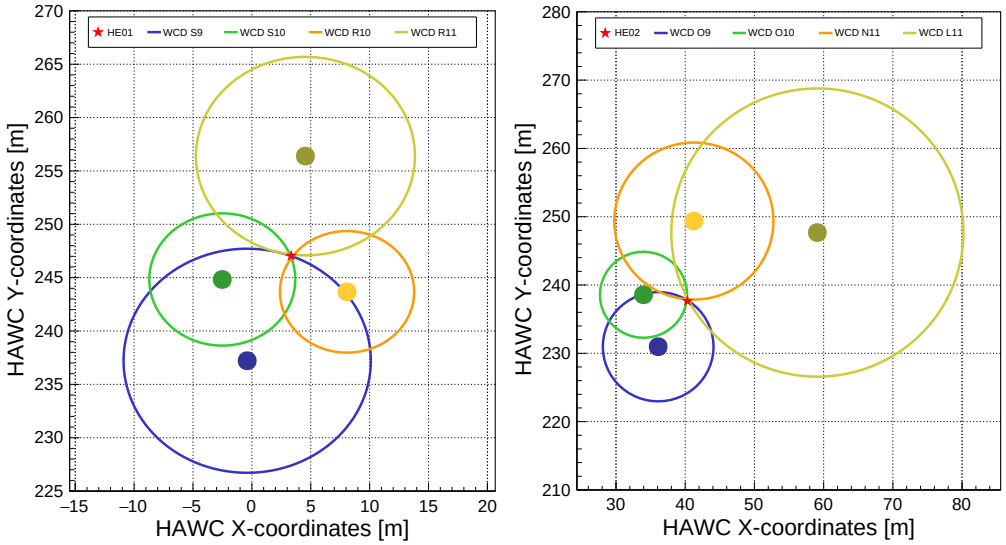

(a) (b)

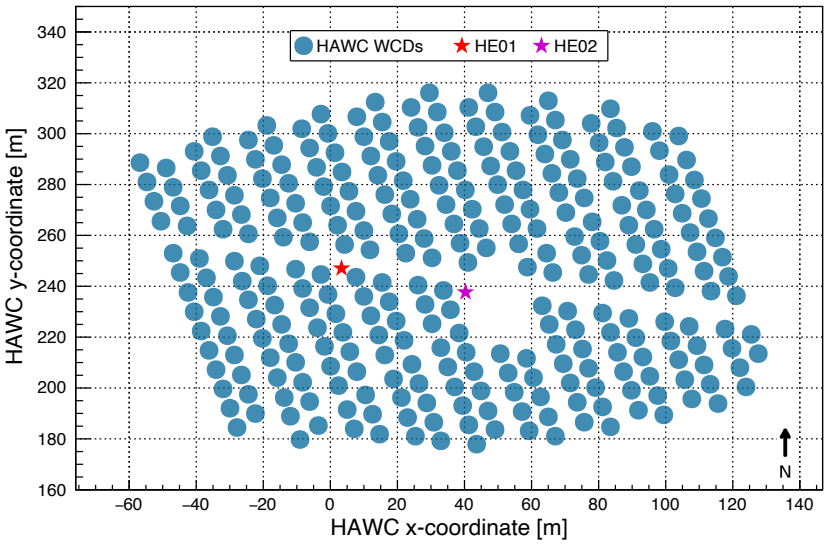

(c)

Figure 4.2: *(a)* Computed position for HE01 using the distance to the nearest WCD. *(b)* Computed position for HE02 using the distance to the nearest WCD. *(c)* HAWC's Eye 01 and HAWC's Eye 02 positions in the HAWC's array represented with orange and magenta stars respectivelly. The blue circles represent the HAWC's WCDs.

HAWC's Eye 01				HAWC's Eye 02			
WCD ID	**x [m]**	**y [m]**	**Distance [m]**	**WCD ID**	**x [m]**	**y [m]**	**Distance [m]**
S9	-0.398	237.214	6.572	L11	59.094	247.680	17.984
R11	4.546	256.389	6.085	N11	41.250	249.364	8.054
R10	8.082	243.671	2.432	O9	36.093	230.965	4.184
S10	-2.513	244.829	2.170	O10	33.976	238.572	2.382

Table 4.1: Distances between each HAWC's Eye telescope and their four closest WCD, with its coordinates respectively. The coordinates are taken from the layout file included in the AERIE software.

	HAWC's Eye 01	**HAWC's Eye 02**
x [m]	3.33	247.05
y [m]	40.31	237.66

Table 4.2: HAWC's Eye telescopes x-y coordinates in the HAWC's coordinate system computed using the distances to the nearest WCDs.

until they were leveled in every direction. Finally, similar to the first campaign, each telescope was powered with 100 V and connected to its own PC. Both telescope triggers were connected to the HAWC DAQ, each one to a different PMT that was previously blacklisted so they cannot be into the HAWC's trigger decision or reconstruction, all this using the same fiber optics transceiver design from the previous campaign.

During the observation campaign, several issues came up: first only the HAWC's Eye 01 telescope trigger was able to connect to the HAWC DAQ (channel 31), and the other trigger can not. Then, a high-frequency noise on the trigger signal appeared which was originated by the telescope itself or by the trigger transceiver system.

Approximately 30 minutes after starting the data acquisition, the lens became frozen (Figure 4.3), which affects the recorded data.

About one and a half hours of data were recorded, which was analyzed despite the frozen lens. With this data, analysis on the arrival direction of the air-shower particles was done.

The telescopes were stored in the *Verification and Assessment Measuring of Observatory Subsystem (VAMOS)* trailer, located up in the HAWC's site. Storing the telescopes on-site enables the posibility to easily plan future observation campaigns, since it is no longer necessary to transport the telescopes from the *Universidad Nacional Autónoma de México (UNAM)* laboratories to the HAWC site (which is a journey of approximately 5 hours), and the possible damage of the telescopes because of the transportation is avoided.

For a deeper explanation of this observation campaign and its results, see [Audehm, 2020].

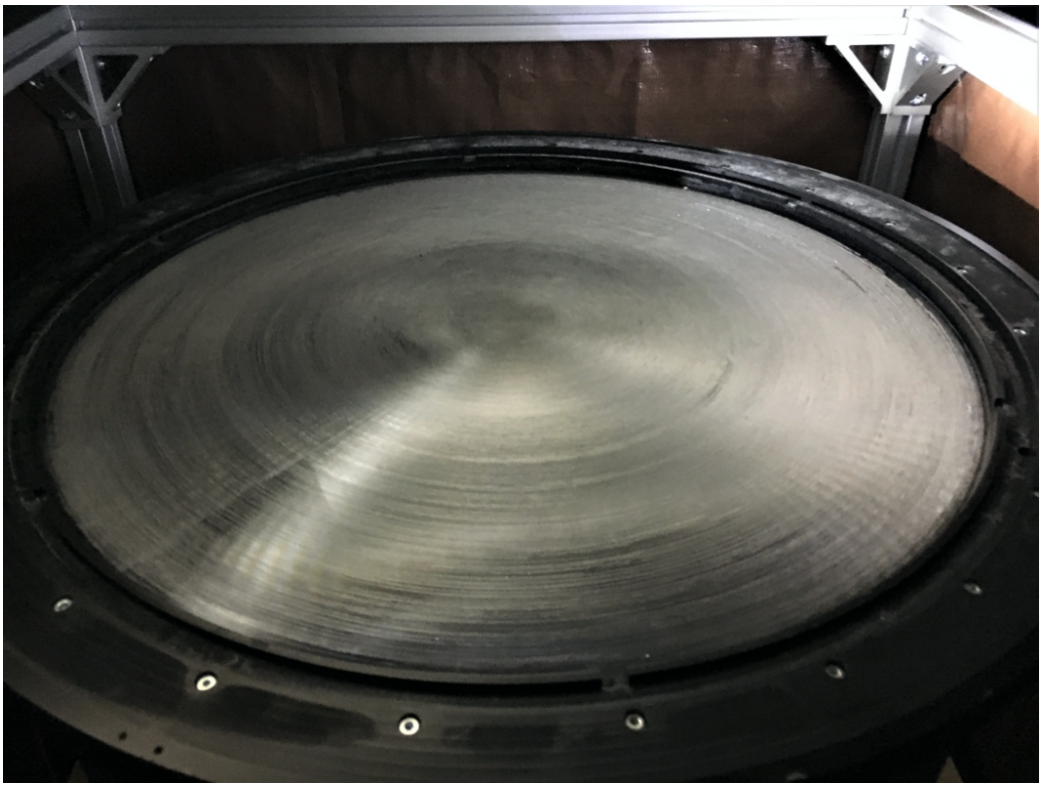

Figure 4.3: Telescopes frozen lens during the 2nd observation campaign. Image by Jan Audehm.

4.3. 3rd Observation campaign: Dec 2019

In 2019 another observation campaign happened, a few months after than the last one. This third campaign occurred from the 18th to the 20th of December of 2019. It was performed at the site by José Serna in collaboration with Rubén Alfaro and Arturo Iriarte, and remotely by Thomas Bretz and Jan Audehm.
For this campaign, the same setup characteristics used in the previous campaign were followed: the telescopes were located at the same positions (Figure 4.2(c)), and they were correctly orientated and leveled as before.
This time, the weather conditions were optimal for the observation, but the electronic noise that appeared during the 2nd observation campaign, appeared again delaying the start of the observation for a few hours. Besides that issue, no other problem appeared during the process. Furthermore, now both telescope trigger signals were able to connect to the HAWC DAQ; HAWC's Eye 01 and HAWC's Eye 02 were connected to channels 23 and 22 respectively and, as always, these channels were blacklisted so they will not be used for the trigger decision or event reconstructions.

During this observation campaign, about five hours of data were recorded. This information was analyzed, which led to an optimization in the synchronization of hybrid events and the first estimation of the cosmic ray spectrum with this instrument as well [Rehbein, 2021].
For a deeper explanation of this observation campaign and its results, see [Do, 2021].

4.4. 4th Observation campaign: Nov 2020

From 11th to 14th of November of 2020, the 4th observation campaign was performed. This campaign was carried out despite the difficulties caused by the COVID-19 pandemic. Five observation campaigns were planned from November 2020 to March 2021, during the Crab Nebula transit through the HAWC's FoV, but due to the pandemic, just the November campaign was possible.
As in the last campaigns, HAWC's Eye 01 (HE01) and HAWC's Eye 02 (HE02) were installed in the HAWC's site in the same positions used on previous observation campaigns (Figure 4.2(c)), and the distances with the nearest WCD, shown on Table 4.1 were corroborated.
The first day of the campaign, November 11th was used to check the proper functioning of the telescopes after a long period of inactivity. The telescopes DAQ were tested and the remote connection as well. Both telescope triggers were connected to the HAWC DAQ; at first both telescopes were planned to be connected to different HAWC channels (PMTs) as in previous campaings, but when it was done an electronic noise appeared and it disturbed the measurenment. Then the HE01 and HE02 trigger signals were connected to a same channel, the HAWC PMT E14C[5], which is associated with channel number 23.
During the next two nights, November 12th and 13th, the observation was performed. Both telescopes were controlled remotelly (via Ethernet) using the FACT++ framework in their own PCs located at the Counting House[6]. First, each night a rate scan was performed for both telescopes so a correct threshold could be used[7]. The threshold was selected after the rate scan for each telescope, and then it was adapted automatically by the telescope depending on the SiPMs current; the threshold value selected was in the range of 400 and 550 DAC counts both nights.

[5]The PMT E14C is the central PMT inside the WCD E14. For a detailed location of the WCD, the HAWC layout can be found in Appendix A.

[6]The Counting House is the main laboratory at the HAWC site where all the performance of HAWC is monitored, and the HAWC DAQ is located in.

[7]The rate scans of HE01 and HE02 for both nights of observation can be found in Appendix A.

Then, data taking started at 6:20 UTC (00:20 CST[8]) and 4:00 UTC (22:00 CST) on each night respectivelly, while the Crab Nebula was on top of HAWC. During data taking, both telescopes stopped the process because of different issues with the DAQ boards, but everything was solved and the process was restarted successfully again. Data taking finished at 11:50 UTC (5:50 CST) and 11:50 UTC (5:50 CST) respectivelly, due to the sunrise, which represents about 5:30 hours of observation during the first night and 7:50 hours of observation during the second one. The weather conditions during both nights were excellent: a starry night without clouds, rain, snow, or moonlight, until the sunrise. The lens did not get frozen, which represents a good concentration of the light to the camera. After this, both telescopes shields were closed to protect the telescopes from daylight.
In summary, the weather conditions were excellent both nights, which represents a good collection of data. Also, the data recorded represents about 13:20 hours of observation during two nights of the Crab Nebula transit above HAWC.

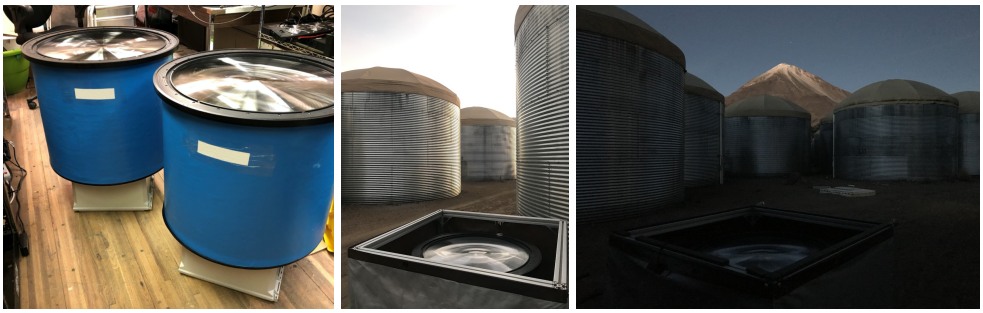

(a) (b) (c)

Figure 4.4: *(a)* HE01 and HE02 telescopes inside the VAMOS trailer before been placed inside their weather shields. *(b)* HE01 already located at its observation position inside its weather shield, before sunset. *(b)* HE02 already installed inside its weather shield and ready for observation, during sunset with the surrounded by the WCD and the Pico de Orizaba in the background.

[8]CST is the standard Mexico timezone (UTC-6). Do not confuse it with the summertime DST (UTC-5).

5

HYBRID DATA ANALYSIS PROCESS

To correctly analyze hybrid data recorded from both experiments, the information must be analyzed separately by each experiment's analysis chain and then make the synchronization of the events. In this chapter the detectors analysis software will be explained, focusing principally on the HAWC's Eye data analysis chain, and a brief explanation of HAWC's analysis.

5.1. HAWC's Analysis Software: AERIE

The HAWC observatory must save the information from a huge amount of EASs that reach the detector at every moment, so the data has to be stored in a file format that supports the amount of information and is easy to manage. For this reason, HAWC data is stored in an eXplicitly Compacted Data Format (XCDF) file [XCDF, 2021]. Raw data detected by HAWC is stored in an XCDF file, and to perform the EAS extended reconstruction analysis, the Analysis and Event Reconstruction Integrated Environment (AERIE) offline reconstructor tool was used [Abeysekara et al., 2018], which is the HAWC's analysis software. The output is provided in XCDF format and it has the full information about the primary particle. Finally, the XCDF file can be converted to ROOT file format [Brun and Rademakers, 1997] with the XCDF-ROOT tool included in AERIE. Figure 5.1 shows a flow chart with the steps followed during the analysis of HAWC.

5.2. HAWC's Eye Analysis Software: MARS

While HAWC saves its data in an XCDF file, the HAWC's Eye telescopes use the Flexible Image Transport System (FITS) [Wells and Greisen, 1979, Pence et al.,

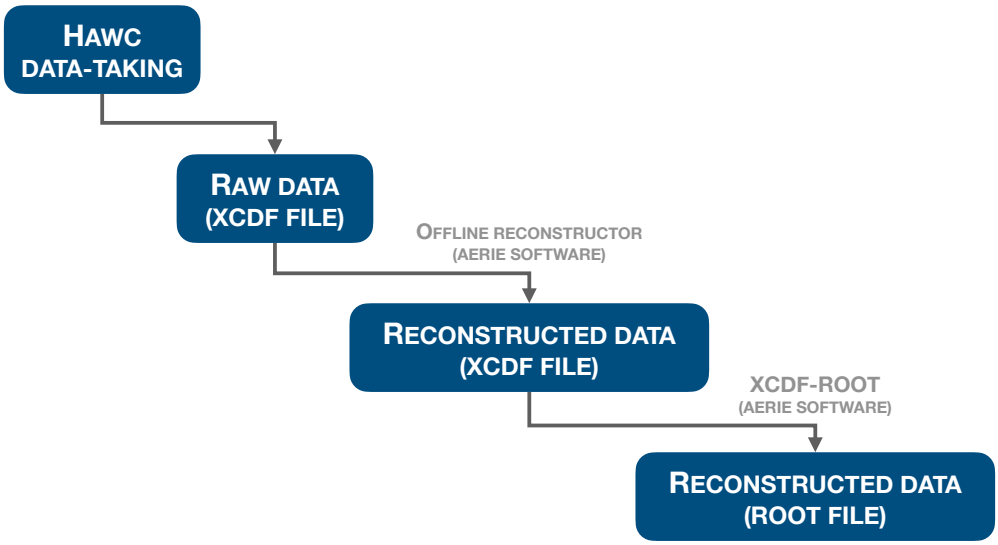

Figure 5.1: Flow chart of the steps followed for the HAWC analysis steps, starting with the data-taking and finishing with the data reconstruction in ROOT format.

2010] file format to store the data from the EAS's that triggered the telescope's DAQ because it is a useful format to store astrophysical data. The main advantage of this file format is that the metadata is stored in human-readable ASCII format. One example is that FITS files also supports tabular data with named columns and multidimensional rows. Both binary and ASCII table formats have been specified. The data in each column of the table can be in a different format from the others. Together with the ability to string multiple header/data blocks together, this allows FITS files to represent entire relational databases. Also, FITS files are supported in most of programming languages used for cientific work which allows that each person can write their own code to read and use the data recorded in a same FITS file.
Therefore, basically, four steps must be followed to do a proper data analysis: data calibration, signal extraction, image cleaning, and image parametrization. These steps are done using scripts contained in the Modular Analysis and Reconstruction Software (MARS) ROOT-environment [Bretz, 2003]. Such scripts were developed in [Schaufel, 2017].

5.2.1. Calibration

When the Cherenkov light produced by an EAS reaches the telescope, it is focused on the camera, where the information is recorded as signal pulses produced by the SiPMs pixels, all this using the DRS4 chip previously described in 3.2.4.

The DRS4 chip is made up of 1024 capacitors, where the signal is recorded with a sampling rate of 2 GHz in a dynamical voltage range of 2 V. Then, each signal, that is an analog signal, is digitized. Now, each capacitor of the DRS4 has a characteristic gain and offset, so each one of these has to be calibrated individually. If these pulses are not calibrated, the signal will be hidden within the background noise, especially the signals with small amplitudes. Therefore, initial calibrations are done for each SiPM to correctly know their gain and offsets, and a proper calibration to the signals can be applied [Kraehenbuehl, 2011]. An easy way to differentiate a calibrated signal from an uncalibrated one is to look after the baseline value and the pulse shape: in an uncalibrated signal the baseline is far away from 0 mV and the shape of the pulse usually is not soft and is wider, while in a calibrated signal, the baseline is at 0 mV (or very close) and its shape is softer, as shown in Figure 5.2.

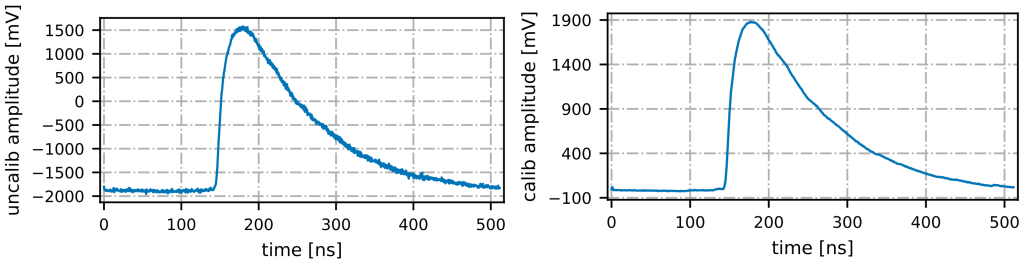

(a) (b)

Figure 5.2: *(a)* Signal pulse before the calibration: the baseline is ~ -1900 mV, the pulse is wide and has tiny peaks along all the pulse fall. *(b)* Signal pulse after the calibration: the baseline is ~ 0 mV, it is thinner and softer than before. [Audehm, 2020]

5.2.2. Signal Extraction

The signals recorded by the telescope camera make a so-called *camera image*. Then, the necessary information to reconstruct the primary particle associated with the observed EAS is contained in it. So, to correctly know the camera image, the signal from each SiPM pixel recorded after the trigger produced by the EAS, must be extracted.

Each pulse contains 1024 samples of the signal, which are recorded every 0.5 ns. Thus, the SiPM pulse can be shifted inside the record window[1] by applying an internal delay to the trigger decision. This shift must be correctly chosen so that most of the pulse is inside the window, but leaving enough samples to estimate the baseline. The arrival time and amount of light that reached the telescopes are

[1] A record window is a fixed time lapse in which the triggered signal samples are recorded.

fundamental parameters for the event reconstruction, and these parameters can be estimated by the maximal amplitude of the pulse and the position of its rising edge, so then, this information for all the pixels is used on the analysis.
Figure 5.3 shows the different pulse regions considered for the analysis: the first 5 ns of the pulse are excluded from the analysis due to fluctuations (red), then the 5 ns to 112.5 ns region is the one used to compute the baseline (yellow). Next, the region from 115 ns to 250 ns (blue) is used to locate the maximum amplitude of the signal, which is completely related to the detection of the EAS by the telescope. Then the leading edge must be located, and it is defined as the moment when the rising pulse crosses 70 % of the maximum amplitude; the leading edge is expected to be located in the range of 117.5 ns to 162.5 ns (fading green). Finally, the last 5 ns of the pulse are also excluded from the analysis because of fluctuations (red). For cases with a low signal-to-noise ratio, the maximum amplitude of the pulse might be too close to the record window edges, so the leading edge can not be found. These special cases are analyzed more deeply.

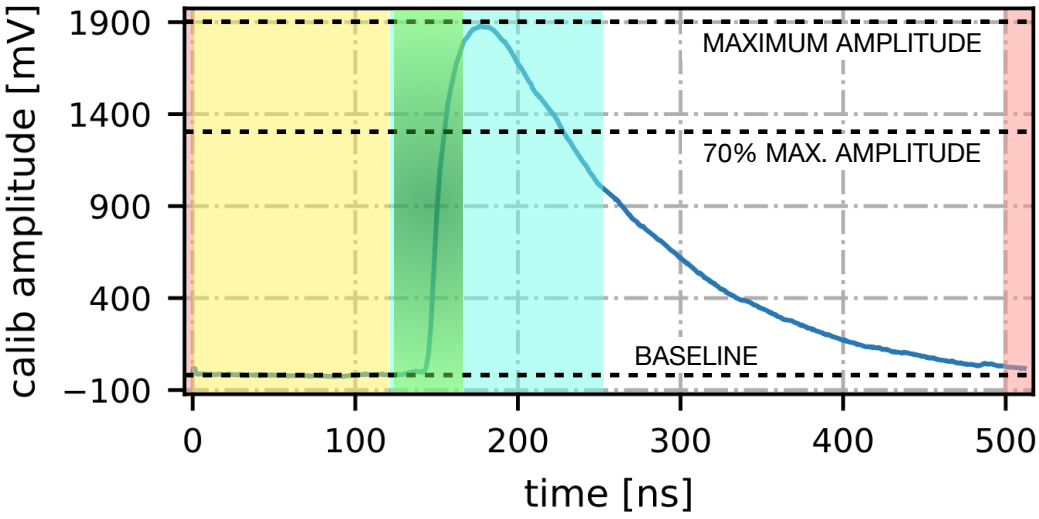

Figure 5.3: Pulse parts considered during the signal extraction. The red regions located at the edges are the parts excluded from the analysis, the yellow region is the pulse section used to compute the baseline, the fading green region is the one where the arrival time information is expected to be, and the blue region is the pulse section where the pulse maximum is expected to be.

Finally, the light pulses detected with the camera must be cleaned to correctly reconstruct the EAS detected.

5.2.3. Image Cleaning

The cleaning process follows two different steps: first, the signal preselection is performed, and then the image pixels cluster selection.

In what follows, both processes are described.

SiPM Signal Preselection

In this step, the SiPM pixels are analyzed and the clustering pixel signals are selected. To be selected, the signal from each SiPM has to pass through several filters, and the logic path followed for this is shown in Figure 5.4.
These filters include the condition that each independent pixel signal must have an amplitude > 45 mV, and also it must be, at least, 5 times bigger than the baseline. Other conditions are that the leading edge and the maximum position are inside the regions described in Section 5.2.2. Some pixels can have an amplitude > 2000 mV, which are considered as saturated, so for them, the maximum of the signal is given by the integral of the pulse trace. From all the preselected pixels, the one with the highest maximum amplitude (or trace integral) value is selected as the center of the cluster, and the rest are stored in a list of corrected preselected pixels.

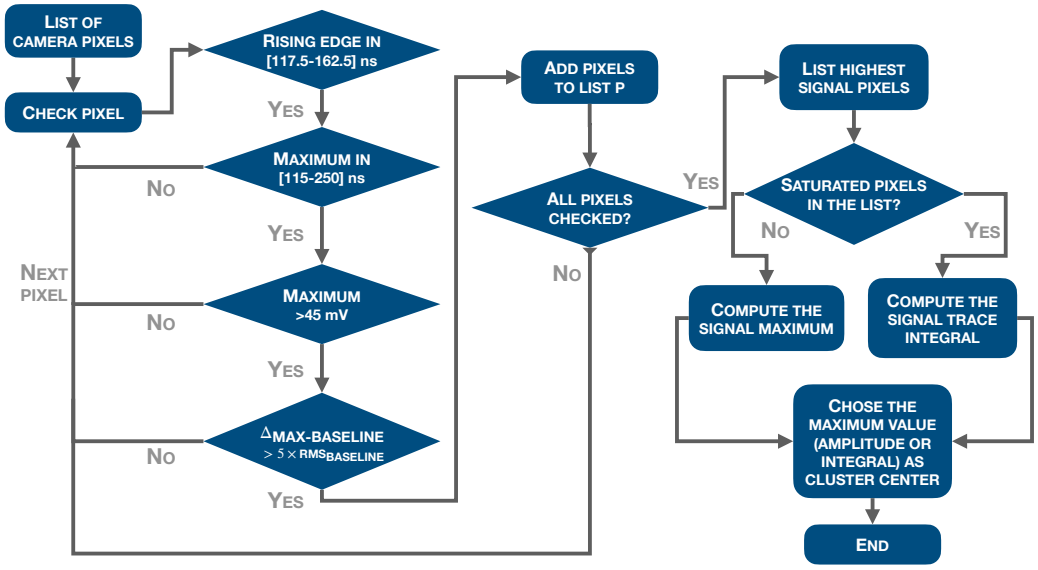

Figure 5.4: Flux diagram of the logic steps to preselect the SiPM signals from the camera. At the end, a list of filtered signals is created. Adapted from [Schaufel, 2017, Audehm, 2020].

Image Pixel Cluster Selection

After the preselection of the SiPMs, the next procedure is to analyze the signal clustering. For this, the SiPM selected as the center of the cluster in the preselection process is fixed as the center of the cluster and as the starting point. Then, all

the neighbor pixels of the center one are analyzed, and all those that have a signal arrival time > 5 ns concerning the signal arrival time of the center one are stored in a list of SiPMs that constitute the cleaned camera image. Then, the same process is repeated for the neighbors of the SiPM pixels added to the list previously. This method is repeated three times and all the SiPM pixels that pass through this filter, are stored in the list. Figure 5.5 shows the logic steps previously described.

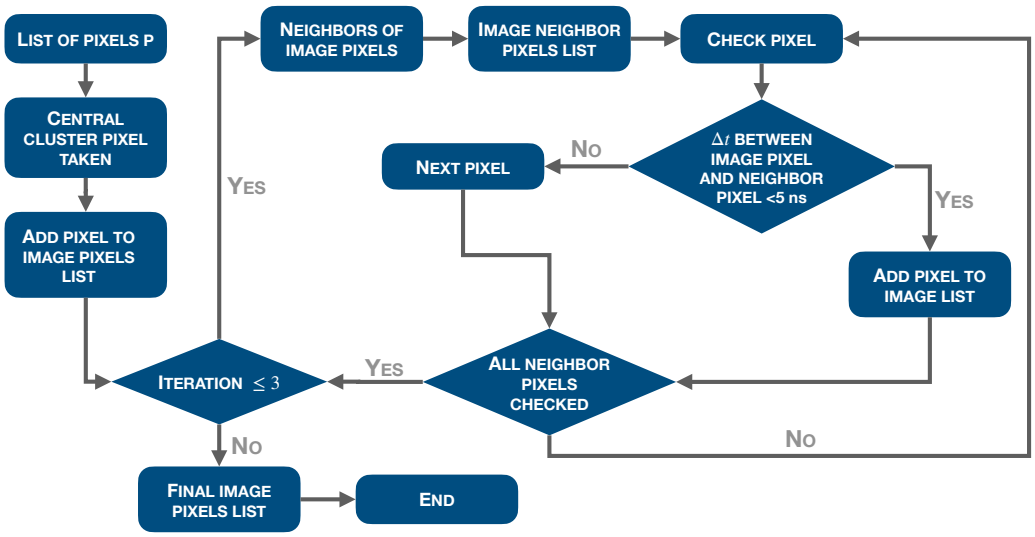

Figure 5.5: Flux diagram with the logic steps to select the SiPMs included in the cleaned camera image. Adapted from [Schaufel, 2017, Audehm, 2020].

This cleaning technique was empirically tested by analyzing different images and looking after the resulting camera image to be correctly cleaned.
Figure 5.6 shows an example of the cleaning process, showing the amplitude values and arrival time for each pixel, and the SiPM cluster obtained at the end of the method, which is the camera image.
After the cleaning process is correctly applied and the SiPM pixels which constitute the image camera are identified, now the image has to be parametrized.

5.2.4. Image Parametrization

The result of the cleaning process is a cleaned image that is associated with the detected EAS. So, to make a full reconstruction of the primary particle that created the detected EAS, the cleaned image must be characterized by parametrizing it. The parameters that characterize it are known as *Hillas parameters*, which are described below.

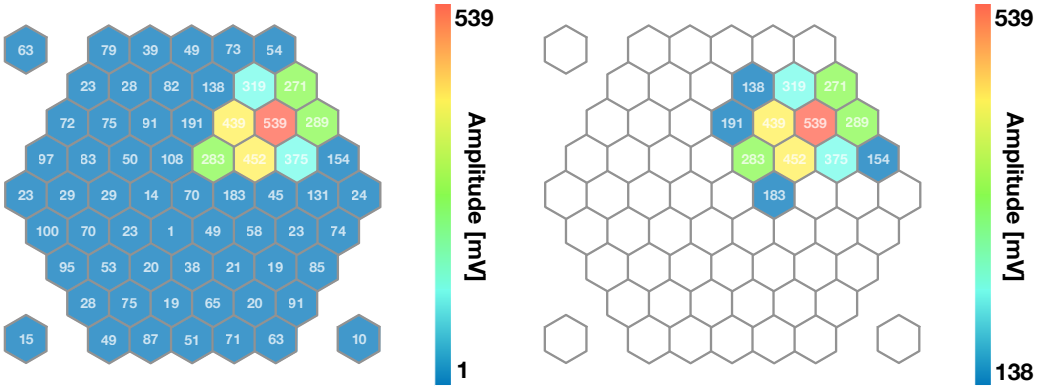

(a)

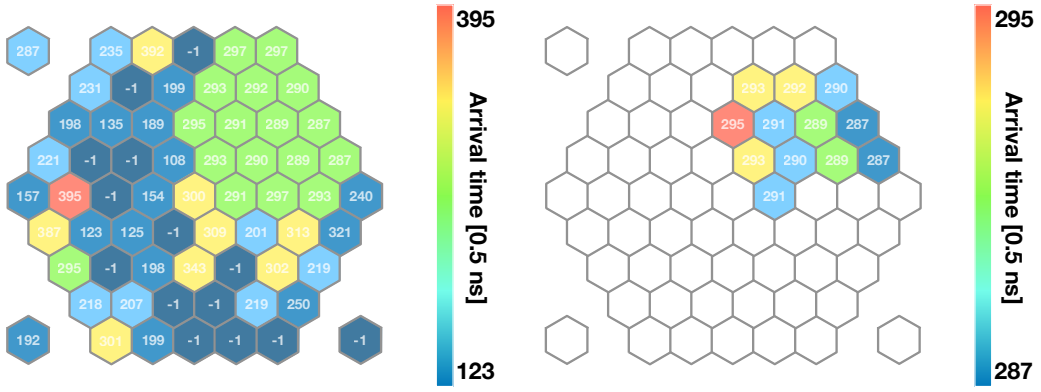

(b)

Figure 5.6: The hexagons in the display represent the camera pixels, and their color is associated with the color scales. *(a)* For each pixel of the camera, the amplitude value (in mV) is specified. The left side shows the recorded signal produced by the detected EAS before being cleaned, and the right side is the same detected event after the cleaning method has been applied. *(b)* Now, the values of each pixel represents the arriving time (in 0.5 ns). The negative values are for those pixels that the leading edge could not be estimated. The left side shows the arrival time for all the pixels in the camera, for the detected EAS. The right side shows the selected pixels after the cleaning, which are the same pixels selected in the signal cleaning.

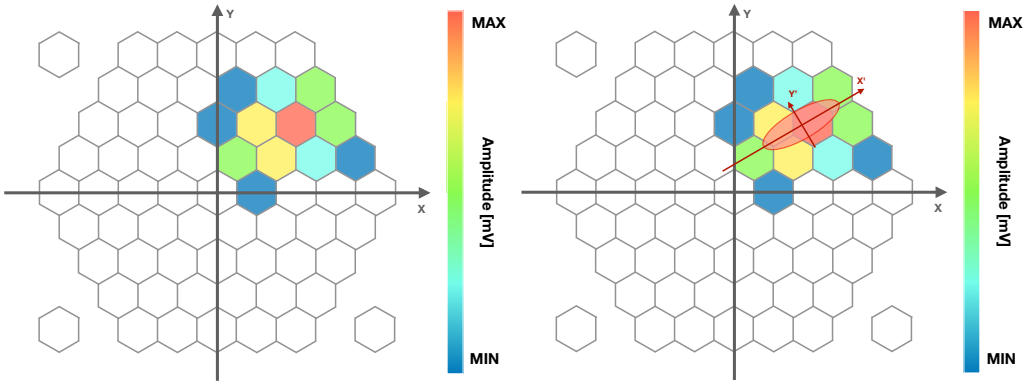

(a) (b)

Figure 5.7: *(a)* SiPM pixels selected after the cleaning process. The color scale shows the distribution of the amplitude values for the pixels. All pixels in white color are taken out of the analysis. *(b)* Parametrization of the SiPM pixel cluster is representated with an ellipse and computing it centroid and defining a new coordinate system (X', Y').

Hillas parameters

The Hillas parameters are values that describe geometrically the cleaned image associated with an EAS. The first to propose these parameters was Anthony Hillas in 1985 [Hillas, 1985]. For this process, the parametrization of the cleaned image is represented with an ellipse, and the geometrical parameters are obtained. Figure 5.8 shows a description of the Hillas parameters of the ellipse.

The main Hillas parameters are:

- **Centroid:** Center Of Gravity (COG) of the image with coordinates $(X_{\mathrm{COG}}, Y_{\mathrm{COG}})$. It is defined as the weighted mean of the N position vectors $\vec{v}_i$ of the cleaned image pixels. If s_i is the signal of the $i-$th pixel, then the center of gravity is given by:

$$\vec{v}_{\mathrm{COG}} = \langle \vec{v} \rangle = \frac{\sum_{i=1}^{N} \vec{v}_i \cdot s_i}{\sum_{i=1}^{N} s_i}, \tag{5.1}$$

  and it is the starting point to compute the rest of the parameters. Then, a covariance matrix which describes the signals can be estimated, by:

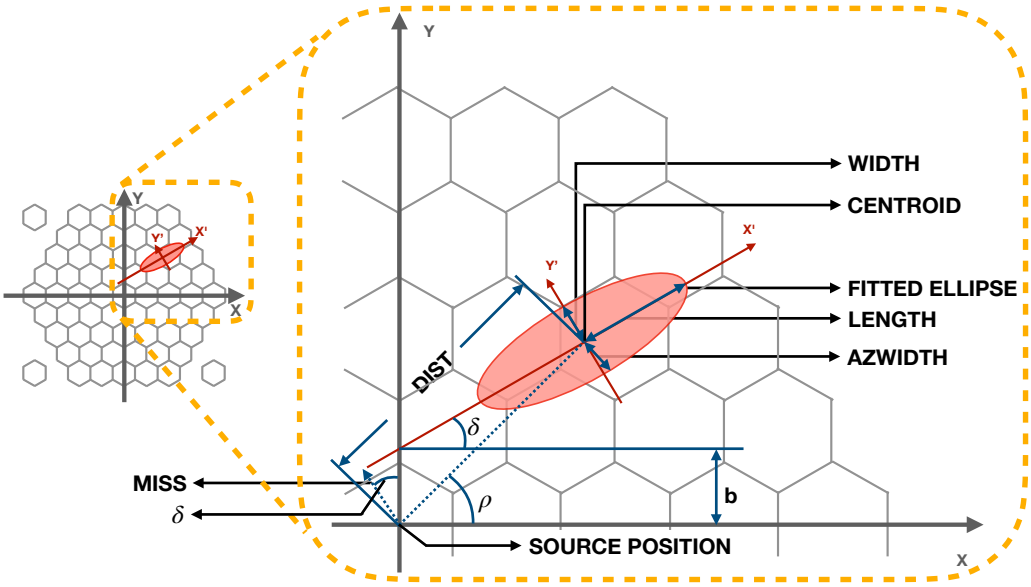

Figure 5.8: Hillas parameters of an ellipse associated to a detected EAS.

$$\begin{aligned}\hat{M}_{\mathrm{COG}} &= \left\langle (\vec{v}-\vec{v}_{\mathrm{COG}})(\vec{v}-\vec{v}_{\mathrm{COG}})^T \right\rangle \\ &= \frac{\sum_{i=1}^{N}(\vec{v}-\vec{v}_{\mathrm{COG}})\cdot(\vec{v}-\vec{v}_{\mathrm{COG}})^T \cdot s_i}{\sum_{i=1}^{N} s_i} \\ &= \begin{pmatrix} \mathrm{var}(x) & \mathrm{cov}(xy) \\ \mathrm{cov}(xy) & \mathrm{var}(y) \end{pmatrix}, \end{aligned} \tag{5.2}$$

Then, it is added over all the N pixels from the cleaned image. By calculating the eigenvalues and the eigenvectors of the covariance matrix, the new coordinate system is obtained which is located along the image axis. The other parameters are computed using this new system. [Bretz, 2006]

- $(\mathbf{X}_{\mathrm{COG}}, \mathbf{Y}_{\mathrm{COG}})$: COG coordinates of the cleaned image. They are calculated as the weighted mean of the pixels coordinates X_{COG} and Y_{COG}. Using the signal amplitude as the weight, they are computed by:

$$X_{\mathrm{COG}} = \frac{\sum_{i=1}^{N} X_i \cdot s_i}{\sum_{i=1}^{N} s_i} \quad \text{and} \quad Y_{\mathrm{COG}} = \frac{\sum_{i=1}^{N} Y_i \cdot s_i}{\sum_{i=1}^{N} s_i}. \tag{5.3}$$

- **Length:** RMS spread of light in the parallel direction to the fitted axis X'.

This is given by the direction of the eigenvector of the covariance matrix to the greater eigenvalue, in the eigenvector direction.

$$\text{length} = \sqrt{\text{var}(x) + \text{var}(y) - \sqrt{[\text{var}(y) - \text{var}(x)]^2 + [2 \cdot \text{cov}(xy)]^2}}. \quad (5.4)$$

- **Width:** RMS spread of light in the perpendicular direction to the fitted axis X' (parallel to Y'). It is given by the eigenvector of the covariance matrix to the smallest eigenvalue, in the eigenvector direction.

$$\text{width} = \sqrt{\text{var}(x) + \text{var}(y) + \sqrt{[\text{var}(y) - \text{var}(x)]^2 + [2 \cdot \text{cov}(xy)]^2}}. \quad (5.5)$$

- **Miss:** The perpendicular distance of the center of the field (the source) from the image axis.
- **AzWidth:** or Azimuthal-Width, is the RMS image width relative to a new axis that joins the source to the centroid of the image.
- **Dist:** The distance of the centroid of the image and the center of the camera. It is given by:

$$\text{dist} = \sqrt{X_{\text{COG}}^2 + Y_{\text{COG}}^2}. \quad (5.6)$$

- ρ : is the angle between the image centroid and the camera X axis. It's given by:

$$\rho = \arctan2(Y_{\text{COG}}, X_{\text{COG}}). \quad (5.7)$$

- δ : is the angle between the image X' axis and the camera X axis. It is given by:

$$\tan\delta = \frac{[\text{var}(y) - \text{var}(x)] + \sqrt{[\text{var}(y) - \text{var}(x)]^2 + [2 \cdot \text{cov}(xy)]^2}}{2 \cdot \text{cov}(xy)}. \quad (5.8)$$

- **Size:** is the size of the cleaned image. It is given by the sum of all image pixels, N, amplitudes:

$$\text{size} = \sum_{i=1}^{N} s_i. \quad (5.9)$$

- **b:** is the distance between the source position and the interception between the image X' axis and the camera Y' axis.
- **Leakage:** is the contribution of the outmost pixels of the cleaned image. It is given by the sum of the amplitudes of the outmost ring pixels, K, of the image:

$$\text{leakage} = \sum_{i=1}^{K} s_i. \tag{5.10}$$

This is just a set of all of the Hillas parameters that can be computed. There are more parameters like the *number of islands*, *number of pixels*, the *concentration*, the *assymetry*, and much more. As seen previously, most of the Hillas parameters are computed geometrically.
By determining the Hillas parameters of a detected event, is possible to characterize the primary particle that produced the detected EAS and have an idea of the possible particle that may produce it.
After all the preselection, cleaning, and parametrization processes, the HAWC's Eye parametrized data and the reconstructed HAWC's data can be synchronized to detect those events that were observed by both experiments almost at the same time.

5.3. Stereoscopic Observation

If an EAS is observed by one IACT, the reconstructed image is a 2-dimensional reconstruction, so then if two or more telescopes observe the same event, their camera images can produce a 3-dimensional reconstruction of the observed EAS. For this, it is needed to establish a coordinate system in which the orientation of the telescope and the camera is fixed. The xy-plane is parallel to the camera plane, while the z-axis is parallel to the telescope axis, as shown in Figure 5.9(a). One of both telescopes can be set as the origin telescope, to be the reference to the other telescopes. It must be assumed that both telescopes are pointing exactly to the same position in the sky; corrections on the telescope pointing can be performed by shifting the camera origin for each telescope.
Then, the shower axis can be characterized by its direction and core position. The direction can be described by the shower angle, θ, which is the angle between the EAS axis and the telescope axis, considering the projections θ_x and θ_y on the xz-plane and the yz-plane respectivelly[2]. [Kohnle et al., 1996]

[2]If the angle between the triggered showers and the telescope axis is minimal, the small-angle approximation can be used: $\sin\theta_{x,y} \approx \tan\theta_{x,y} \approx \theta_{x,y}$.

Figure 5.9(b) shows how the EAS angle θ is determined: when each telescope data has been analyzed and the cleaned images are obtained, both images are superimposed in the same coordinate system and, considering the absence of fluctuations in the EAS evolution and the analysis process, the EAS axis coincides with the image axis. Both the image of the source as well as the point where the EAS axis intersects the camera plane lie on this line. So, the EAS direction is determined by intersecting the axis of both images, giving in the intersection point $(-f\theta_x, -f\theta_y)$. The f denotes the focal length, and the signs account for the mirror reflection. The angular resolution of the stereoscopic system is governed by shower fluctuations and photon statistics, which are associated with uncertainties with the determination of the image center and, hence the image orientations; in particular, the determination is poor if the telescope's images are approximately collinear. [Kohnle et al., 1996, Ulrich et al., 1998]
Then, the shower core position is given by a similar method. Now, the telescope's images are located at the positions of the telescopes, as in Figure 5.9(c). Then, the major axis of each image is extended until all of them intersects. So, the intersection point is the reconstructed core position $(x_{\text{core}}, y_{\text{core}})$. Strictly, this process is just valid if the telescopes look at the zenith; otherwise, there is a distance d_{T_1,T_2}[3] between the image planes along the z-axis (Figure 5.9(a)), and also a small displacement $(d_{T_1,T_2}\theta_x, d_{T_1,T_2}\theta_y)$ of the EAS core location of the telescope which was not set as the reference telescope [Ulrich et al., 1998, Hillas, 2013].

5.4. Event Synchronization

When the observation campaign is performed, both HAWC's Eye telescopes and the HAWC observatory work simultaneously but recording data independent from each other. The synchronization analysis is made following the same process discussed in [Schaufel, 2017], but with the detectors previously described in Chapter 3.
Then, after the data-taking procedure of both experiments finishes, the recorded events must be synchronized. For this, each file of data must be reconstructed separately following the logic processes described before. To improve the HAWC reconstruction and reduce the computing time and memory space, a selection of the events recorded by HAWC with a trigger sigal from a HAWC's Eye telescope can be performed. For this, an XCDF-tool from the AERIE software can be used where the software channel associated for each PMT is specified, so all events that triggered that specific channel are stored, and the rest are rejected. Finally, after the selection of coincident events, the events reconstruction by HAWC can

[3] This case is an example of two telescopes T_1 and T_2. For an array of more telescopes, the distance between each pair must be computed.

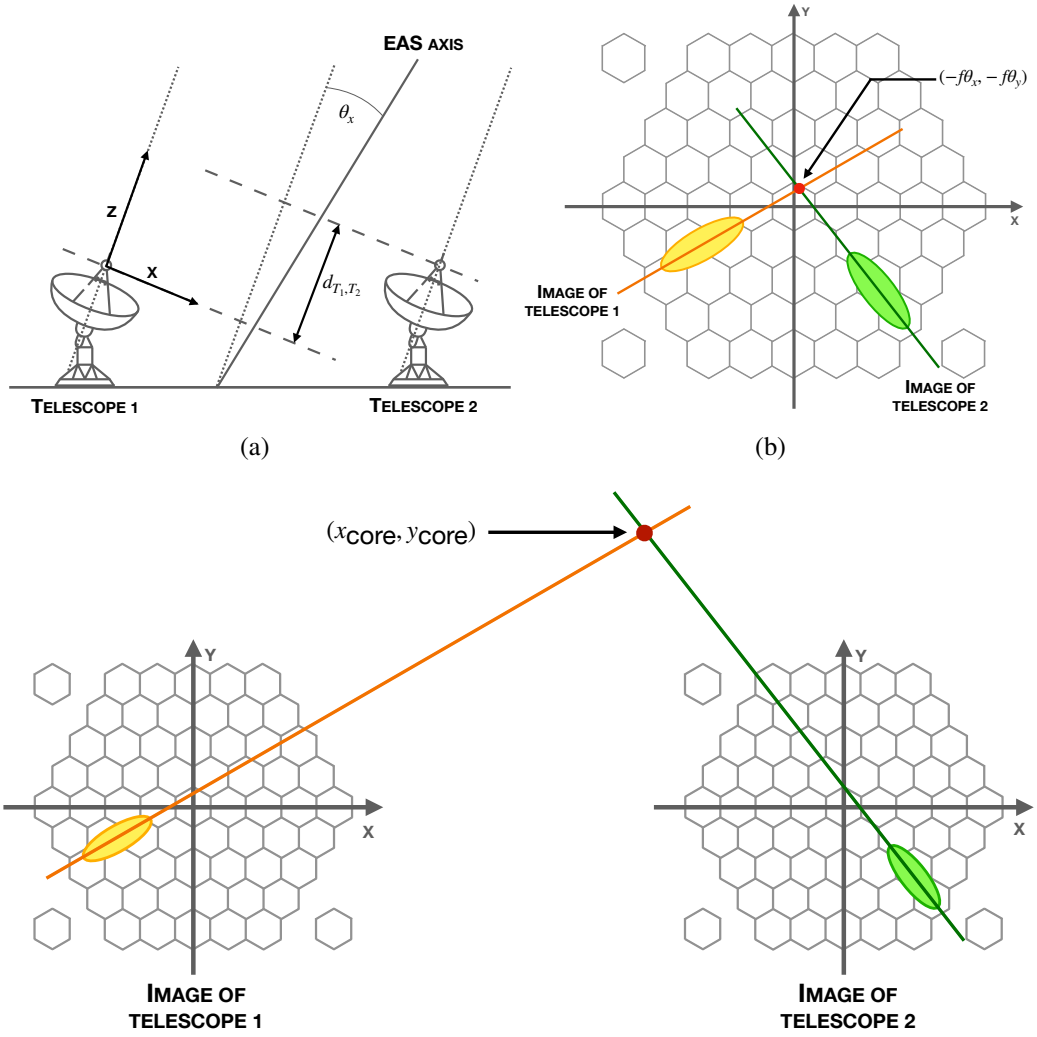

Figure 5.9: *(a)* Schematics of the geometry and coordinate system on a stereoscopic observation: the *xy*-plane denotes the camera plane, *z*-axis is orientated along the telescope axis; d_{T_1,T_2} is the distance of the image planes along the *z*-axis, and θ_x is the *x*-projection of the EAS angle. *(b)* Reconstruction method of the EAS angle: the camera images are superimposed and the lines parallel to the mayor axis of each one are intersected. The intersection point has to be mirrored with respect to the camera center, and the EAS angle is determined. *(c)* Reconstruction method of the EAS core: lines parallel to the mayor axis of the camera images are intersected, starting from the positions of the telescopes, considering a correction of the distance d_{T_1,T_2}.

be performed with just the necessary recorded events. After the recorded data was correctly selected and reconstructed, the synchronization can be done. To perform it, the events recorded by HAWC's Eye and HAWC have to be related to each other. For this, the minimum of the mean time difference between closest events in both trigger timestamps is searched, while the patterns are shifted against each other. Thus, the minimum value indicates the synchronization point, and all the events inside a time window of 1 ms from both data sets are assigned between each other. To perform the syncrhonization, the hardware clock (board counter in HAWC's Eye) is used instead of the PC timestamps of the telescopes events to avoud fluctiation in the timestamps. To convert the hardware counter into meaningul timestamps to synchronize with HAWC, a linear fit is performed between the counter and the telescope's PC time.The HAWC timestamps are shifted to the board's counter in steps of 100μs, and the mean time difference between HAWC's events and their closest telescope's events neighbours can be estimated:

$$\overline{\Delta t} = \frac{1}{N_{\mathrm{HAWC}}} \sum_{0}^{N_{\mathrm{HAWC}}} \left| t_{\mathrm{HAWC},i} - t_{\mathrm{Tel},i} \right| . \tag{5.11}$$

A simplified idea of the time shifting process is described in Figure 5.10.

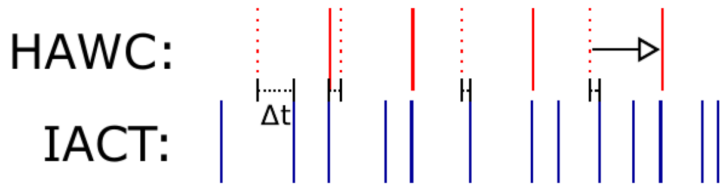

Figure 5.10: Schematics of the time synchronization process between HAWC and a telescope. For each pair of HAWC's and telescope's runs with an overlapping measurement time window, the events are synchronized by shifting the HAWC events with respect to their nearest telescope's neighbour events.

After shifting the events, a time window of 1 ms is considered to select the coincident events between both experiments. It has to be chosen carefully because in one hand it has to be small enough to reduce the random coincidence as most as possible, but in the other hand it must be large enough to not accidenally cut some events at the edge of the analyzed run.
Figure 5.11 shows all the logic steps described above.
Considering two HAWC's Eye telescopes were used during the observation, each telescope data set has to be synchronized with HAWC data independently. Then, both synchronized data sets (HAWC+HE01 and HAWC+HE01) are merged into one single set by selecting those HAWC events contained in both hybrid data sets

having the same event ID number. Finally, the resulting hybrid data set contains the events observed by HAWC and both HAWC's Eye telescopes.

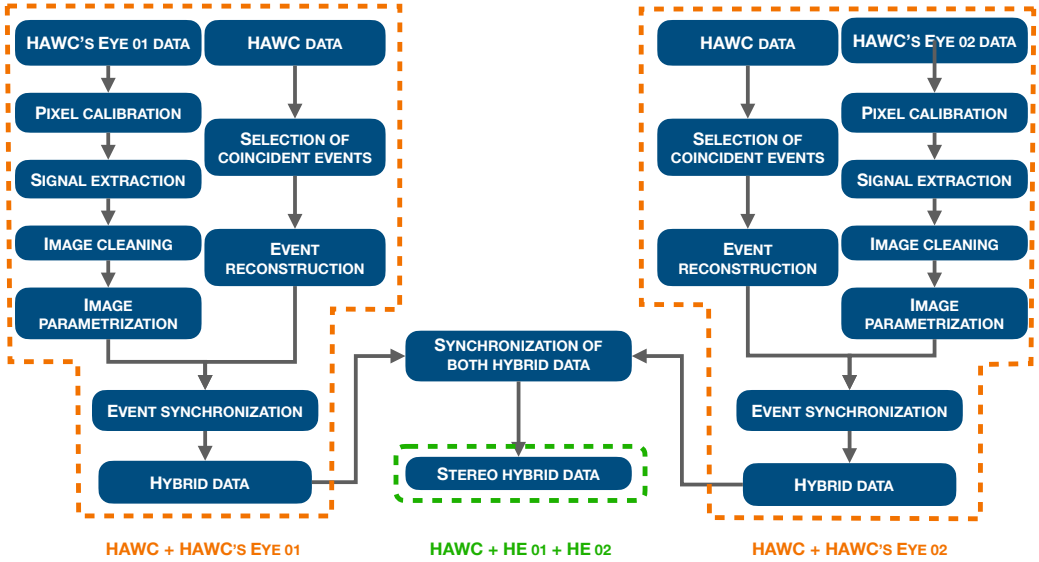

Figure 5.11: Logic steps for a correct synchronization of the HAWC's Eye telescopes data and the HAWC data. On the left side of the diagram first, the analysis on the HAWC's Eye 01 data is performed as well as the HAWC data, then they are synchronized and the synchronized events between HAWC and HAWC's Eye 01 are recorded. On the right side of the diagram, the same process is done but now with HAWC's Eye 02. Finally, after the events from both telescopes were correctly synchronized with HAWC independently, both data sets are synchronized with each other to obtain the final stereo hybrid synchronization. Adapted from [Audehm, 2020, Schaufel, 2017].

6

DATA ANALYSIS AND RESULTS

In the following chapter, the data recorded during the nights of 12th-13th and 13th-14th of November of 2020 with the HAWC's Eye telescopes and the HAWC observatory is analyzed, as the simulation performance as well.

6.1. Observational Data

6.1.1. HAWC Data

During the observation campaign of November 2020, the HAWC observatory had an average dead time of about 50 minutes associated with the start and stop of each data run, which represents $\sim 10\,\%$ of the full observation time. The main reason to perform the hybrid observation during these dates was because of the Crab Nebula being inside the HAWC FoV, considering it is the standard candle of gamma-ray sources. It's important to specify that the Crab Nebula is not inside the HAWC's FoV the full time, but just a few hours per day so is relevant to perform the observation campaigns during the moment in which the Crab is in the HAWC's FoV and also the environmental conditions that HAWC's Eye need are available. the estimated hours the Crab entered and left the HAWC's FoV are shown in Appendix A.

HAWC's data is stored in information packages called *runs*, which also are divided into smaller packages called *subruns*. This storage method is used to protect the data, because in case of losing or having a damage run the rest of the information will be safe. During both days of observation, HAWC created 378 subruns[1] of

[1]The subrun has a mean size of 2.1 Gb before the reconstruction, and 17 Gb after the reconstruction of parameters.

information associated with three different runs, which are specified in Table 6.1. This data was reconstructed using the AERIE software version Pass4, as specified in Chapter 5.

HAWC Data Runs			
1st night: 12-13 Nov		**2nd night: 13-14 Nov**	
Run 9719	Run 9720	Run 9720	Run 9721
Subruns 58-61	Subruns 1-150	Subruns 619-693	Subruns 1-150
Number of subruns: 154		**Number of subruns:** 224	
Total number of subruns: 378			

Table 6.1: HAWC's runs and subruns information of the recorded data during the 4th observation campaign performed on November 2020.

With the recorded events observed by HAWC, is possible to make a significance map of the Crab Nebula to measure the certainty of HAWC's detection. It can be done for each observation day, and for both days joined. Figures 6.1(a) and 6.1(b) shows the significance maps of the first and second nights of observation respectively, while Figure 6.1(c) shows the significance map of both nights joined.

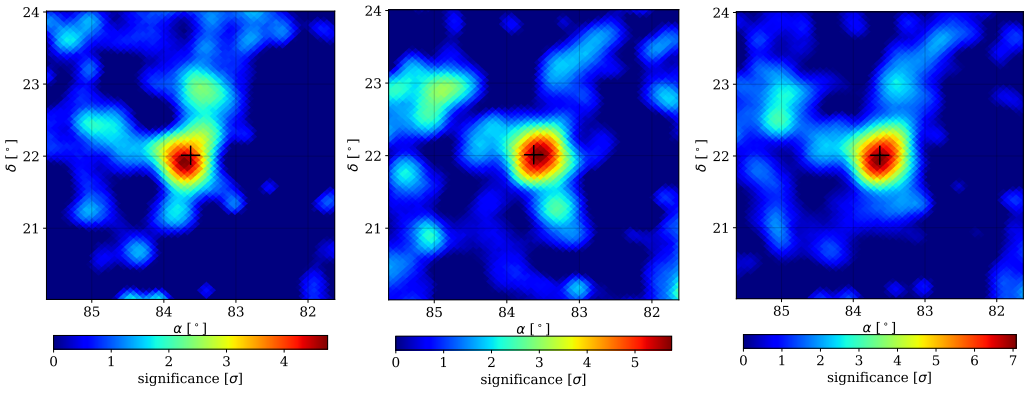

(a) (b) (c)

Figure 6.1: Significance map of the Crab Nebula with HAWC's data during the 4th observation campaign. *(a)* Significance map of the November 12-13, 2020 night. *(b)* Significance map of the November 13-14, 2020 night. *(c)* Significance map of both observation nights. The cross shows the real position of the source $(\alpha, \delta) = (83.6287, 22.0124)$ [UChicago, 2021]. A small displacement is observed between the cross and the place with maximum significance, and this is associated with the atmosphere fluctuations.

In each night the Crab Nebula was observed with a signal-to-noise ratio of $> 4\sigma$, that is very good considering the brief time of observation and having in mind that

5σ is the standard value to declare an observation[2]. With this information we can confirm that the performance of the HAWC observatory was correct during the observation campaign.

6.1.2. HAWC's Eye Data

During the observation campaign, the HE01 and HE02 telescopes recorded the observed events in runs, similar to the HAWC observatory storage method, resulting in 196 and 187 runs[3] for each telescope respectively. The information of the created runs for each telescope is shown in Table 6.2. Then, the Hillas parameters were computed with the MARS software (Chapter 5).

HAWC's Eye Data Runs†		
	HE01	**HE02**
1st night: 12-13 Nov	Runs 8-101	Runs 8-103
2nd night: 13-14 Nov	Runs 4-126	Runs 4-126
Total number of runs:	196	187

Table 6.2: HAWC's Eye telescopes runs information of the recorded data during the 4th observation campaign performed on November 2020. †The calibration files are not included.

The COG distributions of the events recorded by both HAWC's Eye telescopes are shown in Figure 6.2. Figure 6.2(a) shows an isotropic distribution of events, which means that the gain of the pixels was stable due to the temperature feedback, and so then the camera worked correctly during its performance. The COG distribution of the events observed by HE02 is shown in Figure 6.2(b) and there a different behavior can be appreciated. The main difference is that five low-statistics spots appeared, and this can be explained considering the four bad pixels in the HE02 camera (for more detail see Chapter 4 and Appendix A[4]). The remaining low-statistics spot is associated with a low-gain pixel that didn't work correctly during the campaign, and the reason for this can be wrong temperature feedback or a bad calibration of the pixel's voltage. Also, another minor difference is that de distribution shows a tiny high-statistics spot that can be associated with a wrong performance of a pixel due to its gain. The low-statistics spot is in the middle of pixels 7 and 20, meanwhile, the high-statistics spot is located in pixel 13 (for the

[2] A 5σ level represents that one chance in 3.5 million that a random fluctuation would yield the result.

[3] Each run have a mean size of $<$ 1.6 Gb before the parameters reconstruction and $<$ 120 Kb after.

[4] The image from Appendix A is reflected compared to the Figure 6.2(b) because the photograph was taken front.

camera mapping, see Appendix A), so further analysis must be done to find the reason for this behavior and solved it. Despite this, these pixels can be used for analysis.

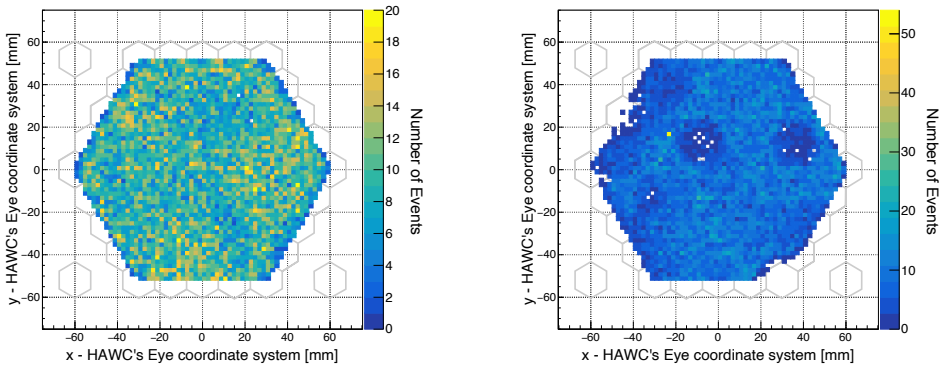

(a) (b)

Figure 6.2: COG of events observed with both HAWC's Eye telescopes during the 4th observation campaign in November 2020. *(a)* Events COG distribution for the HE01 camera, resulting in an isotropic distribution as expected. *(b)* Events COG distribution for the HE02 camera, showing low-statistics spots due to the dead pixels in this camera, as expected too.

The different performance of both cameras was already expected because the issues in the HE02 camera were well known, and this means that both telescope DAQ systems worked correctly during the campaign.
During each day of the observation campaign, the different parameters like the temperature, the current, and the trigger rate, were monitored for both telescopes. In particular, the trigger rate gives important information: if the rate is high it could mean that a visible-light source is in the FoV, or the selected threshold was low; if the rate is low, it could mean that the night is too dark or the selected threshold is high. Quality plots can be made with this information. Figure 6.3 shows the quality plots for each telescope during the 13th to 14th of November (second) night. The trigger rate plot in Figure 6.3(a) shows the trigger rate all night long for HE01 having a low-rate baseline during the observation, and a clear peak at $\sim$ 1:30 hrs HAWC's local time, which corresponds to the transit of Ceta Tauri through the telescopes FoV, which is a double-star system near the Crab nebula. Meanwhile, Figure 6.3(b) shows the development of HE02 during the observation. Here, the trigger rate plot shows a variating baseline which can be associated with a low threshold used, so more counts were recorded. Despite the low threshold, a peak can be found at $\sim$ 1:30 hrs HAWC's local time too, which means that HE02 saw Ceta Tauri too. Also, for HE02 more peaks can be found along the observation nigh, in particular the trigger rate increased since $\sim$ 3:30 hrs, which can be associated to the moonrise. The moon light did not affect so much HE01 because it was placed

between some WCD which protected it from external light, meanwhile HE02 was placed beside the Counting House which is not so high as a WCD and did not shield HE02 from external light. Comparing both plots (and the quality plots from the first night), can be notice that HE01 had a more stable performance during the observation campaign, and HE02 had a low threshold which let more noise being recorded. Despite all the differences between the performance of both telescopes, both telescopes had a good performace during the observation campaign, recording enough good data to be analized. The four quality plots of the observation campaign (of both nights with both telescopes) can be found in Appendix A.

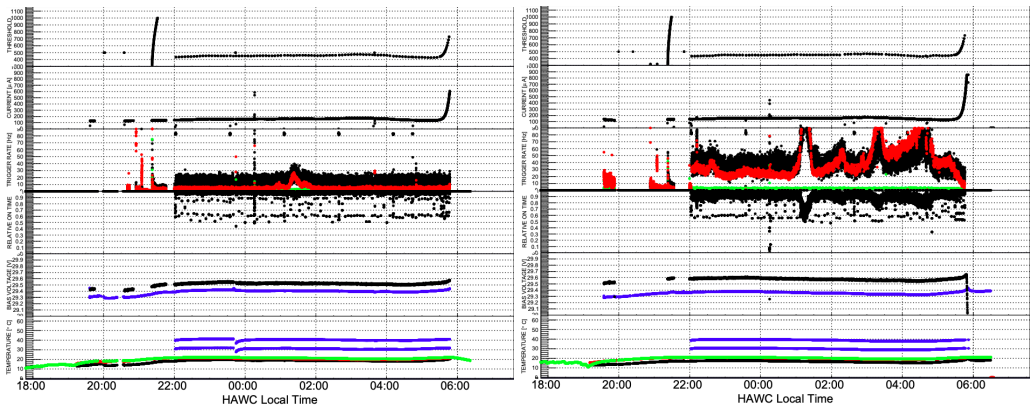

(a) (b)

Figure 6.3: Quality plots for *(a)* HE01 and *(b)* HE02 during the 13th to 14th November (second) night of observation. The trigger rate peak at $\sim 1:30$ hrs HAWC's local time for both telescopes is associated with the transit of Ceta Tauri in the telescope's FoV, which is a double-star system near the Crab nebula.

After confirming the correct performance of HAWC and the two HAWC's Eye telescopes, the time synchronization between HAWC's events with each telescope must be done.

6.1.3. Events Synchronization

As previously described in Chapter 5, to make a proper time synchronization, the time calibration between the timestamps of the telescopes board counters and the PC time must be done. For this, the counter timestamps are converted in UTC by using the PC timestamps. This process is applied for every pair of runs in which measurements of HAWC and each telescope overlaps. Figure 6.4(a) shows an example of the resulting time calibration applied for HAWC's run9720-subrun29 and HE01's run23, and Figure 6.4(b) shows an example of the time calibration of HAWC's run2720-subrun18 and HE02's run18.

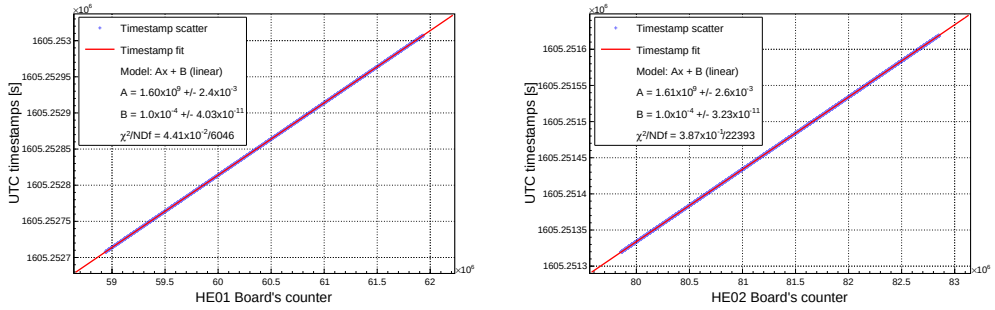

(a) (b)

Figure 6.4: Telescopes timestamps calibration with HAWC's PC time. *(a)* Timestamps calibration of HE01. *(b)* Timestamps calibration of HE02.

For each HE event, a time window of 1 ms was fixed to search for all the HAWC events that lay inside that time range synchronizing the events that match in time, but also HAWC's and HE's data have a time shift between them because of the different observation techniques. So, the synchronization is performed for different shift times, and the time difference between the events of both datasets is computed, finally, the mean time difference of every shift time used is computed. On one hand, if there are no synchronized events, the mean time difference distribution will not have a global minimum value; meanwhile, if there are synchronized events, a global minimum value of the meantime difference will appear. Figure 6.5 shows the mean time distributions obtained during the synchronization of HAWC with HE01 and HAWC with HE02.

After confirming a correct synchronization process performed, the HAWC's and HE's information of the synchronized events became complementary and a single event can be analyzed with both observation techniques. And because both techniques are complementary to each other, sometimes some events are observed with both techniques both with different levels of precision depending on the advantages and disadvantages of the technique used. Considering this, quality cuts must be implemented in the databases to select all the events that Figure 6.6 shows the distributions of the synchronized event's cores estimated with HAWC. There can be observed that both distributions have their maximum at the HE's positions, which confirms that the synchronization process was correctly done because all the events were observed by both experiments.

To reject the most number of events associated with the background noise, quality cuts must be applied. Some cuts are associated just with the HAWC's performance, and other ones with the HAWC's Eye telescopes performance, but also some of them are associated with the hybrid performance. For example, the image size of the telescopes is related to the energy of the detected event, so a quality cut

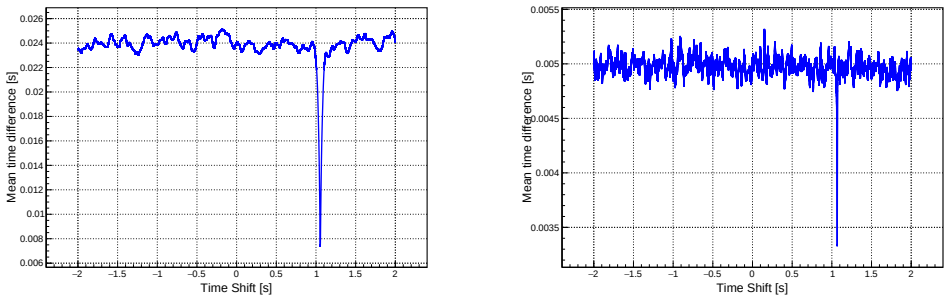

(a) (b)

Figure 6.5: A global minimum value on the meantime difference distribution represents a correct synchronization of events between two datasets (i.e. HAWC + 1 telescope). *(a)* Meantime difference distribution obtained during the HAWC and HE01 synchronization. *(b)* Meantime difference distribution obtained during the HAWC and HE02 synchronization. Both distributions have a global minimum of $1.055 \pm 5 \times 10^{-3}$ s. The baseline of HE02 is more oscillating compared to the HE01 baseline due to more background recorded by that telescope.

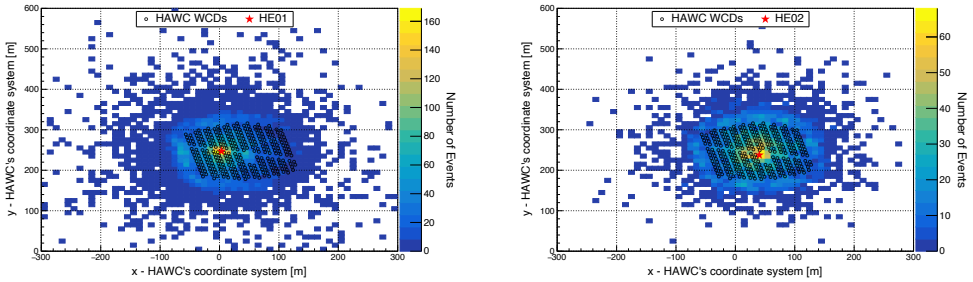

(a) (b)

Figure 6.6: Distributions of the synchronized event's cores. *(a)* Distribution for events observed by HAWC and HE01. *(a)* Distribution for events observed by HAWC and HE02. The red stars represent the position of the telescopes in the HAWC coordinate system. These distributions do not have any quality cuts applied.

can be obtained comparing HAWC's energy estimation and the HAWC's Eye telescopes image size. Figure 6.7 shows the relation between the HAWC's energy estimation and the telescope's image size.

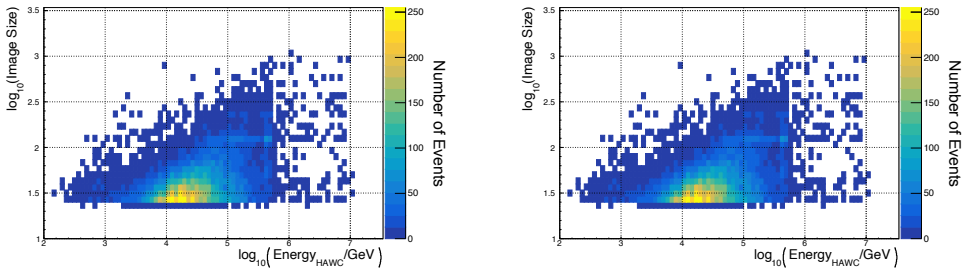

(a) (b)

Figure 6.7: Correlation between the HAWC's estimated energy of the observed events against the image size produced in the telescopes'cameras, for *(a)* HE01 and *(b)* HE02.

So then, the quality cuts used in this work are:

- **rec.angleFitStatus==0**: status of the HAWC's angle fit, where 0 ==good.
- **rec.coreFitStatus==0**: status of the HAWC's core fit, where 0 ==good.
- **rec.nHit>500**: number of triggered HAWC's channels (PMTs).
- **rec.lgNNEnergy<6**: logarithmic of the energy estimated by HAWC, in GeV, using neural networks.
- **rec.zenithAngle<6**: zenith angle of the events recorded by HAWC, in degrees.
- **rec.PINC∈[0.5,4.5]**: HAWC's PINCness gamma/hadron separator.
- **Leakage1<0.3**: signal fraction of the outmost ring of the HAWC's Eye camera, as explained in Chapter 5.
- **Width>0.025**: is the RMS spread of light in the Y'ḋirection, as explained in Chapter 5.

6.1.4. Stereoscopic Observation

As mentioned before, stereoscopic observation refers to a simultaneous observation of events by two or more telescopes. For this specific case, the stereoscopic observation analysis was performed using the hybrid data of HAWC with each one of both HAWC's Eye telescopes, i.e. a hybrid stereoscopic data analysis was done. Figure 6.8 shows the event's core distribution for all the events observed by HAWC and both HAWC's Eye telescopes. The distribution has its maximum value between both telescopes, which is congruent with the premise that there is no preference between neither of both telescopes.

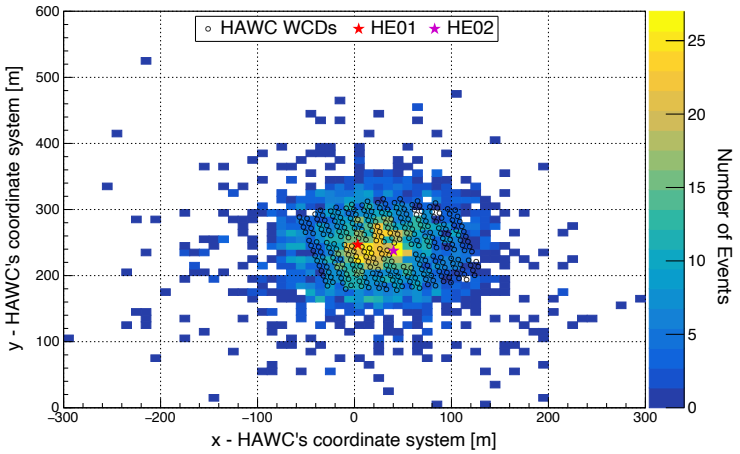

Figure 6.8: Distribution of the event's core distribution for those events observed simultaneously with HAWC and with both HAWC's Eye telescopes, i.e. hybrid stereoscopic events.

The number of recorded events changed drastically since the original number of events recorded during the observation campaign, passing through the reconstruction and cleaning process, and finally the quality cuts. Table 6.3 shows the number of events recorded in each step of the analysis, considering the observation of each experiment and its reconstruction process separately, and also the number of events recorded in hybrid and stereoscopic performance.

As shown in Table 6.3, the final number of hybrid synchronized events represents $\sim 0.009\,\%$ of the total number of events initially recorded by HAWC, and the $\sim 0.5\,\%$ and $\sim 0.2\,\%$ of the total events recorded by HE01 and HE02 respectively. This confirms that most of the recorded events are associated with the background, or with events that do not fit into the experiment's characteristics, as the FoV.

To properly characterize the system, the observational results must be compared to the simulation results. In the following section, the simulation analysis is described and its results are shown.

HAWC	
Total recorded events: 34115933	
Channel 23 recorded events: 490261	
HAWC's Eye	
HE01 calibrated events: 633767	HE02 calibrated events: 1765504
HE01 reconstructed events: 66639	HE02 reconstructed events: 80592
Synchronized events without cuts	
HAWC + HE01: 20939	HAWC + HE02: 18645
Synchronized events with cuts	
HAWC + HE01: 9464	HAWC + HE02: 10310
Hybrid stereoscopic events with cuts	
HAWC + HE01 + HE02: 2932	

Table 6.3: Number of events recorded for each step of the analysis chain, considering the data reconstruction for each experiment separately and the hybrid and stereoscopic performance as well.

6.2. Simulation Performance

To simulate the performance of both HAWC's Eye telescopes, a simulation library was created where the characteristics of the HAWC observatory were considered. For the simulation of the telescopes, the position of the telescopes in the HAWC's site, the elevation, and the atmosphere model was used, matching the HAWC's environment. // Extensive air-showers were simulated with CORSIKA v7.69 [Heck et al., 1998], contemplating gamma-rays and protons as the primary particles with energies between 1 TeV and 100 TeV, and an integral spectral index of -1.5. So far, more than three million simulated events were produced for each species. The CORSIKA configuration used for the simulated events is shown in Table 6.4.
Further details of the simulation's setup can be found at [Serna-Franco, 2021, Rehbein, 2021].
The MARS analysis software was used for the image reconstruction, as with the observational data. To study the energy and arrival direction of the recorded events, a Random Forest [Albert, 2008] based package, *Ranger* [Wright and Ziegler, 2015], was used.
The Random Forest (RF) algorithm is a machine learning method of classification and regression, based on a collection of decision trees, built up with some elements of random choices. The RF creates a set of largely uncorrelated trees and combines their results to form a generalized predictor [Albert, 2008].

Parameter	Value/Range
Energy spectrum slope	-1.5
Energy range	1 TeV - 100 TeV
Zenith angle	0°
View cone	8°
Shower core scattering area	500×500 m^2
Observation height	4100 m
Cherenkov wavelength range	250 nm - 700 nm
Atmospheric model	US standard atmosphere (7)
Magnetic field	27.717 μT (hor.); 29.902 μT (vert.)
Hadronic interaction model	GHEISHA (low-energy); QGSJET (high-energy)

Table 6.4: CORSIKA configuration used for the simulated events. [Rehbein, 2021]

The RF must be trained to achieve the best prediction possible. Propper training depends on several parameters that steer the growth of trees, and which the user should be aware of, like the number of trees, the node size, and more.
For this work, the total sample of simulated events was divided into two subsets. One subset was constituted by 70 % of the total dataset, and it was used to train the algorithm; meanwhile, the other subset was made up of the remaining 30 %, which was the events to be analyzed. The RF was trained for regression of $\log_{10}(E)$ and the arrival direction of the events for each telescope and each particle species individually, based on ten image parameters from the cleaned, i.e. background free, image. The image parameters used are:

- *Alpha, Dist, Length, Width*: the so-called Hillas parameters which describe the orientation, location and shape of the image.
- *log10SizeMainIsland*: logarithm of the sum of the signals of the brightest cluster of pixels.
- *Leakage1*: fraction of the total signal in the outermost pixel-ring of the camera.
- *TimeSpread*: spread of the arrival times of all image signals.
- *TimeSpreadWeighted*: spread of the arrival times weighted with the pixel signal.

In addition, the simulated *Impact* parameter of the primary particle relative to the telescope's position smeared with a two-dimensional Gaussian distribution with a width of $\sigma = 4$ m was included. The distribution width was selected because it corresponds to the average resolution of HAWC.

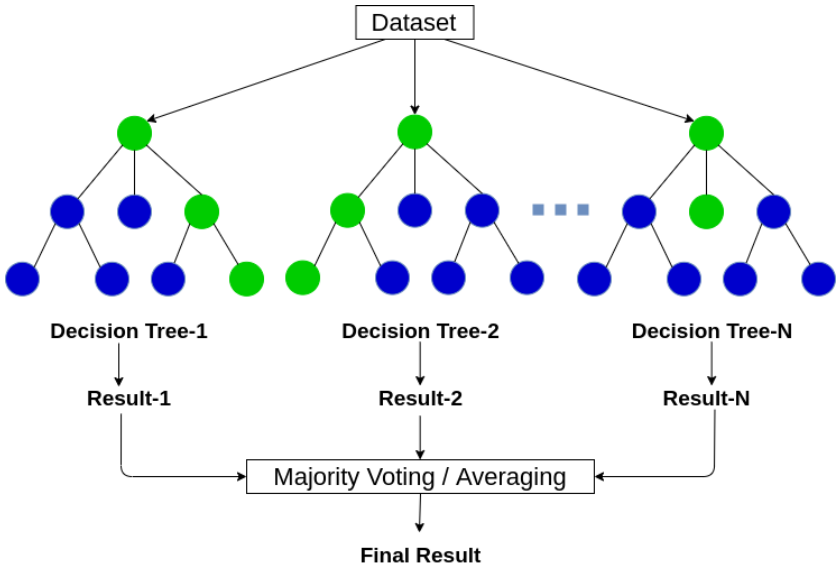

Figure 6.9: Diagram of the logic steps in the Random Forest method. First, the method must be trained with a controlled dataset, and then the method is feed with a test dataset. With the information of the test dataset, predictions are made by N random-decision trees, where each tree will give an individual prediction. Finally, the resulting prediction is the average of the N individual predictions or the most repetitive value. [Pool, 2021]

6.2.1. Arrival Direction Prediction

The arrival direction of the events is an important feature to be reconstructed/predicted and analyzed, considering that photons are not deflected by magnetic fields, so then their arrival direction provides information of the source where they come from. The arrival direction of the events can be reconstructed geometrically as explained in Chapter 5, or it can be predicted using RF. To make a correct prediction of the arrival direction with RF, the cartesian projections $\theta \sin\phi$ and $\theta \cos\phi$ are trained and predicted, where θ and ϕ are the zenith and azimuth angles of the events, respectively. The reason to train the RF with cartesian coordinates is that RF does not handle cylindric variables well. The arrival direction in cartesian coordinates is:

$$(x, y) = (\theta \cos\phi, \theta \sin\phi)\,. \tag{6.1}$$

Then, θ and ϕ angles can be estimated by,

$$\Rightarrow \theta = \sqrt{x^2 + y^2} = \sqrt{(\theta \sin\phi)^2 + (\theta \cos\phi)^2}, \tag{6.2}$$

and,

$$\Rightarrow \phi = \tan^{-1}\left(\frac{y}{x}\right) = \tan^{-1}\left(\frac{\theta \sin\phi}{\theta \cos\phi}\right). \tag{6.3}$$

So then, Figure 6.10 shows the zenith angle correlations of HE01 and HE02, considering gamma-rays and protons as primary particles. The perfect correlation is described by the identity line (red) and can be noticed that the distributions follow the identity tendency, and the width of each distribution is related to the resolution of the experiment. The HAWC's Eye quality cuts, Leakage1<0.3 and Width>0.025, were applied for these correlations; the rest of the quality cuts used for the observational data were not used because those correspond to HAWC parameters, and this analysis just involved HAWC's Eye data. Also, it can be noticed that the distributions became flat at $\log_{10}(E_{\text{Pred}}/\text{GeV}) \approx 5.5$, while this behavior do not appears for $\log_{10}(E_{\text{Pred}}/\text{GeV})$. The reason for this is that the library of events was simulated up to 8° for the zenith angle, but due to the simulated view cone of the telescopes, only those events smaller than 6° were detected by the telescopes, and that is why the predicted values are smaller than 6°.
Now, the azimuth angle correlations of HE01 and HE02 with gamma-ray and proton events are shown in Figure 6.11. These distributions do not have weights of the flux dependency applied neither. Similar to the zenith angle distributions, the red line corresponds to the identity which represents a perfect correlation. For gamma-rays and protons, the distributions follow the same tendency as the identity line which means that the azimuth angle prediction was done correctly. No global maximums can not be found in these distributions, which means that the detected events come isotropically as expected. The HAWC's Eye quality cuts Leakage1<0.3 and Width>0.025 were applied for these distributions as well.

6.2.2. Angular Resolution

Now, with the arrival direction angles correctly predicted, the angular distance can be computed, which is,

$$\Delta = \cos^{-1}\left(\vec{r}_{\text{MC}} \cdot \vec{r}_{\text{Pred}}\right). \tag{6.4}$$

In an ideal case, the telescopes would have a Gaussian PSF and there would not be any global offset between the telescopes, so then the angular distance Δ could be described by a Gaussian distribution centered around zero. But for this case, the Δ distribution can be described by a Rayleigh distribution,

$$f(x|\sigma) = \frac{x}{\sigma^2} \cdot e^{-\frac{x^2}{2\sigma^2}}, \quad \text{where} \quad \sigma^2 = \sigma^2_{\text{HE}}, \tag{6.5}$$

where σ corresponds to the variance of the fitted distribution, and it physically represents the angular resolution of the telescope, and it is computed for the zenith

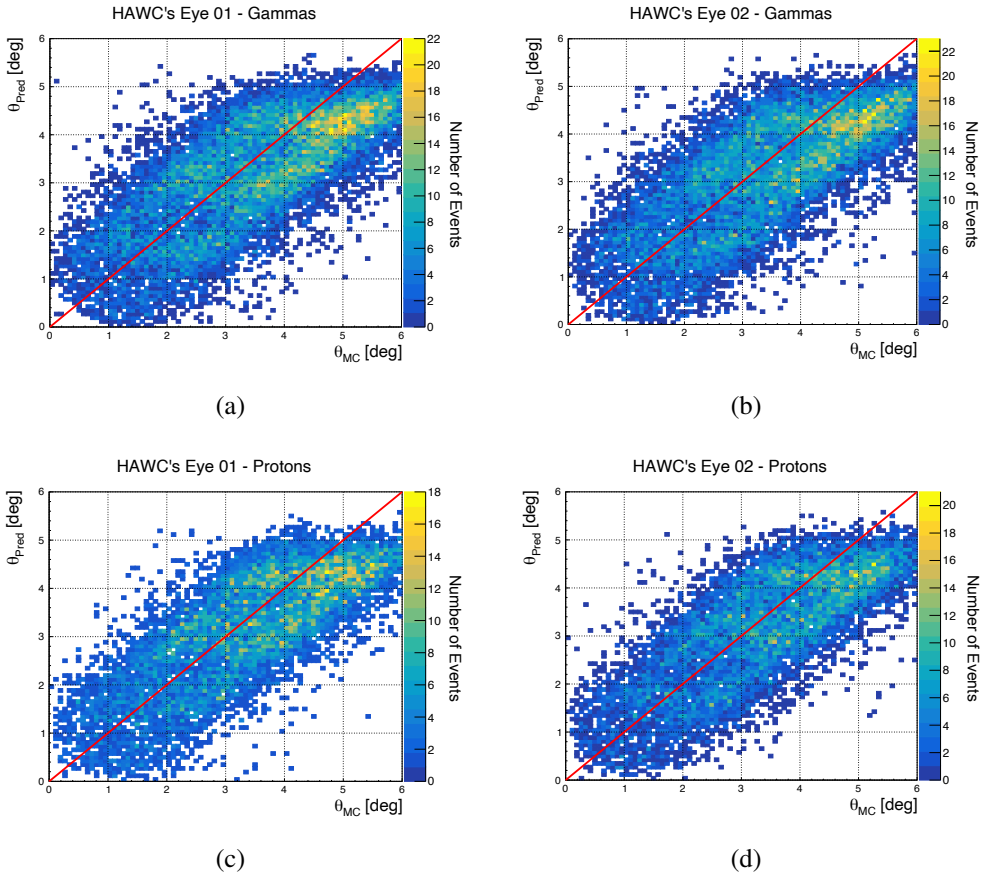

(a) (b)

(c) (d)

Figure 6.10: Zenith angle correlation between the Monte Carlo (MC) value, and the RF prediction. *(a)* Zenith angle distribution of HE01 with gamma-ray events. *(b)* Zenith angle distribution of HE02 with gamma-ray events. *(c)* Zenith angle distribution of HE01 with proton events. *(d)* Zenith angle distribution of HE02 with proton events. The red line is the identity line which represents a perfect correlation.

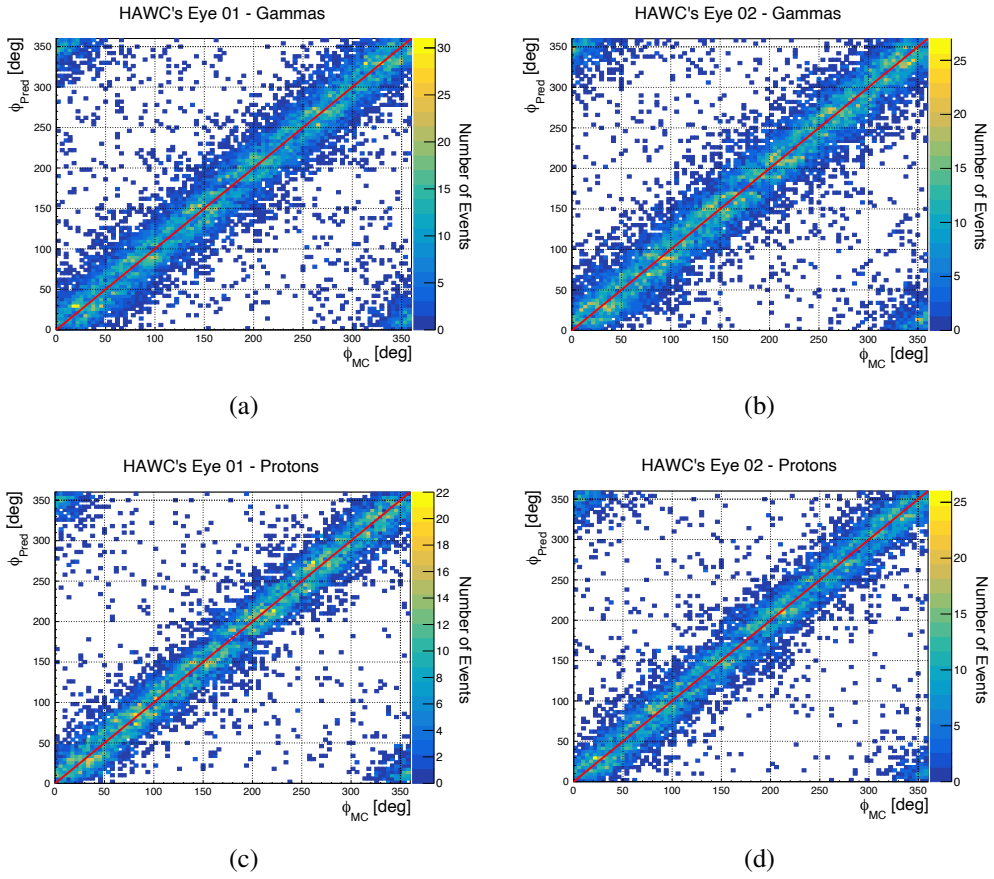

(a) (b)

(c) (d)

Figure 6.11: Azimuth angle correlation between the Monte Carlo (MC) value, and the RF prediction. *(a)* Azimuth angle distribution of HE01 with gamma-ray events. *(b)* Azimuth angle distribution of HE02 with gamma-ray events. *(c)* Azimuth angle distribution of HE01 with proton events. *(d)* Azimuth angle distribution of HE02 with proton events. The red line is the identity line which represents a perfect correlation.

angle. Figure 6.12 shows the angular resolution computed for both telescopes individually, and the average between both as well, which can be associated with the angular resolution of the experiments in stereoscopic performance. The resolution was computed considering gamma-ray and proton events. Edge effects below the energy threshold and at the limit of the simulated energy range are visible.

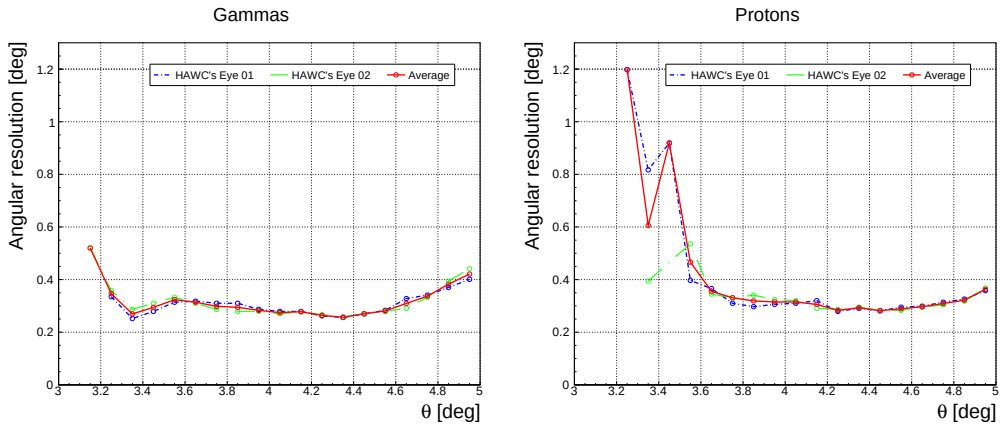

(a) (b)

Figure 6.12: Angular resolution computed for the two HAWC's Eye telescopes and the average with both, considering gamma-ray and proton events. *(a)* Angular resolution of HE01 (blue dashed line), HE02 (green dashed line), and the average of both (red solid line), obtained with gamma-ray events. *(b)* Angular resolution of HE01 (blue dashed line), HE02 (green dashed line), and the average of both (red solid line), obtained with proton events.

Table 6.5 shows the minimum values of the angular resolution for each telescope individually, and the average between both as well. The average value of both telescopes can be understood as the angular resolution of the stereoscopic system. The minimal angular resolution obtained for the system is approximately 0.25° for gamma-rays and 0.28° for proton events. These values can be compared to the angular resolution of other IACTs like HESS, which is 0.1° for individual photons [Aharonian et al., 2005], or like MAGIC's which is $\sim 0.07^\circ$ for energies bigger than 300 GeV [Cañellas et al., 2012]. The angular resolution of the HAWC's Eye telescopes is in the same order of magnitude as other IACTs much bigger and much expensive ones. Also, the angular resolution of the HAWC's Eye telescopes is a little bit bigger than others because the energy of the events detected by the HAWC's Eye telescopes is higher than the rest of the IACTs: while HESS or MAGIC have their best angular resolution for gamma-ray events at hundreds of GeV, the best angular resolution for gamma-rays of the HAWC's Eye telescopes is at $\log_{10}(\mathrm{E/GeV}) = 4.35$ which is $E \simeq 22.38$ TeV. It is an important improvement for the high-energy astronomy instrumentation because it means that the HAWC's

Eye telescopes are suitable to constitute a hybrid experiment with HAWC because the energy range of both experiments fits between each other.

Gammas			
$\log_{10}(\text{Energy}/\text{GeV})$	HE01 Angular Resolution (±0.001) [deg]	HE02 Angular Resolution (±0.001) [deg]	Average Angular Resolution (±0.001) [deg]
4.35	0.258	0.256	0.0257
Protons			
$\log_{10}(\text{Energy}/\text{GeV})$	HE01 Angular Resolution (±0.001) [deg]	HE02 Angular Resolution (±0.001) [deg]	Average Angular Resolution (±0.001) [deg]
4.25	0.279	0.287	0.0283

Table 6.5: Minimal angular resolution for both telescopes individually and the average between both as well, specifying the energy associated.

6.2.3. Energy Prediction

The energy can be predicted directly with RF, and the energy of the simulated events goes from 1 TeV up to 100 TeV. The correlations of the MC energy and the predicted energy for gamma-ray and proton events are shown in Figure 6.13.
As expected from shower physics, the gamma-rays energy prediction is slightly better. Also, both telescopes show a peak in their distributions at high energies, and this is because no weights were applied to correct the flux dependency considering the solid angle. As well, at the lowest and highest energies, an unavoidable prediction bias is visible due to the cut-off of the distribution by the energy threshold and the limitation of the simulated energy range.
Once the energy was correctly predicted, the energy resolution can be computed as well.

6.2.4. Energy Resolution

To estimate the angular resolution of the HAWC's Eye telescopes, the MC and predicted energies are needed. The relation to computing the energy resolution is,

$$\sigma_E = \frac{1}{\sqrt{N}} \sqrt{\sum_{i=1}^{N} \left[\log_{10}(E_{\text{Pred,i}}) - \log_{10}(E_{\text{MC,i}})\right]^2}, \tag{6.6}$$

where N is the number of events contained in each bin where the resolution is computed. It was computed for both telescopes independently and the average between both. The energy resolutions for gamma-ray and proton events are shown in Figure 6.14.
As for the angular resolutions, for the energy resolutions edge effects below the energy threshold and at the limit of the simulated energy range are visible as well.

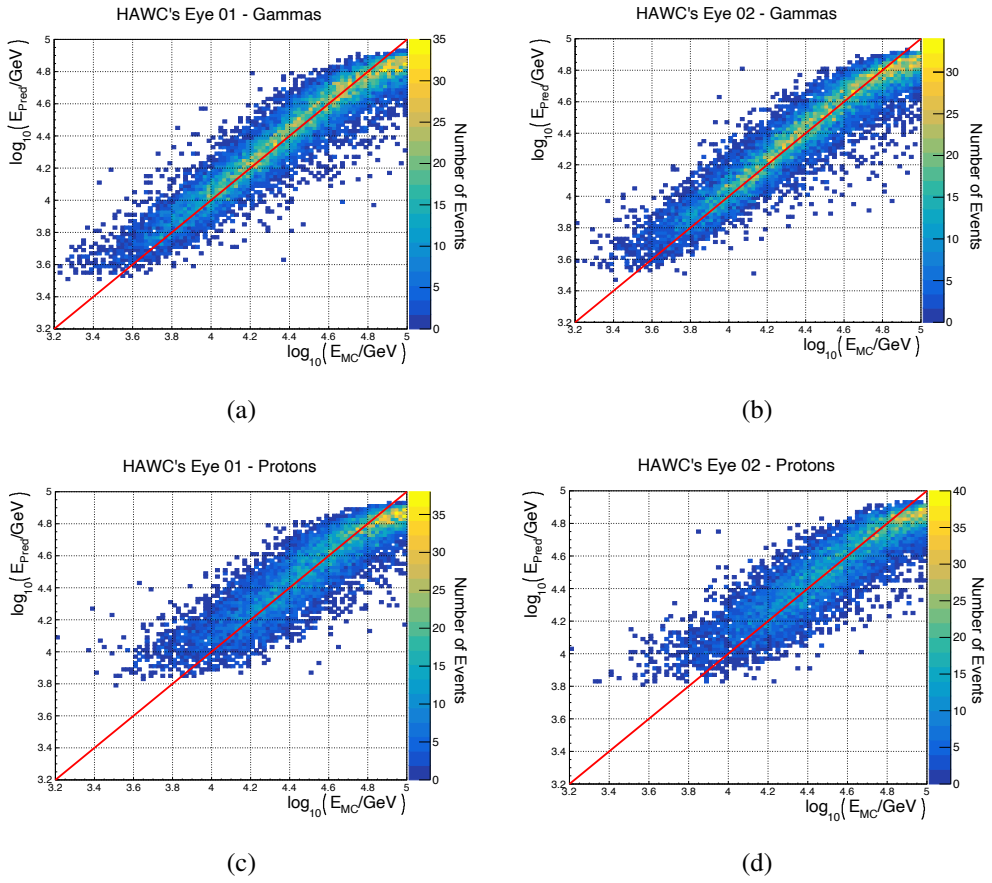

(a) (b)

(c) (d)

Figure 6.13: Energy correlation between the Monte Carlo (MC) value, and the RF prediction. *(a)* Energy distribution of HE01 with gamma-ray events. *(b)* Energy distribution of HE02 with gamma-ray events. *(c)* Energy distribution of HE01 with proton events. *(d)* Energy distribution of HE02 with proton events. The peak of the distribution towards high energies originates from the flat simulated spectrum with a slope of only -1.5. The red line is the identity line.

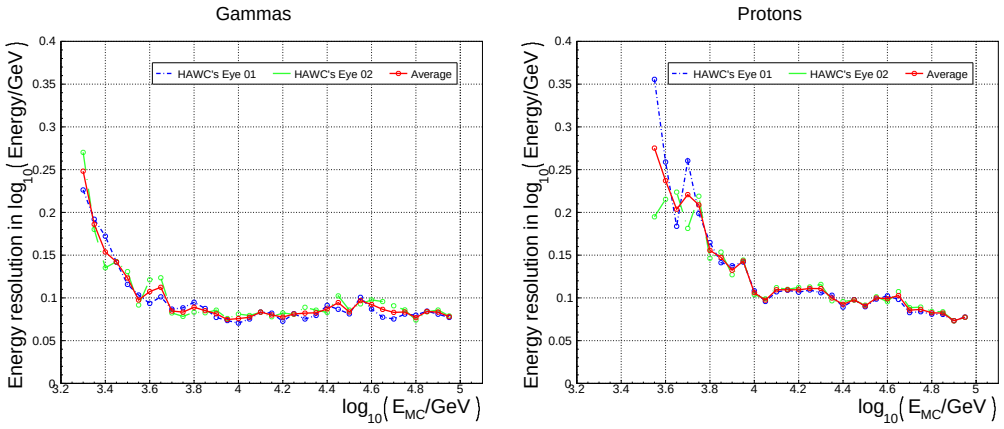

(a) (b)

Figure 6.14: Energy resolution computed for the two HAWC's Eye telescopes and the average with both, considering gamma-ray and proton events. *(a)* Energy resolution of HE01 (blue dashed line), HE02 (green dashed line), and the average of both (red solid line), obtained with gamma-ray events. *(b)* Energy resolution of HE01 (blue dashed line), HE02 (green dashed line), and the average of both (red solid line), obtained with proton events.

As expected, the best energy resolution is obtained with gamma-ray events; the distribution of the angular resolution for gamma-rays is more stable compared to the distribution obtained with protons. The angular resolution for gamma-rays is about < 1.2 TeV for events with energies higher than 5 TeV, but for events with energies lower than that, the resolution grows exponentially.
These values confirm the idea that these telescopes are perfect to perform a hybrid observation, because they have a very good energy resolution, even that they are small and compact telescopes compared to the usually IACTs.

7

Conclusion and Outlook

This thesis aimed to characterize two compact Imaging Air Cherenkov Telescopes called *HAWC's Eye*. For this, a hybrid observation campaign with the High Altitude Water Cherenkov (HAWC) observatory was done. During the observation campaign, the new generation of HAWC's Eye telescopes was used, which have cameras of 64 pixels each, and each pixel had a hex-to-square Winston cone-shaped light-guide and a SiPM photosensor of the type SenseL MicroFJ. Additionally, the DAQ system of each telescope was based on the FACT telescope's DAQ.

In November 2020 the hybrid observation campaign was performed using the two HAWC's Eye telescopes in simultaneous performance with the HAWC observatory, having approximately 13 hours of observation time, which was analyzed. Also, the HAWC's Eye telescopes were theoretically characterized by analyzing their performance with simulations of gamma-ray-induced and proton-induced particle air-showers.

The analysis was divided into two parts: the observational data analysis and the simulation analysis. First, with the observational data, the performance of the instruments was studied by producing a significance map of the Crab Nebula with HAWC getting a significance for the source of $> 7\sigma$, confirming the good operation of the instrument during the campaign. The Crab Nebula is the standard candle of gamma-ray astronomy because it is the brightest gamma-ray source in the sky.
Then, the distributions of the center of gravity of the recorded events by each HAWC's Eye telescope were successfully produced. The distributions were as expected confirming the good operation of the cameras during the observation, even that one of them had some damaged pixels. Additionally, the trigger-rate distribu-

tions for each telescope were computed, which showed that both telescopes registered the light coming from noisy sources like Ceta Tauri which is a visible-light source that entered into the field of view of the telescopes during the campaign. This indicates that the DAQ of both telescopes worked properly during the observation.
This observation campaign is the longest one of all performed with the HAWC's Eye telescopes during the Crab Nebula transit in the HAWC's site. With this, the performance of the HAWC's Eye telescopes DAQ and hardware were tested over long periods. The DAQ system had some minor problems during the campaign, but they were working back again fast, which means that there was a short observation dead time.
While HE01 recorded the information perfectly, there was a bigger amount of noise on the data recorded by HE02 because the trigger threshold was low for this particular telescope. This is associated with the gain of the SiPMs in the HE02's camera, so a solution is to recalibrate the gain of the pixel or fix a higher threshold of its DAQ. This issue can be easily solved in the next observation campaign.

Afterward, from HAWC's and HAWC's Eye's databases, those events that were observed and recorded by both instruments simultaneously were selected, i.e. the events recorded by hybrid observation (HAWC + 1 HAWC's Eye) and those recorded by hybrid stereoscopic observation (HAWC + 2 HAWC's Eye), getting > 9000 hybrid events and ~ 3000 hybrid stereoscopic events. With these events, the shower's core distributions were obtained, showing a double-gaussian distribution centered around the HAWC's Eye position in the HAWC's coordinate system. This means that the peak of the recorded events is close to the position of the HAWC's Eye telescope considered for the event's synchronization, suggesting that the event's selection process was successful in which a time-window of 1 ms (with steps of 100 μs) was chosen to synchronize the events.
In the second part of the analysis, the HAWC's Eye telescopes were simulated considering the same environmental conditions as the HAWC's site, and the position of the telescopes into the HAWC's coordinate system was the same as during the observation campaign as well. For this analysis, a simulation library of more than 3 million gamma-ray-induced and proton-induced particle air-showers was produced with CORSIKA, and using the Machine Learning algorithm Random Forest, the energy and arrival direction of the events were predicted. To predict these parameters, the Random Forest was successfully trained, where the energy was directly predicted, and the arrival direction, which is in spherical coordinates, was reconstructed from the predicted cartesian coordinates. The correlation between the true and the predicted zenith and azimuth angles was successfully computed, and they showed the telescope's response depending on the energy and the arrival direction of the detected event. Furthermore, the energy and angular

resolution of the telescopes individually and in stereo performance were calculated. For gamma-ray events, the energy resolution is < 1.2 TeV and the angular resolution is 0.35°, both for primary energies higher than 5 TeV; and for protons, the energy resolution is < 1.2 TeV and $\sim 0.6^{\circ}$ for primary energies higher than 10 TeV. As expected from shower physics, the resolutions for gamma-ray events are better than the ones from proton events. These results are consistent with the energy and angular resolutions of IACTs like HESS and MAGIC, indicating the good characterization of the telescope, but understanding that some more updates and modifications can be done to improve the performance of the telescopes.

The results obtained during this work are consistent with previous estimations done, and some improvements were obtained. The data-taking process, the analysis chain, and the analysis of results showed the path to be followed to improve the observational campaigns, and the HAWC's Eye telescopes performance as well. With all of this, the compact IACTs HAWC's Eye are confirmed as an important candidate to be considered as upgrades for WFD, where hybrid observations are considered. At this moment, the HAWC's Eye telescopes seem to be an important upgrade for WFD like HAWC and IceCube, but also they become a viable option for future experiments with hybrid observations like The Southern Wide-field Gamma-ray Observatory (SWGO), which is a HAWC-like WFD planned to be constructed in the southern hemisphere to map the full south hemisphere sky, considering that there is any WFD which have done that mapping before. Also, an important feature of the telescopes to be considered as a viable option is the low cost of production, because this represents that more telescopes can be built with less money than the cost of a large size telescope like the rest of the IACTs.

A

APPENDIX A

A.1. Poisson Distribution

Most of binary processes can be characterized by a constant and small probability of success for each individual trial. Particle beam experiments are a good example of this, because many particles from an accelerator might strike a target for every recorded reaction product. Considering these conditions, the approximation holds that the success probability is small and constant, and the binomial distribution reduces to the Poisson form:

$$P(x) = \frac{(pn)^x e^{-pn}}{x!}, \tag{A.1}$$

because $pn = \bar{x}$ holds for this distribution as well as for the parent binomial distribution:

$$P(x) = \frac{\bar{x}^x e^{-\bar{x}}}{x!}, \tag{A.2}$$

which is the common form of the Poisson distribution.
Then, the binomial distribution requires values for two parameters: the number of trials n and the individual success probability p. From equation A.2 can be noticed that a significant simplification has occurred: only one parameter is required, which is the product of n and p. This is a very useful simplification because now is just needed the mean value of the distribution in order to reconstruct its amplitude at all other values of the argument. That is a great help for processes in which the mean value can be estimated or measured in some way, but for which there is no idea of either the individual probability or the size of the sample, as usually in astrophysical measurements.

Fome properties of the Poisson distribution follow directly. First, it is also a normalized distribution:

$$\sum_{x=0}^{n} P(x) = 1. \tag{A.3}$$

Also the first moment or mean value of the distribution can be calculated:

$$\bar{x} = \sum_{x=0}^{n} xP(x) = pn, \tag{A.4}$$

which is the result also obtained for the binomial distribution. The predicted variance of the distribution, however, differs from that of the binomial and can be evaluated from the first definition:

$$\sigma^2 \equiv \sum_{x=0}^{n} (x-\bar{x}))^2 P(x) = pn, \tag{A.5}$$

and from equation A.4:

$$\sigma^2 = \bar{x}. \tag{A.6}$$

Then, the predicted standard deviation is just the square root of the predicted variance:

$$\sigma = \sqrt{\bar{x}}. \tag{A.7}$$

Thus, the predicted standard deviation of any Poisson distribution is just the square root of the mean value that characterizes that same distribution.
Finally, a fluctuation can be defined as deviations of the value of an observable from its average or, also, deviations of the actual time evolution of an observable from its average evolution in a system subject to random forces or, simply, undergoing chaotic motion.

A.2. Mapping SiPMs Layout

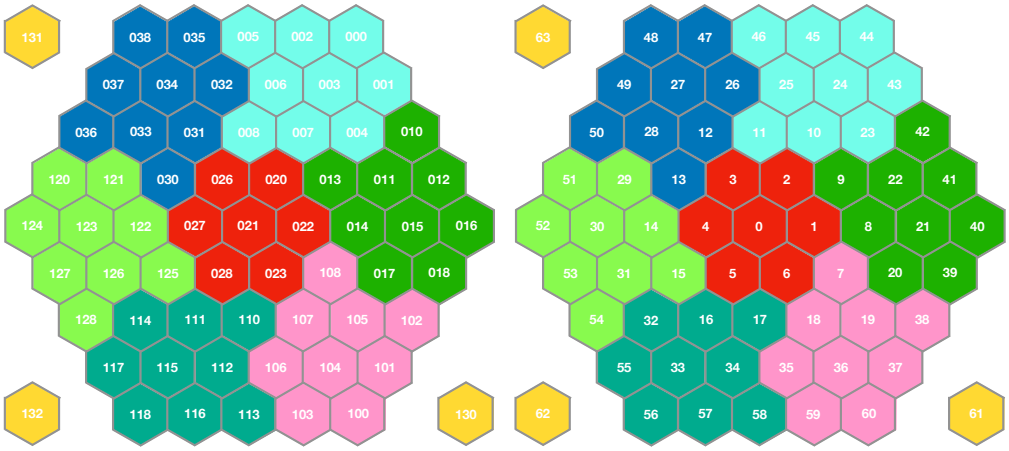

Figure A.1: Mapping used in the HAWC's Eye cameras from an above point of view. *Left:* Hardware mapping of the SiPM pixels to the FPA boards. Each pixel numbers follows the logic Board|Patch|Pixel. Each color represents a set of pixels contained in a same patch. *Right:* Mapping used for the analysis enumerating the pixels from 1 to 64 continously; the order assigns the analysis outputs (Sw ID) to each pixel in the camera. Layout taken from the FACT++ framework.

A.3. Telescope's Connection Plate

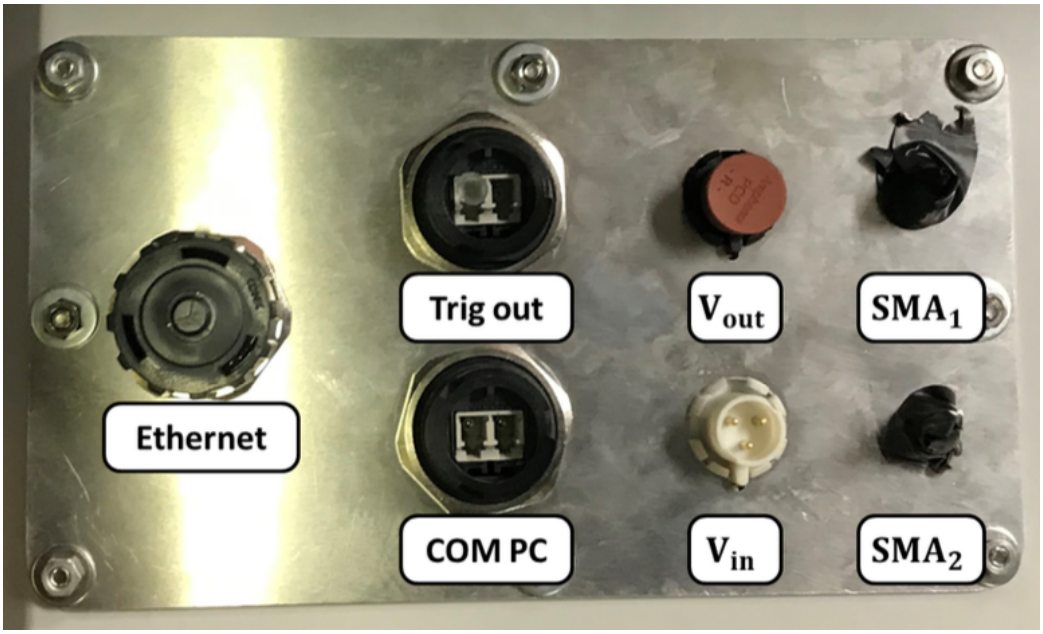

Figure A.2: Aluminum plate used for the pass-through into the closed box, where the connectors are located. The SMA connectors are not used. [Audehm, 2020]

A.4. Observation Campaign's Crews

(a) (b)

(c)

Figure A.3: *(a)* Crew on-site during the 1st observation campaign on July 2017. From left to right: Rubén Alfaro, Arturo Iriarte and Merlin Schaufel. *(b)* Crew on-site during the 2nd observation campaign on September 2019. From left to right: Jan Audehm, Rubén Alfaro, Yunior Pérez and Jesús Martínez. (C) Crew on-site during the 4th observation campaign (same as during the 3rd campaign) on November 2020. From left to right: José Serna, Rubén Alfaro, Arturo Iriarte and Abel Sánchez (site crew member).

A.5. Telescope Damaged Camera

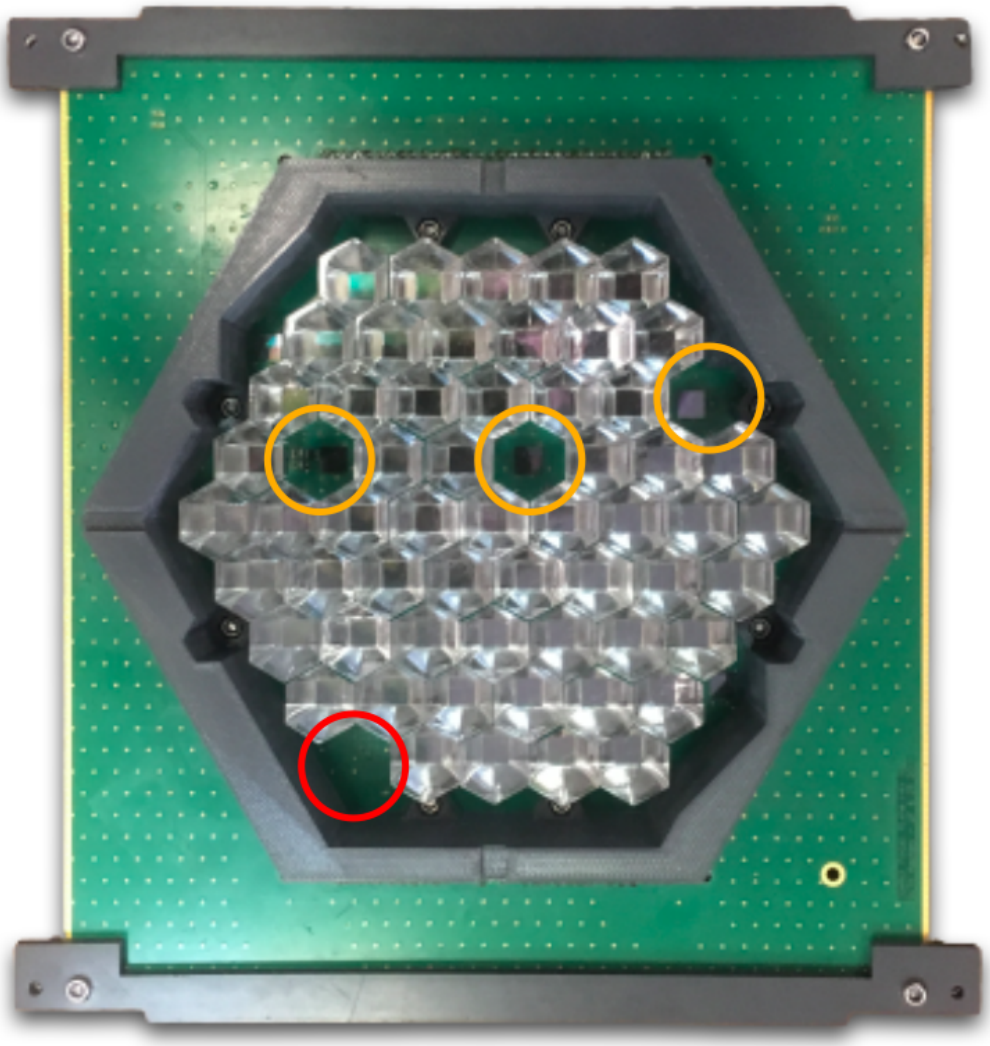

Figure A.4: HE02 damaged camera in which three light-collectors unglued from the SiPMs (yellow circles) and one SiPM pixel ripped off from the camera with the light collector (red circle).

A.6. HAWC's Layout

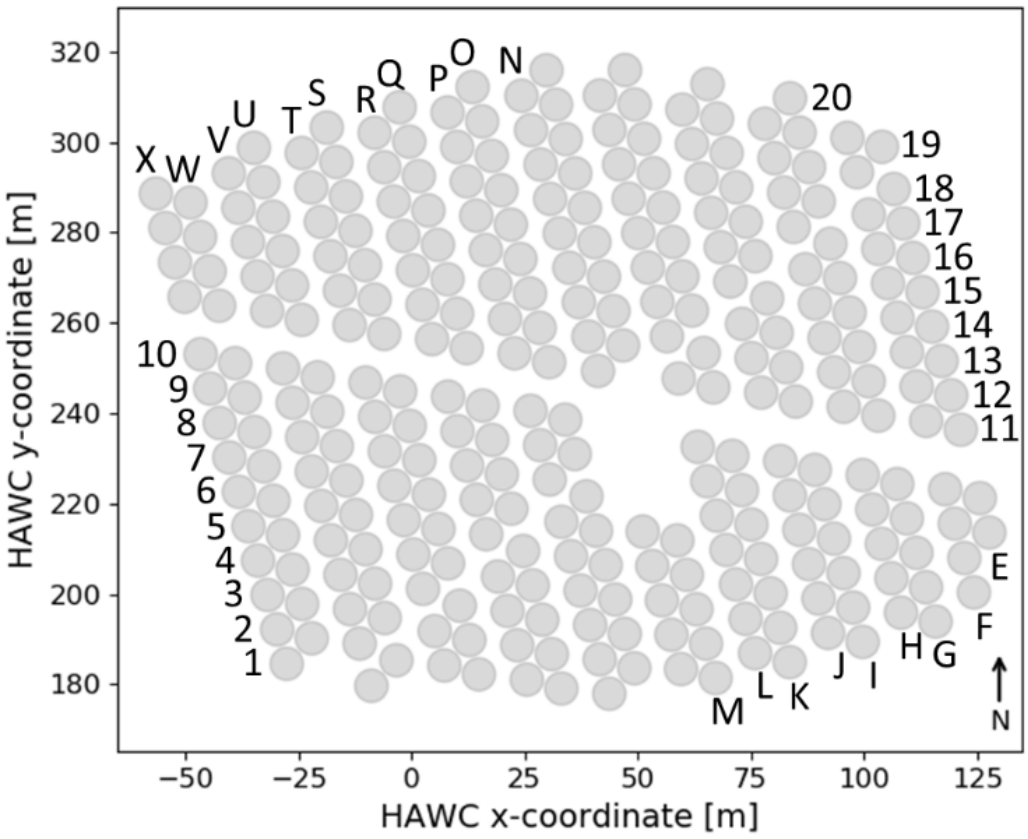

Figure A.5: Layout of the WCDs of the HAWC observatory. Layout taken from the AERIE software.

A.7. 4th Observation Campaign's Rate Scans and Quality Plots

A.7.1. HAWC's Eye Telescopes Rate Scans

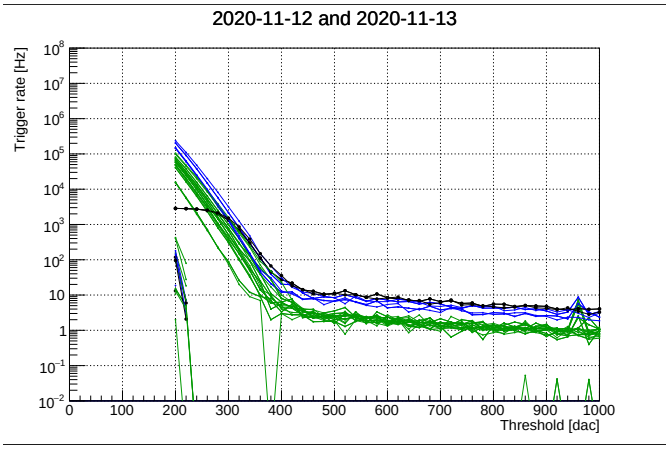

(a)

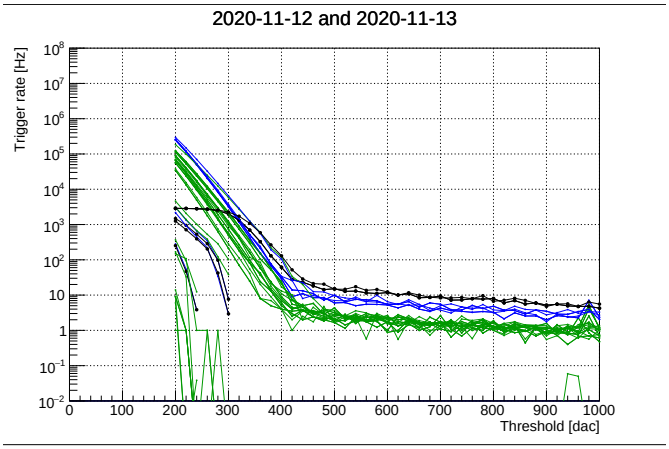

(b)

Figure A.6: Rate scans performed for both telescopes, on both nights. The threshold (in DAC counts) was changed from 200 DAC counts to 1000 DAC counts and the trigger rate (in Hz) was recorded. Green curves are the rate scans of the patches, blue curves for the boards and the black curves are the mean value of the trigger rate for the whole telescope. *(a)* Rate scans for both nights for HE01. *(b)* Rate scans for both nights for HE02.

A.7.2. HAWC's Eye Telescopes Quality Plots

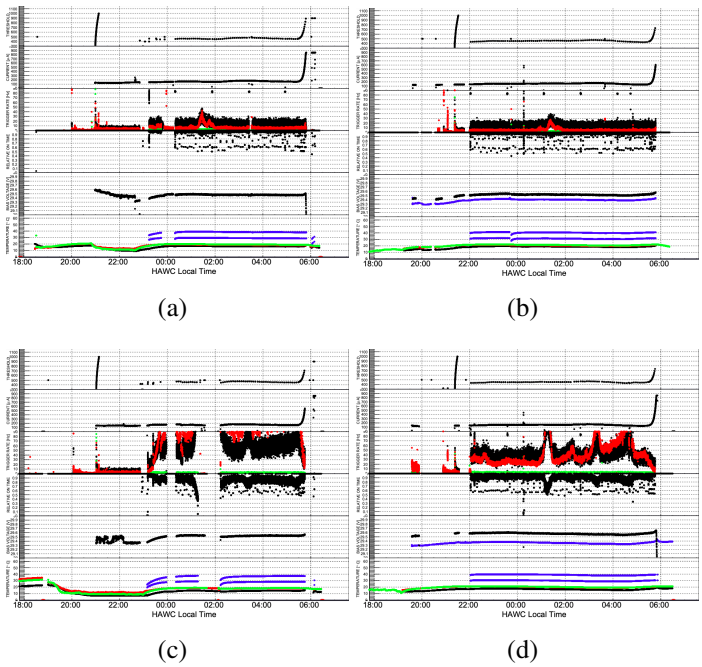

(a) (b)

(c) (d)

Figure A.7: *(a)* Quality plot of HE01 during the first observation night (12th to 13th of November, 2020). *(b)* Quality plot of HE01 during the second observation night (13th to 14th of November, 2020). *(c)* Quality plot of HE02 during the first observation night (12th to 13th of November, 2020). *(b)* Quality plot of HE02 during the second observation night (13th to 14th of November, 2020). All plots show the variation of differents telescope parameters during the time of observation. The time-dependent parameters plotted are, from top to bottom: the telescope's threshold in DAC counts, the camera's current in μA, the telescope trigger rate in Hz, the relative on time, the camera's bias voltage in V, and the telescope's temperature in °C. The discontinuities on the trigger rate plots are due to the stop of the telescopes DAQ. Also, on *(a)* and *(b)* the peak on the trigger rate at 1:30 HAWC local time on both plots is associated with Ceta Tauri, which is a double star system near the Crab Nebula, passing through the telescopes FoV. Meanwhile on *(c)*, compared to HE01 quality plots, the trigger rate plot of HE02 of the first night seems to be high, which represents a larger amount of background signals recorded. Then, on *d*, HE02 second night, the threshold was higher, and the trigger rate got low and even the Ceta Tauri transit was seen by the telescope, but still, a large amount of background data was recorded.

A.8. Crab Nebula into the HAWC's FoV

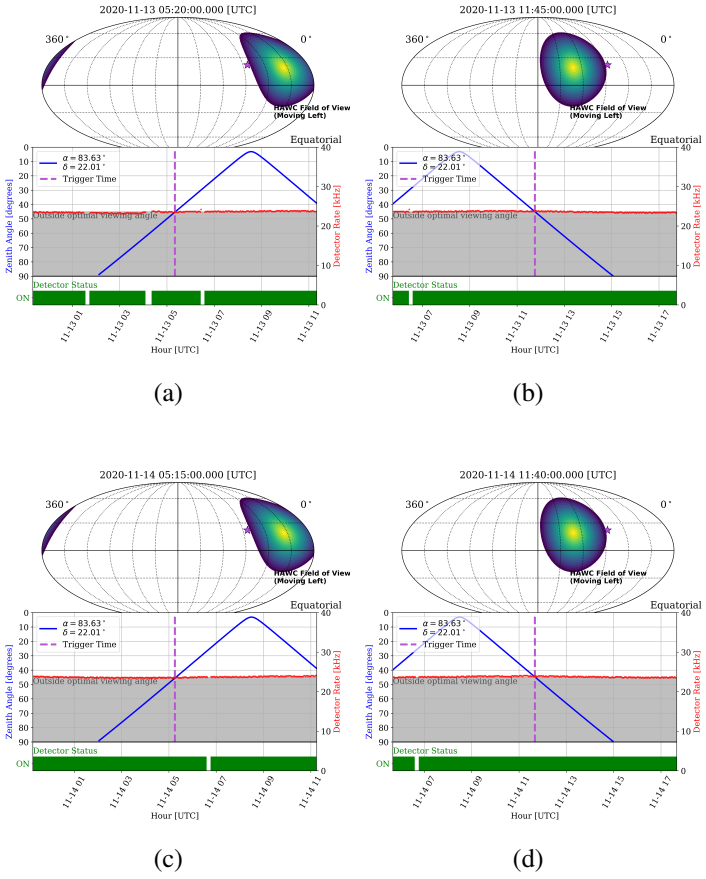

Figure A.8: Upper diagram: the purple star shows the position of the Crab Nebula in equatorial coordinates. The blue-to-yellow contours show the HAWC's FoV, where the blue and yellow colors represent where HAWC is less and more sensitive, respectively. The time and date shown is in UTC. Mid diagram: shows the zenith angle of the Crab during its transit into the HAWC's FoV. Bottom diagram: shows the detector status, i.e. when it is on or off. The four diagrams correspond to *(a)* the Crab Nebula getting into the HAWC's FoV on November 13, *(b)* the Crab Nebula getting out of the HAWC's FoV on November 13, *(c)* the Crab Nebula getting into the HAWC's FoV on November 14 and *(d)* the Crab Nebula getting out the HAWC's FoV on November 14.

A.9. Quality cuts'plots

rec.nHit> 500

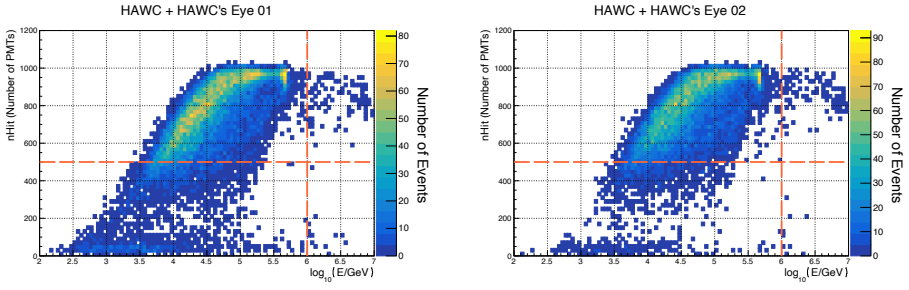

(a) (b)

Figure A.9: Quality cut of *rec.nHit*> 500 considered for the hybrid data between HAWC and *(a)* HAWC's Eye 01 and *(b)* HAWC's Eye 02.

rec.lgNNEnergy< 6

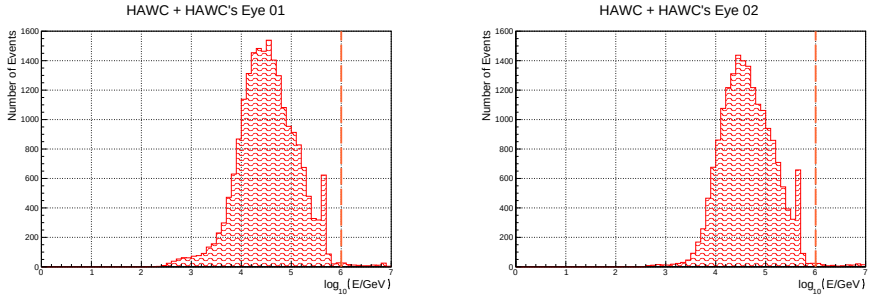

(a) (b)

Figure A.10: Quality cut of *rec.lgNNEnergy*< 6 considered for the hybrid data between HAWC and *(a)* HAWC's Eye 01 and *(b)* HAWC's Eye 02.

rec.zenithAngle< 6

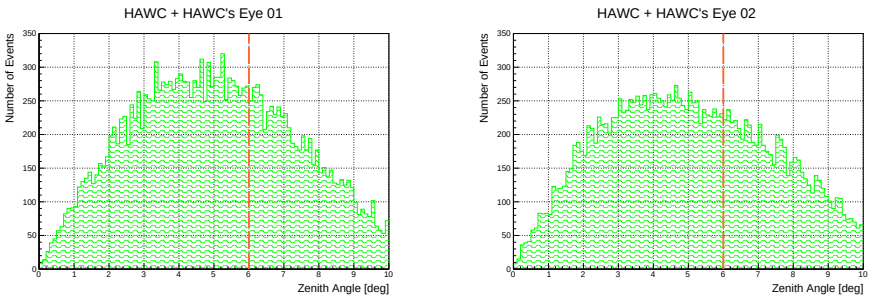

(a) (b)

Figure A.11: Quality cut of *rec.zenithAngle*< 6 considered for the hybrid data between HAWC and *(a)* HAWC's Eye 01 and *(b)* HAWC's Eye 02.

rec.PINC$\in [0.5, 4.5]$

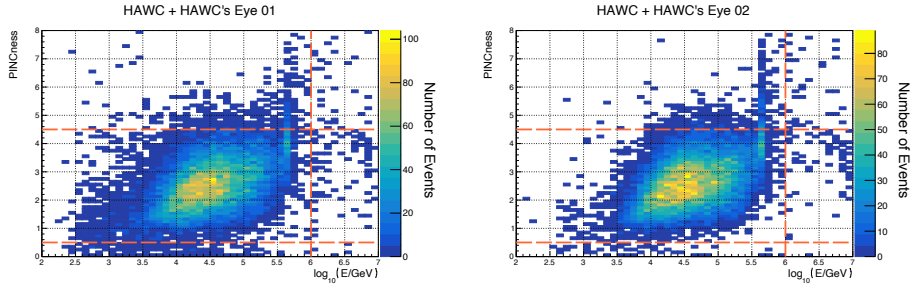

(a) (b)

Figure A.12: Quality cut of *rec.PINC*$\in [0.5, 4.5]$ considered for the hybrid data between HAWC and *(a)* HAWC's Eye 01 and *(b)* HAWC's Eye 02.

Leakage1< 0.3

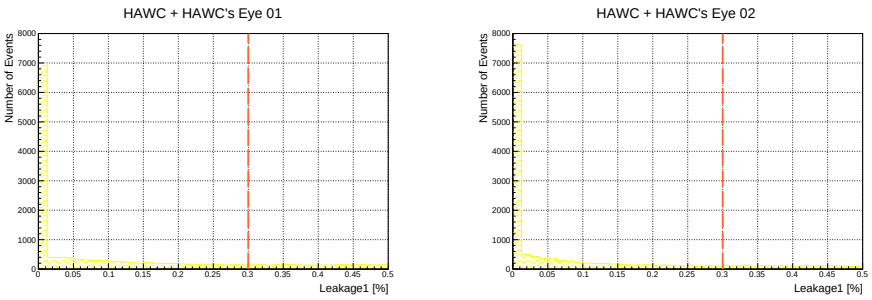

(a) (b)

Figure A.13: Quality cut of *Leakage1*< 0.3 considered for the hybrid data between HAWC and *(a)* HAWC's Eye 01 and *(b)* HAWC's Eye 02.

Width> 0.025

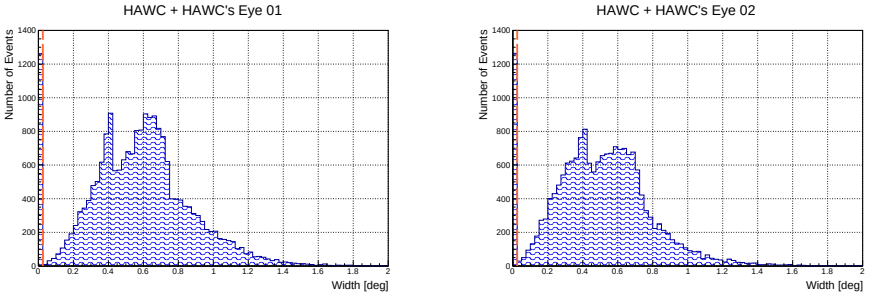

(a) (b)

Figure A.14: Quality cut of *Width*< 0.3 considered for the hybrid data between HAWC and *(a)* HAWC's Eye 01 and *(b)* HAWC's Eye 02.

ACKNOWLEDGEMENTS

Agradezco a mi familia por siempre ser parte de mi desarrollo personal, en especial a mis padres, Alma y José, quienes con su ejemplo y enseñanzas me han guiado. Este logro es de ustedes y para ustedes, gracias por todo hoy y siempre. Espero enorgullecerlos con este logro, el cual es uno de muchos más que están por venir, siempre siguiendo la filosofía del viejo: *paso a pasito.*

De igual manera agradezco a Lizbeth por estar a mi lado en todo este proceso ayudándome, levantándome y motivándome. Este logro es tanto tuyo como mío. Doy gracias por cada momento que has estado ahí para mi, motrándome que seguimos siendo el mejor ecuipo ayer, hoy y siempre.

Quiero agradecer al Dr. Rubén Alfaro y a la Dra. Magdalena González por todo su apoyo, facilidades y conocimientos brindados durante el desarrollo de este trabajo. Espero sigamos trabajando, desarrollando y aprendiendo cosas nuevas por mucho más tiempo.

Agradezco a mi comite tutoral conformado por la Dra. Mariana Cano Díaz y la Dra. Mariana Vargaz Magaña, quienes me apoyaron y aconsejaron a lo largo de todo el posgrado. Gracias.

Agradezco a mi comité sinodal conformado por el Dr. Juan Carlos Arteaga, el Dr. Ernesto Belmont, el Dr. Alejandro Farah, el Dr. Eduardo Moreno, y el Dr. Ibrahim Torres por su tiempo y esfuerzo invertidos en la revisión de este trabajo, así como su retroalimentación para la mejora del mismo.

Ich danke der Arbeitsgruppe von Prof. Dr. Thomas Bretz am III. Physikalischen Institut A der RWTH Aachen, bestehend aus Merlin Schaufel, Mia Giang Do, Florian Rehbein, Fabian Theißen and Marc Klinger, für das Teilen ihrer Erfahrung, ihre Beiträge und ihr feed back.

Ein ganz besonderer Dank gilt Jan Audehm für das gemeinsame Arbeiten, Lernen und den Spaß in dieser Zeit. Es war mir eine Freude mit ihnen zu arbeiten.

Un agradecimiento especial al Fís. Arturo Ismael Iriarte Valverde por toda su ayuda y conocimientos invertidos en este proyecto. Sin él este trabajo no hubiera sido posible.

En nombre de la Colaboración de HAWC's Eye, agradezco el apoyo por parte de DGAPA-UNAM (proyecto IN111419 y IG101320), asi como de DAAD-CONACYT (proyecto 279446). De igual manera agradezco al Laboratorio Nacional de Supercómputo del Sureste de México perteneciente a la red de laboratorios nacionales CONACYT, por los recursos computacionales, el apoyo y la asistencia técnica.

Finally, I want to acknowledge the HAWC Collaboration for its important and interesting feedback during this process, as well the FACT Collaboration for supplying the boards for the DAQ system of both HAWC's Eye telescopes.

LITERATURE

[Aab, 2020] Aab, A. e. a. (2020). Measurement of the cosmic-ray energy spectrum above $2.5\times10^{1}8$ ev using the pierre auger observatory. *Physical Review D*, 102(6):062005.

[Aartsen, 2020] Aartsen, M. e. a. (2020). Design and performance of the first IceAct demonstrator at the South Pole. *Journal of Instrumentation*, 15(02):T02002.

[Abeysekara et al., 2018] Abeysekara, A., Alfaro, R., Alvarez, C., Álvarez, J., Arceo, R., Arteaga-Velázquez, J., Solares, H. A., Barber, A., Baughman, B., Bautista-Elivar, N., et al. (2018). Data acquisition architecture and online processing system for the hawc gamma-ray observatory. *Nuclear Instruments and Methods in Physics Research Section A: Accelerators, Spectrometers, Detectors and Associated Equipment*, 888:138–146.

[Abeysekara, 2017] Abeysekara, A. e. (2017). Observation of the crab nebula with the hawc gamma-ray observatory. *The Astrophysical Journal*, 843(1):39.

[Aharonian et al., 2005] Aharonian, F., Akhperjanian, A., Bazer-Bachi, A., Beilicke, M., Benbow, W., Berge, D., Bernlöhr, K., Boisson, C., Bolz, O., Borrel, V., et al. (2005). Detection of tev γ-ray emission from the shell-type supernova remnant rx j0852. 0-4622 with hess. *Astronomy & Astrophysics*, 437(1):L7–L10.

[Albert, 2008] Albert, J., e. a. (2008). Implementation of the random forest method for the imaging atmospheric cherenkov telescope magic. *Nuclear Instruments and Methods in Physics Research Section A: Accelerators, Spectrometers, Detectors and Associated Equipment*, 588(3):424–432.

[Anderhub et al., 2013] Anderhub, H., Backes, M., Biland, A., Boccone, V., Braun, I., Bretz, T., Buß, J., Cadoux, F., Commichau, V., Djambazov, L., et al. (2013). Design and operation of FACT–the first G-APD Cherenkov telescope. *Journal of Instrumentation*, 8(06):P06008.

[Audehm, 2020] Audehm, J. (2020). Comissioning of two improved hawc's eye telescopes in a hybrid setup with the hawc gamma-ray observatory. Master's thesis, Rheinisch-Westfälische Technische Hochschule Aachen, Aachen, Germany.

[BeagleBone, 2021a] BeagleBone (2021a). BeagleBone.org Foundation. BeagleBone.org Black. URL: http://beagleboard.org/black. Accessed: May, 2021.

[BeagleBone, 2021b] BeagleBone (2021b). BeagleBone.org Foundation. BeagleBone.org Capes. URL: http://beagleboard.org/capes. Accessed: May, 2021.

[Bretz, 2006] Bretz, T. (2006). Observations of the active galactic nucleus 1es1218+ 304 with the magic-telescope. -.

[Bretz et al., 2018] Bretz, T., Hebbeker, T., Kemp, J., Middendorf, L., Niggemann, T., Peters, C., Schaufel, M., Schumacher, J., Auffenberg, J., and Wiebusch, C. (2018). A compact and light-weight refractive telescope for the observation of extensive air showers. *Journal of instrumentation*, 13(07):P07024.

[Bretz, 2003] Bretz, T. e. a. f. t. M. c. (2003). The MAGIC analysis and reconstruction software. In *International Cosmic Ray Conference*, volume 5, page 2947.

[Brun and Rademakers, 1997] Brun, R. and Rademakers, F. (1997). Root—an object oriented data analysis framework. *Nuclear Instruments and Methods in Physics Research Section A: Accelerators, Spectrometers, Detectors and Associated Equipment*, 389(1-2):81–86.

[Cañellas et al., 2012] Cañellas, A., Moldón Vara, F. J., Munar i Adrover, P., Paredes i Poy, J. M., and Ribó Gomis, M. (2012). Performance of the magic stereo system obtained with crab nebula data. *Astroparticle Physics, 2012, vol. 35, num. 7, p. 435-448*.

[CERN, 2021] CERN (2021). CERN. Distributed Information Management System (DIM). URL: http://dim.web. Accessed: May, 2021.

[De Angelis and Pimenta, 2015] De Angelis, A. and Pimenta, M. J. M. (2015). *Introduction to particle and astroparticle physics: questions to the Universe*. Springer.

[Do, 2021] Do, M. G. (2021). Analysis of extensive air showers with the HAWC's Eye telescopes at the HAWC Gamma-Ray Observatory. Master's

thesis, Rheinisch-Westfälische Technische Hochschule Aachen, Aachen, Germany.

[HAWC, 2021a] HAWC (2021a). The HAWC Observatory Official Wabpage: Schematics. URL: https://bit.ly/2SM83pj. Accessed: May, 2021.

[HAWC, 2021b] HAWC (2021b). The HAWC Observatory Official Wabpage: Site Pictures. URL: https://bit.ly/3vX613W. Accessed: May, 2021.

[Heck et al., 1998] Heck, D., Knapp, J., Capdevielle, J., Schatz, G., Thouw, T., et al. (1998). Corsika: A monte carlo code to simulate extensive air showers. *Report fzka*, 6019(11).

[Hillas, 2013] Hillas, A. (2013). Evolution of ground-based gamma-ray astronomy from the early days to the cherenkov telescope arrays. *Astroparticle Physics*, 43:19–43.

[Hillas, 1985] Hillas, A. M. (1985). Cerenkov light images of eas produced by primary gamma. In *19th International Cosmic Ray Conference (ICRC19), Volume 3*, volume 3.

[Hörandel, 2003] Hörandel, J. (2003). On the knee in the energy spectrum of cosmic rays. *Astroparticle Physics*, 19(2):193–220.

[Karttunen et al., 2016] Karttunen, H., Kröger, P., Oja, H., Poutanen, M., and Donner, K. J. (2016). *Fundamental astronomy*. Springer.

[Knoll, 2010] Knoll, G. F. (2010). *Radiation detection and measurement*. John Wiley & Sons.

[Kohnle et al., 1996] Kohnle, A., Aharonian, F., Akhperjanian, A., Bradbury, S., Daum, A., Deckers, T., Fernandez, J., Fonseca, V., Hemberger, M., Hermann, G., et al. (1996). Stereoscopic imaging of air showers with the first two hegra cherenkov telescopes. *Astroparticle Physics*, 5(2):119–131.

[Kraehenbuehl, 2011] Kraehenbuehl, T. (2011). Calibrating the camera for the first g-apd cherenkov telescope (fact). In *International Cosmic Ray Conference*, volume 9, page 30.

[L' Annunziata, 2016] L' Annunziata, M. F. (2016). *Radioactivity: introduction and history, from the quantum to quarks*. Elsevier.

[MAGIC, 2021] MAGIC (2021). The MAGIC Telescopes Official Webpage. URL: https://magic.mpp.mpg.de/. Accessed: May, 2021.

[MILAGRO, 2021] MILAGRO (2021). MILAGRO @NYU Webpage. URL: https://bit.ly/3vX613W. Accessed: May, 2021.

[Nagano, 2000] Nagano, M. e. a. (2000). Observations and implications of the ultrahigh-energy cosmic rays. *Reviews of Modern Physics*, 72(3):689.

[Niggemann et al., 2015] Niggemann, T., Assis, P., Brogueira, P., Bueno, A., Eichler, H. M., Ferreira, M., Hebbeker, T., Lauscher, M., Mendes, L., Middendorf, L., et al. (2015). Status of the silicon photomultiplier telescope famous for the fluorescence detection of uhecrs. *arXiv preprint arXiv:1502.00792*.

[ON-Semiconductor, 2021] ON-Semiconductor (2021). ON Semiconductor *Data sheet MJ-Series SiPM Sensors Rev. 6*. URL: https://www.onsemi.com/pdf/datasheet/microj-series-d.pdf. Accessed: May, 2021.

[Pence et al., 2010] Pence, W. D., Chiappetti, L., Page, C. G., Shaw, R. A., and Stobie, E. (2010). Definition of the flexible image transport system (fits), version 3.0. *Astronomy & Astrophysics*, 524:A42.

[Pool, 2021] Pool, A. (2021). Random forest understanding. URL: https://ai-pool.com/a/s/random-forests-understanding. Accessed: Sep, 2021.

[Rehbein, 2021] Rehbein, F. e. a. (2021). Preliminary cosmic ray results from the hawc's eye telescopes. *In the 37th International Cosmic Ray Conference*.

[SAMTEC, 2021] SAMTEC (2021). SAMTEC INC. MH081 SERIES Catalogue. URL: http://suddendocs.samtec.com/catalog_english/mh081.pdf. Accessed: May, 2021.

[Schaufel, 2017] Schaufel, M. (2017). Implementing hybrid detection by combining a compact air-cherenkov telescope with the hawc gamma-ray observatory. Master's thesis, Rheinisch-Westfälische Technische Hochschule Aachen, Aachen, Germany.

[Schaufel et al., 2019] Schaufel, M., Andeen, K., and Auffenberg, J. (2019). IceAct, small Imaging Air Cherenkov Telescopes for IceCube. *arXiv preprint arXiv:1908.11177*.

[Schneider, 2014] Schneider, P. (2014). *Extragalactic astronomy and cosmology: an introduction*. Springer.

[Schumacher et al., 2016] Schumacher, J., Auffenberg, J., Bretz, T., Hebbeker, T., Louis, D., and Zantis, F.-P. (2016). Dedicated power supply system for silicon

photomultipliers. In *The 34th International Cosmic Ray Conference*, volume 236, page 605. SISSA Medialab.

[Schumacher, 2019] Schumacher, J. C. (2019). *Exploring silicon photomultipliers for the upgrade of the Pierre Auger observatory*. PhD thesis, Physikalisches Institut 3A, RWTH Aachen, Aachen, Germany.

[SenseL, 2021] SenseL (2021). SenseL Technologies, Ltd. *Data sheet MJ-Series SiPM Rev. 2.5*. URL: http://www.eqphotonics.de/cms/cms/upload/datasheets/DS-MicroJseries.pdf. Accessed: May, 2021.

[Serna-Franco, 2021] Serna-Franco, J. e. a. (2021). Simularion performance of 55 imaging air-cherenkov telescopes hawc's eye at high altitude. *In the 37th International Cosmic Ray Conference*.

[Spurio, 2014] Spurio, M. (2014). *Particles and astrophysics*. Springer.

[TexasInstruments, 2021] TexasInstruments (2021). Texas Instruments Inc. MSP430 ultra-low-power MCUs. URL: http://www.ti.com/microcontrollers/msp430-ultra-low-power-mcus/overview.html. Accessed: May, 2021.

[UChicago, 2021] UChicago (2021). TeV Catalog (TeVCat). URL: http://tevcat.uchicago.edu/?mode=1&showsrc=74. Accessed: Aug, 2021.

[Ulrich et al., 1998] Ulrich, M., Daum, A., Hermann, G., and Hofmann, W. (1998). An improved technique for the determination of shower geometry from single and stereo iact images. *Journal of Physics G: Nuclear and Particle Physics*, 24(4):883.

[Wells and Greisen, 1979] Wells, D. C. and Greisen, E. W. (1979). FITS-a flexible image transport system. In *Image Processing in Astronomy*, page 445.

[Wright and Ziegler, 2015] Wright, M. N. and Ziegler, A. (2015). ranger: A fast implementation of random forests for high dimensional data in c++ and r. *arXiv preprint arXiv:1508.04409*.

[XCDF, 2021] XCDF (2021). Braun, Jim. Git Repository XCDF. URL: https://github.com/jimbraun/XCDF. Accessed: May, 2021.